MONASH University

Computational Modelling of 4D Flow MRI Data

by

Abdul Mateen Qadri

B.Eng(Hons)

A Thesis submitted to Monash University

for the degree of

Master of Engineering Science (Research)

February 2020

Department of Mechanical and Aerospace Engineering

Monash University

Copyright notice

Computational Modelling of 4D Flow MRI Data

Abdul Mateen Qadri

Abstract

Phase-averaged blood flow dynamics in the cardiac chambers and great vessels can be visualised accurately using 4D flow cardiac magnetic resonance imaging (time-resolved blood flow). Although 4D flow MRI has proven its utility in highlighting the spatial (3D) and temporal (1D) evolution of three dimensional blood flow with full coverage of any vascular or cardiac region of interest, it is restricted by acquisition noise and limits on its spatial and temporal resolution. Furthermore, diagnostic measures obtained solely from cardiac MRI can often be late indicators of dysfunction. Post-processing 4D flow data to develop novel, sensitive biomarkers of dysfunction may aid clinicians in their prognostic and diagnostic endeavours. This thesis presents the results of two studies related to the modelling of 4D cardiac MRI data.

The first study presents the results of post-processing the existing flow data to obtain patient-specific residence-time distributions (RTD), a novel means of determining ventricular function. Furthermore, RTDs can provide an insight of the extent of overall blood flow, mixing and stasis, which affect cardiac function. A quantitative constant related to the RTDs was developed by tracking individual virtual particles and calculating plane crossing times. In the left ventricle, the RTD constant was compared to the left ventricular (LV) ejection fraction, global longitudinal strain (GLS) and T1 native values. A significant difference was seen in the LV RTD_c between healthy subjects and patients reporting cardiac dysfunction(1.2 ± 0.13 vs 2.2 ± 0.80, $p < 0.001$). A strong negative correlation was reported between the LV RTD_c and the LVEF ($R = -0.843, p < 0.001$). When the RTD constant was compared to the GLS, a strong correlation coefficient of $R = 0.7805$ was seen. A weak

correlation was seen between the RTD constant and native T1 time ($R = 0.1517$). The correlation was not as strong in the right ventricle ($R = -0.7113$, $p < 0.001$) or the right atrium ($R = -0.4543$). The results suggest that the left ventricular residence time constant has the capability of distinguishing normal from dysfunctional cardiac function.

The second study presents a computational model of the left ventricle that expands and contracts over the cardiac cycle. The volume of the computationally obtained model related closely to MRI volumetric changes. Furthermore, the ejection fraction obtained from the model was similar to cardiac MRI measurements (57% versus 60%). Further development of the model presented here will yield a greater insight into the utility of computationally derived markers, such as the vorticity, as a novel marker of cardiac dysfunction.

Dedication

To my parents, Dr Haneef Ahmed Qadri and Dr Rohilla Fazili, for their never-ending
love and support.

Declaration

This thesis contains no material which has been accepted for the award of any other degree or diploma at any university or equivalent institution and that, to the best of my knowledge and belief, this thesis contains no material previously published or written by another person, except where due reference is made in the text of the thesis.

Signature:

Name: Abdul Mateen Qadri

Date: February 27, 2020

Publications Relating to Thesis

Costello, B., **Qadri, A.M.**, Price, B., Papapostolou, S., Thompson, M., Hare, J.L., La Gerche, A., Rudman, M., Taylor, A.J. 2018, "The ventricular residence time distribution derived from 4D flow particle tracing: a novel marker of myocardial dysfunction", *The International Journal of Cardiovascular Imaging*, vol.34, pg. 1927-1935

Acknowledgements

Qadri, and my parents, Dr. Haneef Ahmed Qadri and Dr. Rohilla Fazili. Special thanks to Bhai for reading my thesis numerous times and for providing meaningful feedback. Thank you all so much for your unconditional love, encouragement and understanding through some very troubling times. And last but not least, to the Almighty God for giving me this incredible opportunity. This world is filled with uncertainties, but there is one thing I am certain of: I will never be deserving of the opportunities you have given me. Alhamdulilah.

Contents

List of Figures

List of Tables

Chapter 1

General Introduction

1.1 Introduction

The World Health Organization's (WHO) annual statistical report revealed that the leading cause of death due to non-communicable diseases in 2017 was cardiovascular disease (CVD), accounting for 17.7 million casualties (WHO, 2017). There are numerous types of CVDs such as high blood pressure, stroke, coronary artery disease and arrhythmia, amongst others (Chan *et al.*, 2013). Arrhythmia refers to abnormalities in heartbeat cadence that reduce cardiac output, thereby decreasing heart efficiency. A common form of arrhythmia is atrial fibrillation (AF), where the upper two chambers of the heart (atria) experience abnormal electrical signals, thereby preventing the heart from beating in a regular manner. As a result, blood pools in the atria, which can cause clots to form. A vital blood vessel can be blocked if one of the blood clots leaves the heart and travels towards the brain. Oxygen is thus prevented from reaching the brain through the bloodstream, thereby causing a stroke. Statistically, patients afflicted by atrial fibrillation are at five times higher risk of stroke compared to those without AF.

Blood flow through the heart is difficult to characterise in general as it differs based on the cardiac function and the health of the patient. Obtaining the internal haemodynamic flow patterns of patients with arrhythmia is potentially beneficial to physicians in providing insight into the causes leading to arrhythmias, and may

assist in their diagnosis and treatment.

1.2   Motivation

The most commonly used medical test to diagnose arrhythmias are electrocardiograms, which capture the electrical activity of the heart, and describe the rhythm and how fast it is beating. However, electrocardiograms are incapable of describing how the blood flows through the heart, for example the fluid velocity and flow rate, and any regions of stagnant or recirculating flow. Relying solely on existing diagnostic techniques can be detrimental as they can be late indicators of dysfunction. Therefore, obtaining markers of cardiovascular disorder earlier in the diagnostic process may improve health outcomes for patients.

In this capacity, the role of imaging tools such as cardiovascular magnetic resonance (CMR) is indisputable, and *four-dimensional phase-contrast magnetic resonance (4D PCMR) flow imaging* has demonstrated its utility to provide information on the spatial (3D) and temporal (1D) evolution of three dimensional blood flow with full coverage of any vascular or cardiac region of interest (Eriksson *et al.*, 2010; Geiger *et al.*, 2011; François *et al.*, 2012; Valverde *et al.*, 2012). However, 4D PCMR exhibits some deficiencies as it is affected by acquisition noise and resolution limits. Post-processing CMR data using numerical methods provide a method of deriving beneficial quantitative data from qualitative imaging. Particle tracing, which involves seeding conceptual particles from a sequence of 4D PCMR images and tracking these over a cardiac cycle, provides information on how long blood resides in the cardiac chamber. Merging 4D flow MRI with computational fluid dynamics (CFD) allows the reconstruction of reduced noise, and more spatially and temporally resolved velocity flow fields. Time-dependent flow fields can provide greater information on the haemodynamics (blood flow) within the heart. Derived markers such as pressure differences, quantification of vortices, energy transfer and residence time from post-processing 4D flow MRI data may be complementary to clinicians in differentiating between healthy and abnormal heart function. These quantitative

measures have the potential of providing sensitive methods to detect early stages of heart dysfunction.

It is in this role that computational analyses and CFD are potentially clinically complementary and relevant. As the economic cost of cardiovascular diseases (and particularly arrhythmia) remains high, it is imperative, therefore, to develop economical, reliable and improved diagnostic methods that are non-invasive by utilizing the fields of technology, medicine and engineering.

1.3 Heart physiology

For the purposes of understanding the current study, a brief overview of the structure of the heart, the cardiac cycle and cardiovascular disease is first presented. A detailed description of heart anatomy can be obtained in medical textbooks (e.g. Klabunde, 2012). The heart consists of four chambers: two ventricles and two atria as seen in Figure 1.1. Ventricles are responsible for pumping blood to other organs in the body, whereas the atria act as reservoirs for blood before it is pumped into the ventricles. The inflow and outflow of blood from each ventricle is regulated by two valves.

Four pulmonary veins transport oxygenated blood from the lungs into the left atrium (LA). The mitral valve (MV) separates the LA from the left ventricle (LV). The aorta distributes oxygen-rich blood from the LV to the rest of the body. The aortic valve is responsible for preventing the backflow of blood into the LV. Oxygen-depleted blood is returned from the rest of the body to the right atrium (RA) by two major veins - the superior and inferior vena cava. The tricuspid valve separates the right atrium (RA) and the right ventricle (RV). The pulmonary valve, when open, allows deoxygenated blood to flow from the RV to the lungs via the pulmonary artery. At the lungs, a gas exchange occurs; specifically, the delivery of oxygen into the bloodstream from the lungs and elimination of carbon dioxide from the bloodstream to the lungs. The septum separates the right and left sections of the heart. The LV has a thicker wall compared to the RV due to the requirement for blood from the LV to be transported to the whole body whereas the RV expels blood

Abbreviations: RA, right atrium; RV, right ventricle; LA, left atrium; LV, left ventricle; T, tricuspid valve; P, pulmonic valve; M, mitral valve; A, aortic valve; SVC, superior vena cava; IVC, inferior vena cava; PA, pulmonary artery; PV, pulmonary veins
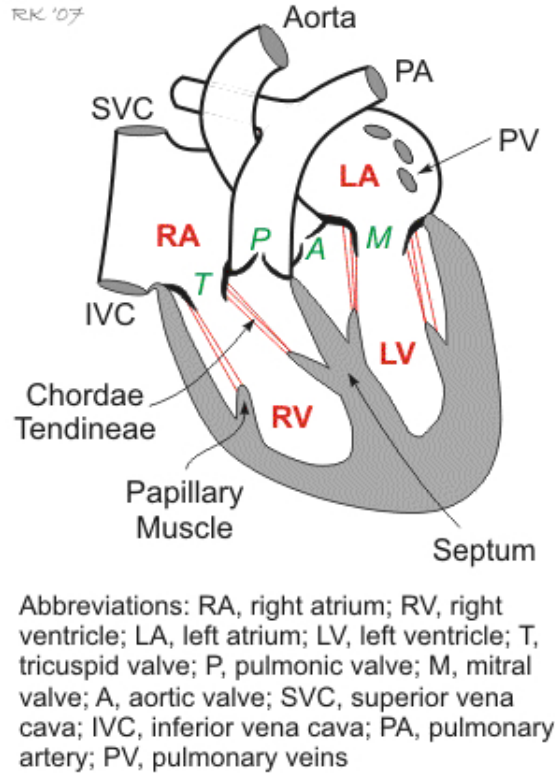
Figure 1.1: Physiology of heart with connecting arteries and veins (Klabunde, 2007).

only to the lungs.

The heart contains four valves which are made of two or three leaflets. Papillary muscles hold the mitral and tricuspid valve to the ventricular walls. To prevent the flow of blood back into the atria, tension is generated on the valve leaflets during contraction by the papillary muscles. The pulmonary and aortic valves lack papillary muscles as they are passive structures. The opening of the leaflets is caused by fluid flow pushing the leaflets out, whereas reverse fluid flow causes the leaflets to move back into the ventricular passage and close.

1.4 Cardiac cycle

There are four major phases of a cardiac cycle: diastole, isovolumetric contraction (IVC), systole and isovolumetric relaxation (IVR) as seen in Figure 1.2. Blood enters the LV through the mitral valve due to ventricular dilation during the diastole phase while the aortic valve remains closed. The diastole can be further divided
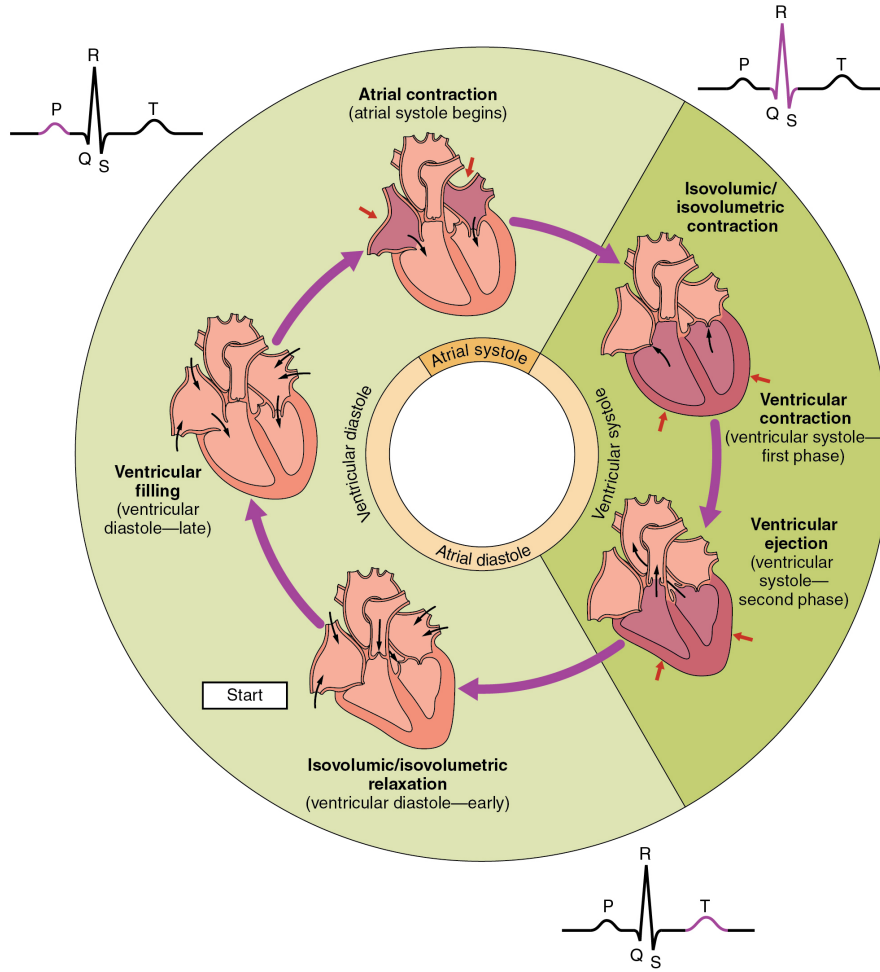
Figure 1.2: Overview of the Cardiac Cycle. The cardiac cycle begins with atrial systole and progresses to ventricular systole, atrial diastole, and ventricular diastole, when the cycle begins again. Correlations to the ECG are highlighted (Biga *et al.*, 2016).

into three sub-phases: primarily the early filling (rapid filling), slow filling (diastasis) and late filling (re-filling). As the LV begins to expand, the mitral valve opens and blood enters into the LV due to a high pressure differential between the LA and LV. As blood continues to fill the LV, the intraventricular pressure increases. The pressure gradient across the mitral valve reduces and thus the rate of blood filling falls. The atrium contracts causing the blood to accelerate in the late filling phase into the LV. As the late filling phase ends, the mitral valve closes and the IVC phase begins. During this phase, the volume remains constant as both valves are closed. The intraventricular pressure increases and the LV readies itself for ejection.
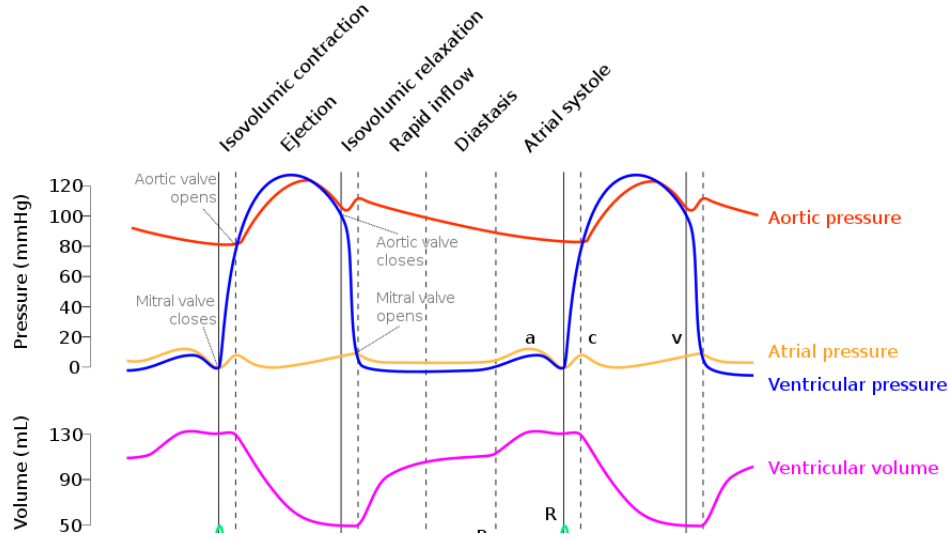
Figure 1.3: Variation of pressure and volume during the cardiac cycle (Biga *et al.*, 2016).

The systolic phase begins as the IVC ends. Here, the contraction of the LV pushes blood into the ascending aorta through the aortic valve. The mitral valve remains closed to prevent backflow into the LA and the aortic valve opens. The systolic phase can be divided into two phases: accelerated systole (rapid ejection) and decelerated systole (reduced ejection). Higher pressure gradients during the accelerated systole phase result in the blood velocity being higher compared to the reduced ejection. As the aortic valve closes, the IVR begins. Both the aortic and mitral valve are closed and their volume remains constant. Intraventricular pressure falls as the LV begins to relax. By the end of the IVR, one complete cardiac cycle has occurred. A summary of how the pressure and volume changes over the cardiac cycle is provided in Figure 1.3.

1.5 Cardiac pathology

An outline of the cardiac pathology relevant to the current study is provided.

Dilated cardiomyopathy (DCM) is a disease where the muscle of the heart (myocardium) begins to dilate (stretches and becomes thinner). The thinning of the muscle results in larger left ventricular volume, and therefore more blood is held. As the ventricle enlarges, the muscle is unable to contract normally, and the heart is

impaired in its blood pumping ability. DCM often goes undiagnosed because many people afflicted fail to show any symptoms. A small number face amongst other symptoms abnormal heart rhythms (arrhythmia). This is because dilated heart muscle, as well as the abnormal structure of heart cells, can disrupt the normal functioning of the heart's electrical system, resulting in fast or irregular heartbeats. Atrial fibrillation, a complication some experience, can also increase the risk of developing blood clots, which may dislodge and travel to the brain, causing a stroke.

1.6 Diagnostic techniques and markers

Ejection Fraction (EF) is a commonly used measure to define how well the heart is able to pump out blood. It is calculated by taking the fraction of the volume of blood pumped out of the chamber against the total volume of blood in the chamber. Patients with arrhythmias are often diagnosed with reduced ejection fraction, as revealed by medical tests. The volume of blood pumped out per contraction is referred to as the stroke volume (SV). The total amount of blood collected in the chamber at the end of the filling phase is the end diastolic volume (EDV). In other words, the ejection fraction is the ratio of SV to EDV. An error of $< 3\%$ for the measured ejection fraction can be achieved (O'Dell, 2019). The main sources of error in the estimation of left ventricular ejection fraction are (1) inability to sample the entire portion of the left ventricle from the mitral valve region (base) to the apex; (2) regions where 2-dimensional short-axis MRI images lack enough detail undergo interpolation by making geometric assumptions and (3) segmentation errors of the endocardial (inner heart) border from 2-dimensional images.

Global longitudinal strain (GLS) is an alternative measure used by clinicians to describe cardiac function. Specifically, GLS measures myocardial deformation. It is calculated by taking the fraction of the change in length of cardiac tissue, as measured by echocardiography (described shortly), against the original length at the point of peak contraction. Recent reports have suggested that the relationship between mortality and left ventricular ejection fraction is not strong; whereas reduced

GLS has been an excellent measure to provide clinicians a suitable prognosis for numerous heart failure-related results exclusive of LVEF (*Left Ventricular Ejection Fraction*) (Kalam *et al.*, 2014). The GLS therefore provides additional prognostic detail and can act as a significant marker for improving risk assessment in abnormal cardiac function (Morris *et al.*, 2017; Park *et al.*, 2018). Errors in assessing GLS arise from varying values obtained when using different software packages and may also change due to inter- and intra-observational variations (Ashish *et al.*, 2019).

T1 mapping provides a further avenue for clinicians to non-invasively measure changes in myocardial composition. T1 "mapping" specifically refers to information derived from the ability of CMR to measure myocardial T1 relaxation time (how quickly protons recover after being "flipped" by a radiofrequency pulse) on a pixelwise basis. The native T1 value is the exponential time constant obtained from curve fitting the T1 relaxation time data points over the entire myocardial domain. An error source for T1 values arise from partial volume contamination from blood, which is more prevalent for thin-walled structures (Kellman & Hansen, 2014).

For the purposes of the current study, three diagnostic methods of the markers previously described are briefly outlined below. The state-of-the-art technology used currently in the diagnosis of cardiac dysfunction is cardiac MRI. Magnetic fields and radio waves are used to create cross-sectional images of the heart. Each MR imaging data acquisition provides information on the signal magnitude and the phase of each voxel (i.e. a small averaging volume). In conventional imaging, only the signal magnitude of each voxel is used to construct the anatomic display (the magnitude image). Quantitative information on blood flow can be obtained using phase-contrast magnetic-resonance imaging (PC-MRI). In phase-contrast imaging, the phase of each voxel is used to calculate the voxel velocity in each direction to generate a velocity image. Thus, PC-MRI is capable of acquiring all three velocity components of blood flow, thereby providing a three-dimensional blood velocity field through the entire imaging volume. Important markers of dysfunction such as ejection fraction, GLS and T1 values can be obtained from cardiac MRI measurements.

As indicated above, the most commonly used medical test to diagnose arrhythmias is the electrocardiogram (ECG) that records electrical activity and describes the rhythm and its frequency. It is a rapid, non-invasive and painless diagnostic procedure. The electrical activity of the heart is detected by electrode sensors that are attached to the chest. Each heart beat is triggered by electrical impulses generated by a special set of cells (pacemaker cells) in the atria. The electrocardiogram records the duration and the strength of the signals, which are displayed as waves on a monitor or printed on graph paper.

An alternative medical test often ordered by cardiologists is an echocardiogram (echo). An echo test is an ultrasound study of the heart. High frequency sound waves are emitted from a probe that is placed on the chest of a patient. A transducer records the sound waves that echo from the heart, and these are converted into images by a computer. A cardiologist is able to thereby determine the relative functioning of the heart and its valves, the strength of contraction of the left ventricle (left ventricular ejection fraction) and the pressure within the heart. A doppler echocardiogram (Echo doppler) allows the speed and direction of the blood flow in the heart to be measured. Sounds wave emitted by the probe undergo a change in pitch as they hit blood cells and echo back. The shift in pitch (Doppler shift) allows the measurement of blood flow direction and velocity in the heart. Advances in technology have meant that 3D echocardiography has become more widely used, allowing the assessment of 3D blood flow velocities. There are some inherent limitations with echocardiography, as eccentric and abnormal flow patterns present a risk for misalignment of the ultrasound beam with the flow jet during the contraction phase for patients with valvular disease. 4D flow MRI is not hindered by the eccentricity of flow, as its multidirectional velocity-encoding allows velocities to be quantified regardless of the spatial orientation of the flow jet (Adriaans et al., 2020).

1.7   Objective of study

The primary objective of this study is the development of novel sensitive markers of cardiac dysfunction. To achieve this, a data-driven approach is initially utilised to develop residence time distributions from particle tracing data. In this approach, residence time distributions (RTDs), an innovative approach of evaluating ventricular function, can be obtained by post processing flow data directly obtained from MRI measurements. The residence time distribution was originally devised to assess the efficiency of chemical reactors, and here reflects the cumulative distribution of the time it takes for a blood volume to transit a cardiac chamber and exit. By correlating parameters obtained from the RTDs with existing cardiac measures (such as the ejection fraction, GLS and T1 native values), the utility of residence time distributions in assessing cardiovascular performance can be determined, and quantitative markers of dysfunction potentially discovered. These markers may then be used in a future clinical trial to assess whether they provide any additional information over existing metrics as a tool for early diagnosis. Following on from the data-driven approach, to quantify dysfunction, a patient-specific CFD-MRI method was developed to investigate 3D intraventricular flow patterns in dysfunctional and normal hearts. The results from such an approach may provide practical and useful insights into heart function, in terms of qualitative and quantitative markers such as pressure gradients, recirculating flows, energy loss (EL), and wall shear stress (WSS).

1.8   Thesis outline

The thesis is organised as follows:

Chapter 2 provides a background to the current study and highlights relevant previous works from the literature.

In Chapter 3, the methodology used in the current study is described. This includes the computational methodology to develop the residence time distributions,

and the details of the parameters used in the computational fluid dynamics modelling. Additionally, the acquisition of MRI data is described briefly followed by a detailed account of the reconstruction of LV geometry including the atrium inlet and aorta outlet.

Chapter 4 presents the results obtained from the residence time distributions, in particular comparing healthy subjects and patients with dilated cardiomyopathy (DCM). The residence time distribution constant is compared to ejection fraction, GLS and T1 value in the LV and RA and the correlation noted. In this chapter, we demonstrate the utility of the RTD constant as a useful tool for describing cardiac function. The content of Chapter 4 has in part appeared in a separate article (Costello *et al.*, 2018), that has been published in the *International Journal of Cardiovascular Imaging.*

In Chapter 5, some results from CFD analysis on the left ventricle geometry is presented. The finite-volume method is used to solve the discretized Navier-Stokes equations in the commercial fluid dynamics software ANSYS-Fluent. A dynamic mesh routine that describes the expansion and the contraction of the LV chamber is detailed. Using representative flow parameters for blood, initial results are obtained and discussed.

Finally, Chapter 6 summarises and concludes the study, briefly recapping the contributions it makes to understanding cardiac function. It also discusses further work that should be performed.

Chapter 2

Literature Review

2.1 Introduction

The heart can be considered a multiphysics organ. A number of studies have been carried out in a effort to understand the flow dynamics in the heart. Hunter *et al.* (2003) published a framework that incorporated all heart functions including cardiac cell behaviour and structure. Linking the different functions of the heart is challenging due to a lack of detailed knowledge, and it has not yet been possible to achieve the goal of a comprehensive model. Studies have used different numerical approaches and assumptions to simplify the geometry and flow in the heart chambers. In this chapter, important computational works related to cardiac blood flow will be introduced and critiqued. Experimental studies are explained initially followed by computational approaches to simulate cardiac blood flow.

2.2 Experimental studies

Relevant experimental studies have been primarily based on phase-mapping MRI measurements or Echo-Doppler approaches. Magnetic resonance velocity mapping was used by Kim *et al.* (1995) to investigate vortex formation in the LV. They discovered a near uniform velocity profile across the mitral valve diameter. During the early diastole, a large counterclockwise vortex was observed at the mitral valve

leaflets, followed by a smaller vortex during the late diastole. No vortices were observed during the systolic phase and blood flow was directed towards the outflow tract.

Kilner *et al.* (2000) carried out non-invasive measurements for a normal heart using magnetic resonance velocity mapping. Changes in the blood flow direction and asymmetries were captured using MR phase-velocity mapping. During the early diastole, part of the blood flow was directed towards the aorta outlet. This feature was thought to minimize energy dissipation in the heart, as it allowed the momentum of the inflowing stream to be preserved. They also observed recirculating blood flow beneath the mitral-valve leaflets, particularly around the anterior leaflet.

Ebbers *et al.* (2002) carried out three dimensional in-vivo velocity measurements using phase-contrast MRI. The relative pressure in the LV was derived by solving the Poisson equation governing the pressure field. Pressure differences between the apical and basal (apex and base) portions of the LV were obtained during the diastole and systole phases. They discovered similar pressure distributions during the two phases. Pressure differentials due to convective inertia during ejection and filling were also discussed. They concluded that pressure differences at the peak inlet and outlet flow velocities were small, whereas maximum pressure differences were seen at the beginning and end of the diastolic and systolic phases.

Fenster *et al.* (2015) carried out a preliminary study with a small group of healthy patients and patients with pulmonary artery hypertension (PAH). They studied how 4D flow CMR could be used to evaluate right ventricular flow patterns, diastolic function and recirculating flow. They discovered that right ventricular diastolic dysfunction (RVDD) was associated with a decrease in spatially integrated vorticity (13 versus 28 (s^{-1})) for the right atrium during the early relaxation phase. Furthermore, an increase in vorticity during the late relaxation phase was also seen (2343 versus 492 (s^{-1}) in the right ventricle and 30 versus 9 (s^{-1}) in the right atrium). They hypothesized that changes in the vorticity field were detectable prior to the onset of changes in other flow metrics for a patient, and therefore concluded that vor-

ticity could be used as a sensitive noninvasive biomarker for ventricular dysfunction in PAH.

Karlsen *et al.* (2019) investigated the reproducibility of the global longitudinal strain (GLS) and the left ventricular ejection fraction (LVEF). An echocardiographic examination was carried out for forty-seven patients that suffered from a reduction of blood flow to the heart. They found that the systematic difference was lower for GLS measurements compared to LVEF (0.21% vs 4.08%). Comparing measurements obtained by an expert echocardiographer and a trainee, the intra-class correlation coefficient was higher for GLS compared to the LVEF (0.89 vs 0.63) respectively. Their findings demonstrated that GLS was a more reproducible method for evaluation of LV function compared to the LVEF regardless of image quality and echocardiographic training.

A number of studies have sought to demonstrate how the GLS and T1 values can provide additional prognostic information over the ejection fraction. Morris *et al.* (2017) carried out a study on 2302 controls and 2282 patients suffering from heart failure with preserved ejection fraction (HFPEF). This is a syndrome in which patients have some of the clinical features of heart failure (such as shortness of breath) whilst maintaining a normal left ventricular ejection fraction (i.e. greater than 50%). They found that the sick patients had significantly lower GLS (mean: -15.7%, range: -12% to -18.9%) than the healthy controls (mean: -19.9%, range: -17.1% to -21.5%). In a study on 46 controls and 92 HFPEF subjects, Weiss *et al.* (2017) found that T1 times were significantly shorter in HFPEF subjects compared to the controls (398 ± 51 vs. 424 ± 37 ms, $p < 0.01$). Clearly, GLS and T1 can provide additional information of clinical use in instances whereby the ejection fraction does not suggest cardiac dysfunction.

The GLS has also been shown to be a better marker for mortality compared to the LVEF. Kalam *et al.* (2014) collected data from 16 published studies which comprised 5721 adults. They found that mortality was independently associated with with each standard deviation change in the absolute value of baseline GLS and less strongly

with LVEF. A study carried out by Park *et al.* (2018) found that patients with reduced strain had significantly higher mortality compared to patients with reduced ejection fraction. Furthermore, they found that each percentage decrease in GLS was associated with a 5% increase in mortality risk, and that LVEF was not associated with mortality.

The residence time distribution was originally devised to assess efficiency of chemical reactors and here reflects the cumulative distribution of the time it takes for a blood volume to transit a cardiac chamber and exit. A detailed description is provided in Fogler (1999). Originally, RTDs were utilized to describe the mixing and flow within chemical reactors, and to draw comparisons between the behavior of these reactors against idealised models. Danckwerts (1953) studied how models could be used to predict the distribution of residence times in large systems. The utility of the distribution function was illustrated by showing how they could be used to calculate the efficiencies of blenders and reactors. RTDs have been also used in the pharamaceutical industry to determine the position of raw materials in the manufacturing process. Engisch & Muzzio (2016) studied how the development of an overall system RTD allowed the tracing of raw materials across the entire system, from the feeder to the tablet press. Additionally, disturbances could be predictively tracked through the entire continuous system. This permits downstream control or even removal of the affected material. Corrective action at the onset of a disturbance is possible when coupled with a diagnostic system (i.e. fault mitigation system). Processes that are characterized by fast reaction rates, intense heat and mass transfer and rapid catalyst deactivation require good control of residence time (Wei & Zhu, 1996). Therefore, residence time distribution data aids in the understanding of fluid dynamics, and are critical for plant operation, optimisation, reactor design and scale-up. The concept of the RTD has also been used to understand the hydraulics of a wetland. When tracer particles are introduced into a nonideal wetland (i.e. one where particles have different residence times), the output tracer concentration is an RTD reflecting the dispersive nature of the system. A

study by Koskiaho (2003) used RTD analysis to design the shape of a wetland with the aim of reducing zones with diminished mixing, thereby optimizing the efficiency of treatment. Ta & Brignal (1998) used RTD analysis to optimize the wetland inlet and outlet tract position to maximize treatment efficiency. A study by Stern *et al.* (2001) showed how natural flooding events in wetlands adjacent to rivers and streams resulted in observable changes in RTD characteristics. The RTD of blood particles in the cardiac context offers the possibility of determining features such as atrial short-circuiting, stagnant zones and whether the cardiac process is more like a well-stirred reactor or a plug flow with little mixing.

Although RTDs have been explored previously with artificially manufactured left ventricles, they have not as yet been used in an existing clinical setting (Shettigar *et al.*, 1989). In their study on an artificial LV, Shettigar *et al.* (1989) found that approximately 58% of particles remain in the ventricle after the first heartbeat, 22% after the second heartbeat, and 5% after the third. Whilst mixing of blood is not a crucial component for satisfactory cardiac function, the slowing and stopping of blood flow (stasis) can have significant consequences to disease and cardiac physiology.

2.3 Computational studies

Numerical studies of predicting blood flow in the LV have made great progress in recent years. They have been classified by Cheng *et al.* (2005) into three broad categories: (1) geometry-prescribed CFD methods; (2) immersed boundary methods; and (3) fluid-structure interaction (FSI) methods. Geometry prescribed methods use the defined movement of the boundary (i.e.the wall) as a boundary condition. Immersed boundary and, in particular, FSI methods aim to directly model the fluid-structure interaction. Peskin (1972) introduced the immersed boundary method for modelling two-dimensional flow patterns around heart valves. This particular version of the immersed boundary method simplifies the heart muscle structure as an elastic-walled boundary immersed in, and interacting with, the fluid. This method

was further developed in later studies for modelling blood flow within the heart (McQueen & Peskin, 1985, 1989, 1997, 2000, 2002). FSI methods generally use the finite-element method for modelling the heart structure and different CFD approaches for the fluid domain. These methods have been further developed in recent years, utilising more realistic coupling methods between the fluid and structure domains (Watanabe *et al.*, 2004; Cheng *et al.*, 2005; Krittian *et al.*, 2010).

Geometry prescribed CFD studies can be divided into two groups: (1) those based on generic models and, (2) those based on imaging data, i.e. Computerized Tomography (CT) and MRI data.

2.3.1 Generic models

2D and 3D generic models have been developed and utilized in recent years to understand LV fluid dynamics (Vierendeels *et al.*, 2000; Baccani *et al.*, 2002*a*,*b*, 2003; Bolzon *et al.*, 2003; Domenichini *et al.*, 2005; Pedrizzetti & Domenichini, 2005; Domenichini & Pedrizzetti, 2011). Such generic models treat the LV deformation as axisymmetric, as a segment of a partial ellipsoid (or prolate spheroid). They usually use a symmetrical (centralised or non-centralised) circular opening.

In their study, Vierendeels *et al.* (2000) used a 2D axisymmetric geometry to model diastolic flow in the LV. They obtained the velocity and pressure distributions in the LV model and found that vortices were generated below the mitral valve inlet during flow acceleration and were seen moving towards the apex during flow deceleration.

Baccani *et al.* (2002*a*,*b*, 2003) studied LV fluid dynamics during the filling phase. To gain a better understanding of vortices during the cardiac cycle, they initially used a truncated prolate spheroid geometry to model the LV (Baccani *et al.*, 2002*a*). They studied the formation and separation of the vortex sheet that was generated from the inlet edge of the mitral valve. The results were described in terms of vorticity. They observed the detachment of a vortex ring from the inlet edge and a subsequent movement of the vortex ring towards the apex. In a subsequent study,

they studied the effects of the mitral valve on LV fluid dynamics using a generic model for the mitral valve (Baccani *et al.*, 2002*b*). A series of boundary conditions were used to mimic the effect of the opening of the mitral valve leaflets (Baccani *et al.*, 2003). They showed that the vortex wake formed during the rapid diastolic phase is more complex in the presence of new boundary conditions that treat the mitral valve operation in a more complex fashion. These models utilised axisymmetric assumptions and ignored the effects of 3D flow.

From a theoretical viewpoint, but also relevant, pulse flow in a cylindrical duct was investigated by Bolzon *et al.* (2003). They studied the initial stages of development of the 3D wake as flow entered the duct through a non-centralized circular orifice. They discovered that a small eccentricity produced a 3D vortical wake. The movement of the vortex ring was suggested to be a result of viscous forces and the wall boundary layer. The model of Baccani *et al.* (2002*a*) was further extended by Domenichini *et al.* (2005) to investigate 3D flow movement in a ventricular-shape geometry. Geometry, flow and eccentricity parameters were varied, and the resulting fluid-flow characteristics analysed. They discovered that the characteristics of the inlet jet had a direct effect on the solution. Pedrizzetti & Domenichini (2005) used a similar methodology to their previous studies to focus on the LV asymmetry. A different inlet jet model of the LV cavity was used to provide the asymmetry. They showed that in their heart, flow patterns were optimal for the minimization of energy dissipation and vortex formation from the shear layer of the mitral valve jet. The results obtained were validated experimentally by Domenichini *et al.* (2007) using an 3D axisymmetric model of the LV.

Domenichini & Pedrizzetti (2011) subsequently studied the change in fluid characteristics for an infarcted left ventricle using a similar methodology as for their previous studies. They discovered that blood travel towards the apical area (apex of the heart) was hindered in the presence of apical akinesia (lack of motion of LV wall) and further restricted in dyskinesia conditions (irregular motion of LV wall).

Generic simplified models are unable to capture the full nature of fluid flow in

the LV because they model the geometry as a portion of a prolate spheroid under axisymmetric assumptions. Additionally, these previously mentioned studies only investigated the blood flow in the LV during the diastolic (filling) segment. Although they provide some insight into the complex flow patterns in the LV, they are not realistic in their predictions of flow in an actual LV.

2.3.2 Geometry-defined MRI/CFD method

This method uses patient-specific MRI data to derive the boundary movement of the LV wall. It therefore provides more realistic boundary conditions and left ventricular mechanics compared to generic models. It uses an Arbitrary Lagrangian-Eulerian (ALE) formulation of the Navier-Stokes equations which allows boundary mesh motion.

The ALE-finite volume method was used by Saber *et al.* (2001) to model fluid flow in the LV. They used the commercial CFD software STAR-CD (Computational Dynamics Ltd., London, UK). Orifices were used instead of valves and a uniform velocity profile was applied as a boundary condition at the orifices during systole and diastole. Circulation of blood flow below the mitral valve was seen. They further developed and extended their previous study through a study where they appended a portion of the ascending aorta and left atrium to the LV model (Saber *et al.*, 2003). During the filling phase, a small posterior and a large anterior counterclockwise vortex were observed.

The choice of inlet boundary conditions on the resulting LV fluid dynamics was investigated by Long *et al.* (2003) using CFD software CFX4 (CFX international, AEA Technology, Harwell). Hybrid and pressure boundary conditions were applied at the inlet, and a sensitivity analysis carried out. They discovered that flow patterns were understandably highly sensitive to the chosen inflow boundary conditions. LV blood flow patterns were investigated by Long *et al.* (2008) in a further study using MRI data from six normal cases. A similar methodology to their previous studies was used (Long *et al.*, 2003). A primary counterclockwise vortex was observed

during the relaxation phase in three cases, and a clockwise vortex seen for one of the cases.

Four different types of mitral valve models were examined by Nakamura *et al.* (2006) to assess their effects on haemodynamic flow patterns in the LV. A 3D axisymmetric geometry of the LV was used. The mitral valve was modelled as a 2D circular orifice without leaflets, and the opening area varied over the cardiac cycle. Four different methods for opening of the mitral valve were used, and the results demonstrated that flow patterns were different for each type of opening. This has the potential of being important for the efficient design of artificial heart valves.

LV blood flow was simulated by Schenkel *et al.* (2009) in a model of the LV that included 2D presentation of valves. The time-varying area of the opening was modelled by projecting the valves' areas onto a circular surface. The upstream regions of the mitral and aortic valves were modelled using a more accurate interpolation method (third-order Bezier interpolation) compared to previous studies. They concluded that the asymmetric development of the initial vortex ring was due to the asymmetric inlet flow through the mitral valve. The vorticity and velocity distributions, which can be important in identifying cardiac disease, exhibit a complex association in the formation of a thrombus (Taylor & Draney, 2004). The quantification of certain parameters of blood flow such as pressure gradients, wall shear stress (WSS) and energy loss (EL) can provide diagnostic and treatment assistance by identifying unfavorable haemodynamic conditions that are indicators of disease progression (Ebbers *et al.*, 2002; Stalder *et al.*, 2008; Harloff *et al.*, 2010; Donati *et al.*, 2015). Thereby, CFD can assist in predicting haemodynamic patterns, allowing the early recognition of disease stages and helping to reduce patient risk.

Using computational fluid dynamics for predicting blood flow can provide us with higher temporal and spatial resolutions compared to 3D fields from MRI, especially in certain regions (such as near a blood-vessel wall or at valve leaflets). CFD has been used in the past to evaluate the wall shear stress and flow energy loss for patients afflicted with cardiovascular diseases (Itatani *et al.*, 2009; Qian *et al.*, 2010;

Sughimoto *et al.*, 2014; Koyama *et al.*, 2016; Sughimoto *et al.*, 2016).

Khalafvand *et al.* (2018) presented a new framework to simulate and analyze LV blood flow. Five unique 4D shapes (Mean, Mode 1 ± 3SD and Mode 2 ± 3SD) of 150 subjects were derived using statistical shape modelling. This process covers generalized LV shape changes over the cardiac cycle. Given a population of corresponding points from the segmentation of short axis contours over 150 patients, a mean shape was extracted and a set of variation modes can be built. Any subsequent novel shape from an individual can be represented as the mean shape varied by a linear weighted combination form of the initial modes. CFD simulations were then performed using these five shape sequences to understand the effects of shape changes on LV blood flow dynamics. The results were validated against particle image velocimetry (PIV) results obtained from a constructed articial model, and showed broad agreement. However, their study was limited as it was validated against two component planar PIV measurements rather than 3D three-component PIV. Their study also failed to characterize or account for the underlying clinical data of the patients. Thus, variations in flow dynamics were not associated with a particular cardiac dysfunction. In a previous study, Khalafvand *et al.* (2017) investigated the kinematic, dynamic and energy characteristics of flow during the diastolic phase in a normal left ventricle motion. They found that the total energy delivered from the ventricular wall to blood was conserved in the ventricle during diastole, as a momentum transfer was observed from the main flow to vortices during the end diastolic acceleration and deceleration phase. Moreover, a large counterclockwise core vortex was formed by the diastolic deceleration. The energy conservation and momentum transfer from the main flow to the vortices indicates healthy cardiac function. Loss of energy due to dissipation and shear stresses can be an indicator of cardiac dysfunction such as aortic regurgitation, a disease where a faulty aortic valve allows blood flow from the aorta back into the left ventricle during ventricular diastole.

Nguyen *et al.* (2015) developed a semi-automated method for simulating blood flow in a patient-specific LV. Similar to other computational studies, they developed

the geometric model from CMR images and translated the dynamic motion of the LV walls into mesh motion. They used the semi-automated method to analyse differences in blood flow dynamics between healthy patients and those with diastolic dysfunction. They found that patients suffering from diastolic dysfunction had lower vortex formation times than the healthy patients. Their study failed to validate the results against experimental/clinical data. They also made the assumption that the mitral and aortic valve open and close instantaneously which is physiologically inaccurate. An earlier study by Gharib *et al.* (2006) showed that a healthy range for the vortex formation time was between 3.5 - 5.5. Vortex formation times less than 3 were associated with impaired cardiac function, and in this study seen with patients suffering from dilated cardiomyopathy.

Su *et al.* (2014) recruited one patient with hypertrophic cardiomyopathy (HCM) and one healthy volunteer, who both underwent magnetic resonance imaging scans. Hypertrophic cardiomyopathy is a disease similar to dilated cardiomyopathy wherein the heart function is impaired due to an alteration of the heart muscle. In HCM however, heart muscle expands and causes the ventricular walls to thicken, potentially blocking blood flow out of the left ventricle. The patient-specific geometries were reconstructed from these, and both spatial and temporal interpolations were applied. The results showed that the HCM patient had *cirrostratus-cloud-like* vortex structures (generally uniform and thin in diameter) rather than a major vortex ring that was observed in the healthy subject. This suggests that the predicted vortex structures from computational fluid dynamics simulations have the potential to diagnose HCM (Su *et al.*, 2014).

Although the number of computational studies carried out are extensive, they often lack in two aspects. First, they lack validation against experimental data from echcocardiographic or cardiac magnetic resonance imaging data. This raises a concern regarding the accuracy of the simulation. Second, the computational studies rarely compare results between healthy and sick patients over a wider sample size. Single computational studies, although valuable, are not necessarily able to

accurately describe or predict the wider cardiac pathologies that can exist.

2.4   Summary

The LV can be modelled using three distinct methods: geometry prescribed methods, immersed boundary methods and FSI methods. Each of the different ways of modeling the LV should be used in their own way and should not be considered as alternatives to each other (Schenkel *et al.*, 2009).

Two alternative geometry prescribed CFD methods were discussed. Generic models provide an easier way to model and treat *an approximate* LV geometry, but still provide some of the basic elements of LV flow dynamics, that can help to better understand large-scale intraventricular fluid dynamic patterns.

On the other hand, the combined CFD/MRI method provides a realistic depiction of the boundary motion of the LV, and the results can be validated better (Long *et al.*, 2008; Schenkel *et al.*, 2009). In the present study, a combined CFD/MRI method is developed based on a dynamic mesh routine to describe the movement of the ventricle walls. This approach can be applied directly to patient-specific MRI data for LV wall motion. This method has been recognized by the literature to provide considerable potential utility for clinicians.

Chapter 3

Methodology

3.1 Introduction

In this chapter, the methodology underlying the residence time distribution analysis and CFD modelling is described. First, the MRI data acquisition and processing is explained. This is followed by an explanation of the process of obtaining residence time distributions from particle tracing data and evaluation of the RTD constant. This chapter concludes with an explanation of grid generation, governing equations, dynamic mesh method and boundary conditions.

3.2 MRI data acquisition and image processing

MRI is a non-invasive diagnostic technique for assessing heart function and dysfunction. Compared to other methods such as X-ray and computed tomography (CT), MRI is considered safer (Schenck, 2000; de González & Darby, 2004).

The availability of access to a high-resolution 3T (Tesla) Siemens MAGNETOM Prisma MRI scanner at the Baker Institute in Melbourne for this project (see Figure 3.1) has permitted blood flow through the cardiovascular system to be captured with greater temporal and spatial resolution than was previously available from lower powered scanners. The Tesla rating quantifies the magnetic field strength produced by the magnet in the scanner.
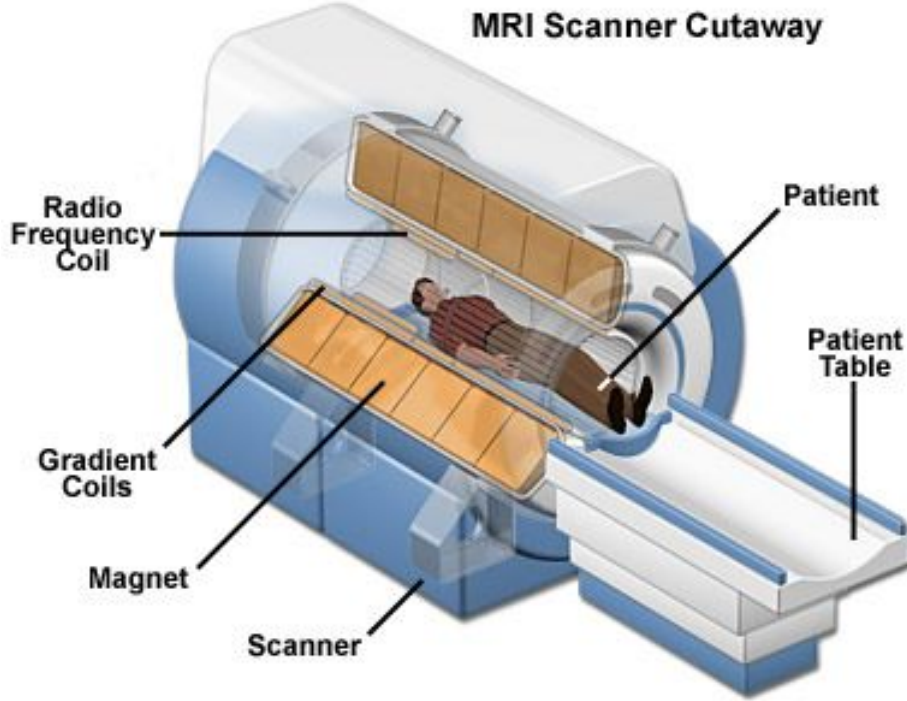
Figure 3.1: Siemens MAGNETOM Prisma scanner (Siemens, 2015).

The majority of the existing research has been carried out on 1.5T MRI scanners. 3T scanners provide higher spatial and temporal resolution because the signal to noise ratio (SNR) is approximately twice that of a 1.5T scanner. The improved SNR can be utilized to improve the quality of the images and to decrease overall scan time.

After acquiring *scout* images, *cine-imaging* (i.e. time-resolved) of the heart in standard 4-, 3-, and 2-chamber long-axis and short-axis views (see Figures 3.2 and 3.3 for orientation) through the left ventricle was performed using a MRI pulse sequence that has a steady state of magnetisation (also called as steady-state free precession or its abbreviation SSFP). This sequence is known for its superiority in its assessment of cardiac function. A stack of 15 sequential short-axis steady-state free-precession cine images was acquired, extending from the mitral valve region to the left ventricle (LV) apex (8-mm slice thickness, no gap), to enable volumetric analysis of the left ventricle using the Simpson summation of disk method. This method uses the short-axis images of the LV to obtain the LV ejection fraction (LVEF). Borders are manually traced on each short-axis image to represent the
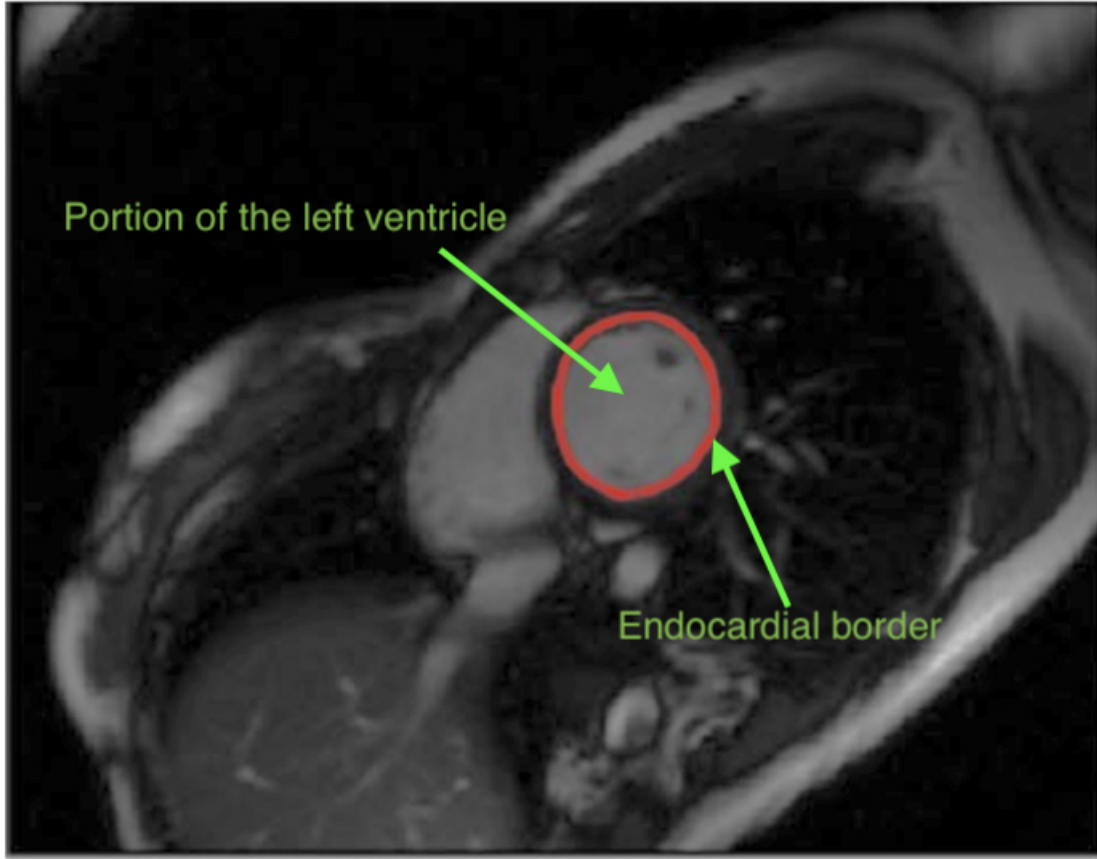
Figure 3.2: Short-axis view of LV in Segment CMR. The red boundary encloses the ventricular cavity.

LV endocardium (membrane that lines the inside of the heart chamber), thereby obtaining the ventricular cavity area for each slice as seen in Figure 3.2. The area enclosed by the border for each image slice was multiplied by the sum of the image gap and slice thickness (slice interval) to provide the slice volume. The total LV volume is then obtained by adding the volume of all slices. The shape of the LV is determined using this method as the entire LV cavity is traced. The use of high contrast will result in a well-defined endocardial border being obtained. It is in this way that the LVEF can be calculated using MRI whilst not requiring the injection of contrast material or ionizing radiation.

In-plane spatial resolution was 1.5mm. Each slice was acquired separately, and there were 25 temporal phases per heart cycle. The complete image acquisition process required 30 minutes. The short- and long-axis views obtained from the MRI were used to carry out a 3D reconstruction of the LV using a customized algorithm
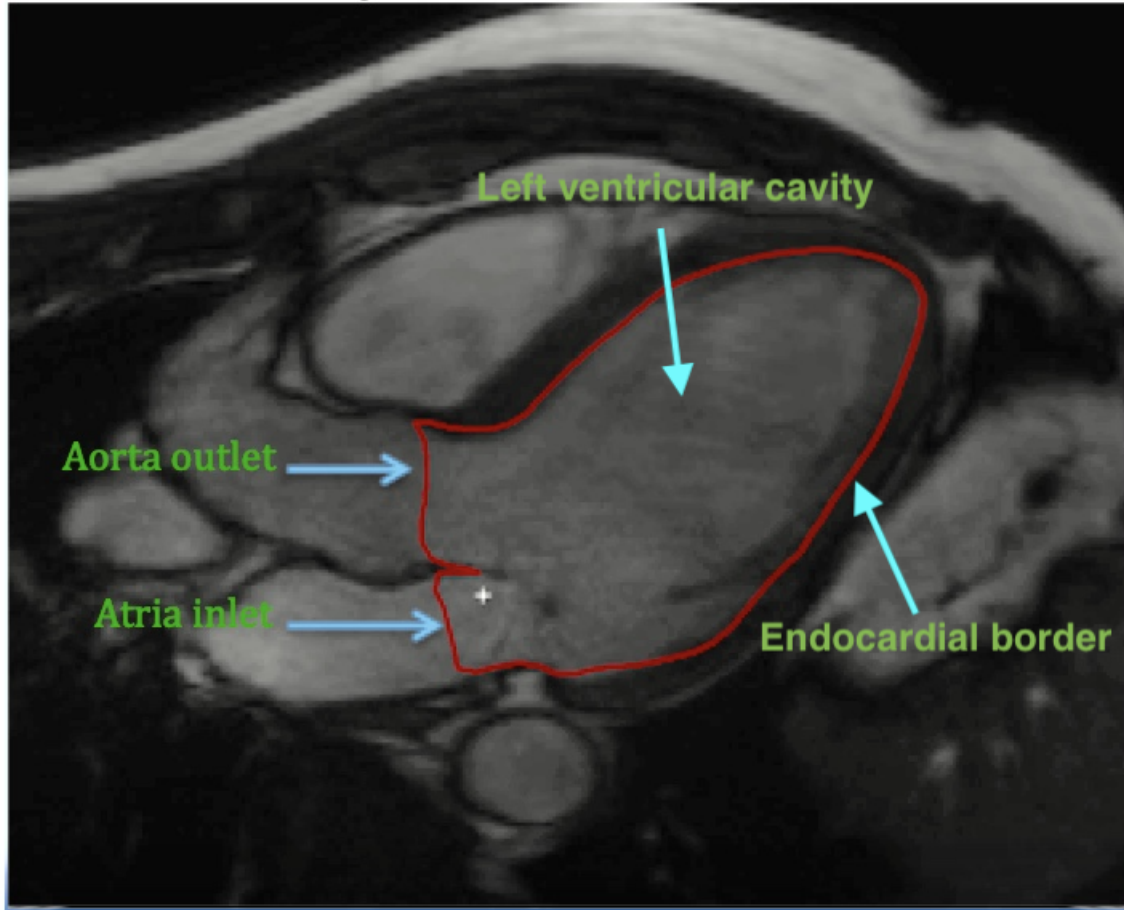
Figure 3.3: Long-axis view of the LV in Segment CMR. The red boundary signifies the ventricular cavity.

discussed below.

3.3 RTD Methodology

Post-processing of MRI 2D images using *Argus Flow* (a proprietary software provided by SIEMENS) produced two immediate sets of data: particle-tracking data and the locations of planes created in the SIEMENS software. The particle-tracking data contained the three-dimensional position and velocity for each seeded particle seeded as it was tracked through the heart. Code was developed in MATLAB to import the particle-tracking data using text scanning methods. Each data set ordinarily contained 1000-1300 timesteps, each of duration 0.00425 seconds, and containing around 2000-3000 distinct particles. This data was refined to remove particles that did not exit the chamber and to exclude particles that were being

tracked outside the walls of the chamber. To remove non-exiting particles from the analysis, a virtual 'particle seeding' plane was created in the software at the atrioventricular valve (in between the left atrium and left ventricle) as shown in Figure 3.4. This was defined as the entry plane. The exit plane was defined at the proximal ascending aorta. Particles were seeded uniformly, on the portion of the entry plane that was detected to be inside the blood flow for a short period of time relative to the cardiac cycle time. These particles were then moved with the measured velocity field over five complete cardiac cycles. As they passed through the heart, they were counted as they crossed the exit plane at the ascending aorta, and their time stamp noted. A schematic of the planes generated in MATLAB is shown in Figure 3.5
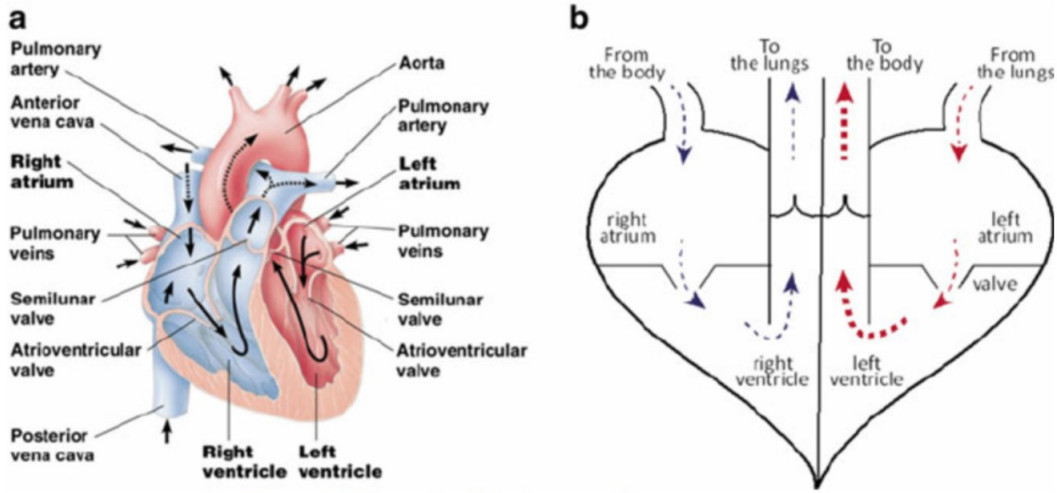
Figure 3.4: Heart schematic and its compartments.

RTD graphs were created in MATLAB using in-house code over the 5 heartbeats. The raw RTD graph, with smoothing, is presented in Figures 3.6 and 3.7. The residence time distribution function, $E(t)$, is expressed as:

$$E(t) = \frac{C(t)}{\int_0^\infty C(t)\, dt} \tag{3.1}$$

where $C(t)$ is the calculated number of particles crossing the exit plane at time t. The $E(t)$ curves express the proportion of all departing particles that cross the exit plane over sequential given specified time intervals (with time defined on the horizontal axis).
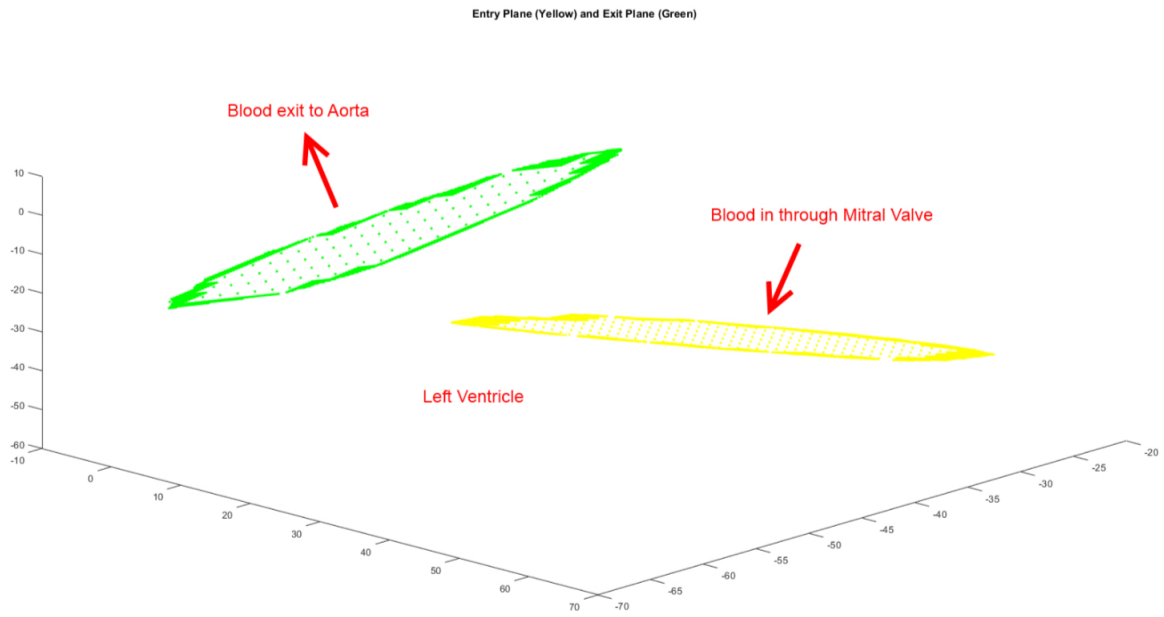
Figure 3.5: Planes generated in MATLAB. Yellow plane depicts the entry plane, and the green plane is the exit plane.
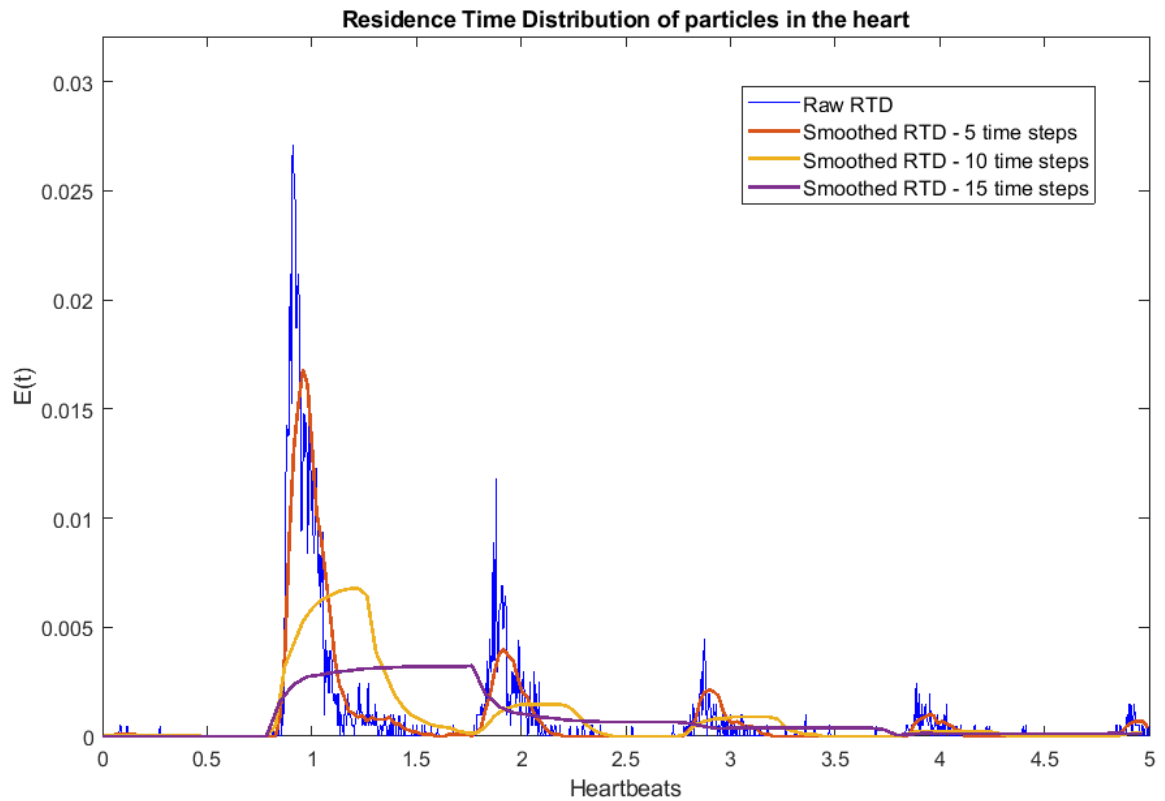
Figure 3.6: Raw RTD graph shown with the various smoothed graphs.
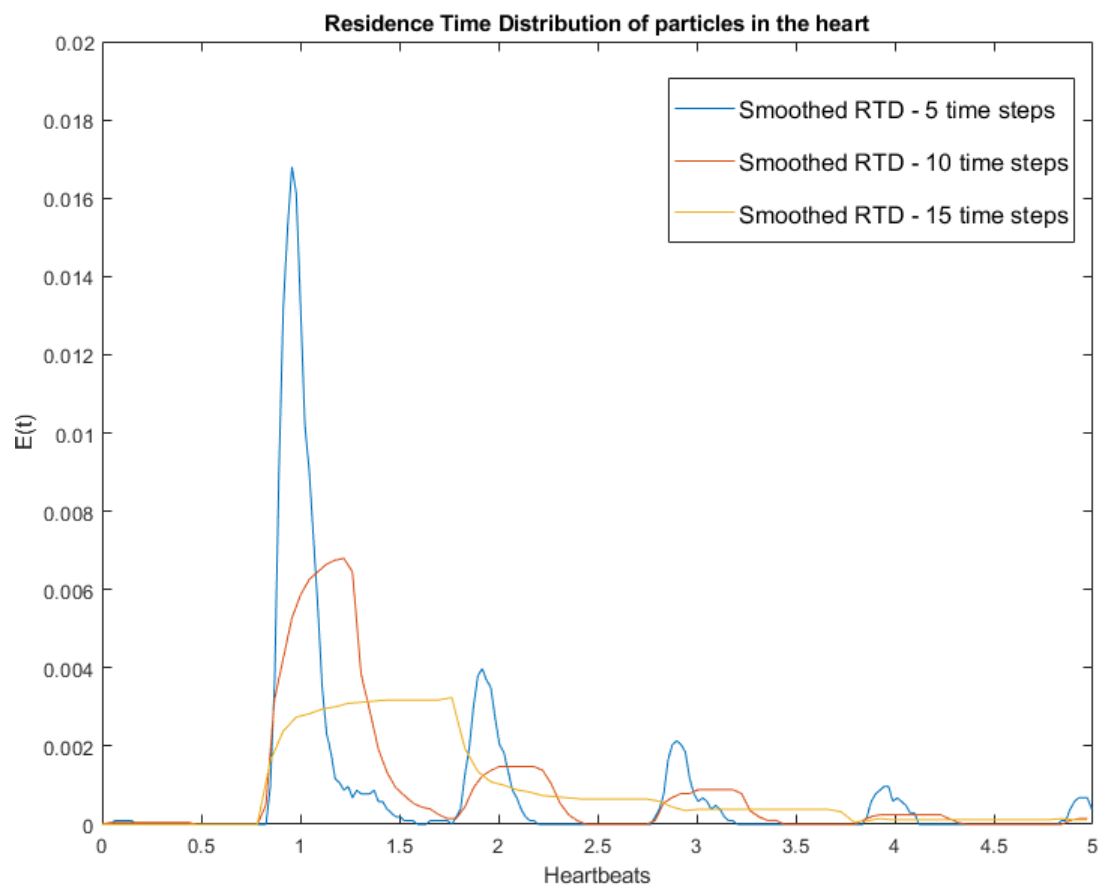
Figure 3.7: Smoothed RTD curves comparing between 5, 10 and 15 time steps.

This function describes in a quantitative manner how much time different fluid elements have spent in the vessel. For comparisons between patients, the distributions are normalized to 5 heartbeats, which when referenced at 60 beats per minute (bpm) is a time period of 5 seconds in length. The RTD data was smoothed because there was a considerable fluctuation between the number of particles exiting at consecutive time points, making it difficult to interpret the data. The length of 5 time steps for smoothing was selected after testing with 5, 10 and 15 time steps as seen in Figure 3.6 and Figure 3.7. It appears 5 time steps provided the best compromise between showing the prominent peaks at each heartbeat and their approximate height.

The data can also be plotted as a fraction of the total particles, $F(t)$, remaining in the ventricle as a function of heartbeats (i.e. time) as expressed by:

$$F(t) = 1 - \frac{\int_0^t C(t)\,dt}{\int_0^\infty C(t)\,dt} \tag{3.2}$$

An exponential decay function of the form $y = Ae^{-bt}$ was fitted to the value of the fraction of particles remaining over time and the performance of ventricular pumping was determined based on the time constant $(RTD_c = \frac{1}{b})$ of the exponential decay curve as seen in Figure 3.8. The variation of this parameter for different patient cohorts can then be evaluated and compared to clinical markers, such as the ejection fraction, T1 values and GLS, to determine if it is a useful predictor of heart dysfunction.
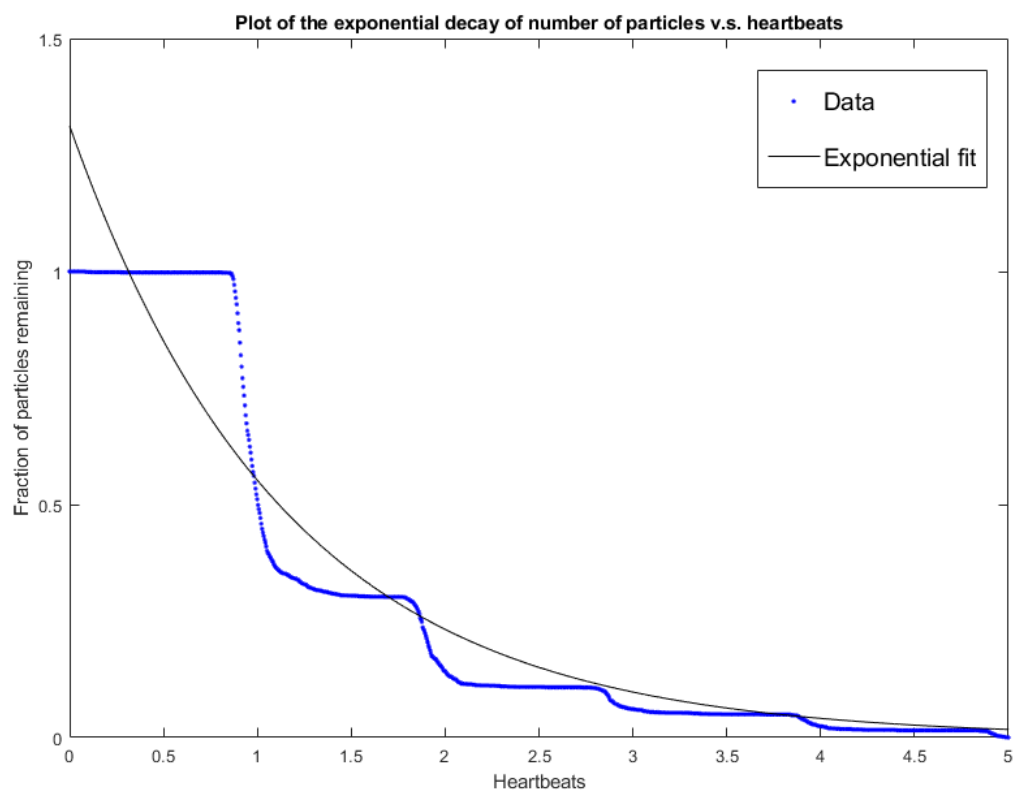
Figure 3.8: Fraction of particles remaining in the heart over heartbeats. Exponential fit to the entire data set is shown.

3.4   Geometry reconstruction and grid generation

The positional data obtained from the short- (see Figure 3.2) and long- axis views (see Figure 3.3) were in the *voxel* co-ordinate system. To use them for the 3D reconstruction of the LV, the 2D positional data had to be transformed from the *voxel* to the 3D DICOM patient co-ordinate system (DPCS).

Digital Imaging and Communications in Medicine (DICOM) is a global standard used in medical imaging for storing, printing, handling and transmitting information.

The 3D DICOM patient-based coordinate system uses the orientation of the patient to define the x, y and z axes. The x-axis increases to the left hand of the patient, the y-axis increases to the posterior side of the patient and the z- axis increases towards the head of the patient (as seen in Figure 3.9). An image slice is stored as a single DICOM file that contains the following objects. The pixel array contains the values of the pixels of a particular slice. In pixel coordinates, (c, r) is the pixel in column c and row r. The positional data from the short- and long-axis views was exported in this format. A slice also contains the Pixel Spacing attribute $(\Delta r, \Delta c)$. The column spacing in mm, Δc, refers to the spacing between the centres of adjacent columns, or the horizontal spacing. The row spacing in mm , Δr, refers to the distance between the centres of adjacent rows, or the vertical spacing.

In order to transform the voxel coordinates of a slice of an image to the DPCS, two attributes are used: the Image Position and Image Orientation. The Image Position attribute contains three values (S_x, S_y, S_z) that define the position of the origin of the image slice in mm relative to the reference patient coordinate system. The Image Orientation attribute defines the positive row axis that has the direction of the last pixel in the first row from the first pixel in that row, and the positive column axis which describes the direction of the column. The Image Orientation attribute therefore defines two axes, which are stored as direction cosines of the axes relative to the patient coordinate system. The row axis is stored as (X_x, X_y, X_z) and the column axis as (Y_x, Y_y, Y_z). Because the Image Orientation is stored as direction cosines, X_{xyz} and Y_{xyz} are the values of the cosines of the angles between the
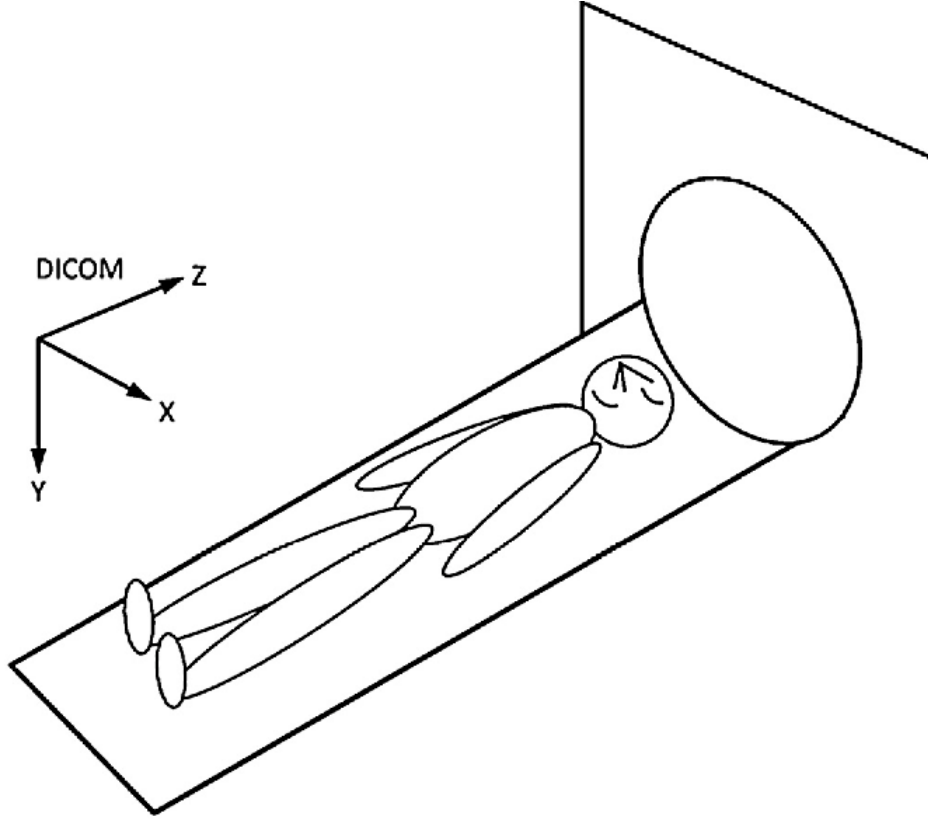
Figure 3.9: Schematic of the DICOM coordinate system.

three patient coordinate axes and the row and column directions respectively. Pixel coordinates (c, r) are mapped to the patient coordinate system using the following equation:

$$\begin{bmatrix} P_x \\ P_y \\ P_z \\ 1 \end{bmatrix} = \begin{bmatrix} X_x \Delta c & Y_x \Delta r & 0 & S_x \\ X_y \Delta c & Y_y \Delta r & 0 & S_y \\ X_z \Delta c & Y_z \Delta r & 0 & S_z \\ 0 & 0 & 0 & 1 \end{bmatrix} \begin{bmatrix} c \\ r \\ 0 \\ 1 \end{bmatrix} = A \begin{bmatrix} c \\ r \\ 0 \\ 1 \end{bmatrix}. \tag{3.3}$$

This equation defines the transformation that maps the voxels of a particular slice from the voxel space to the DPCS. The MRI images are taken at regular intervals along the length of the LV, and this forms a stack of images stored as DICOM images (also called a volume in DICOM terminology). The Image Orientation attribute is the same for each slice. Voxel coordinates can now be expressed in the form (c, r, s) i.e. the column, row and slice indices. To map the voxels in the volume to the DICOM patient coordinate system, a modified form of equation 3.3 is utilised.

Values (k_1, k_2, k_3) are added to the first three rows of the third column of the matrix in Equation 3.3. In a volume containing N slices, slice numbers vary from 0 to $N-1$. The transformation equation can now be expressed as:

$$\begin{bmatrix} P_x \\ P_y \\ P_z \\ 1 \end{bmatrix} = \begin{bmatrix} X_x \Delta c & Y_x \Delta r & k_1 & S_x \\ X_y \Delta c & Y_y \Delta r & k_2 & S_y \\ X_z \Delta c & Y_z \Delta r & k_3 & S_z \\ 0 & 0 & 0 & 1 \end{bmatrix} \begin{bmatrix} c \\ r \\ s \\ 1 \end{bmatrix} = A_{multi} \begin{bmatrix} c \\ r \\ 0 \\ 1 \end{bmatrix} \qquad (3.4)$$

where vector $\mathbf{k}$ can be obtained by subtracting the Image Position vector of slice 0 from that of slice $N-1$.

Beyond this, an algorithm was developed and implemented that corrects for motion distortions in the MRI images. These distortions arise due to patient breathing and motion during the MRI scan (recalling the acquisition time is 30 minutes). This method involved manual delineation (where the closest point on a geometric shape is computed from a given point) and registration (computing a least squared registration vector) based on a generalized, iterative closest point algorithm as developed by Besl & McKay (1992). The algorithm uses the positional data from the long-axis and short-axis images to minimize the sum of the squared differences between the coordinates from the two sets of points. A constraint was put into place in the current implementation that only translation of the points is carried out with no rotation. It was seen that when rotation was permitted that the resulting point cloud, although minimized the squared distances, did not appear as a representative point cloud of the left ventricle.

This positional data was transformed using a multi-step algorithm that resulted in a geometric surface that could be used in software such as ANSYS-Fluent to carry out the CFD simulation. This involved: (1) interpolation of the contour data between the contour levels as seen from Figure 3.10 to Figure 3.11, (2) development and implementation of a Delaunay-based triangulation method for the surface reconstruction from this scattered point cloud data as seen in Figure 3.12. Although
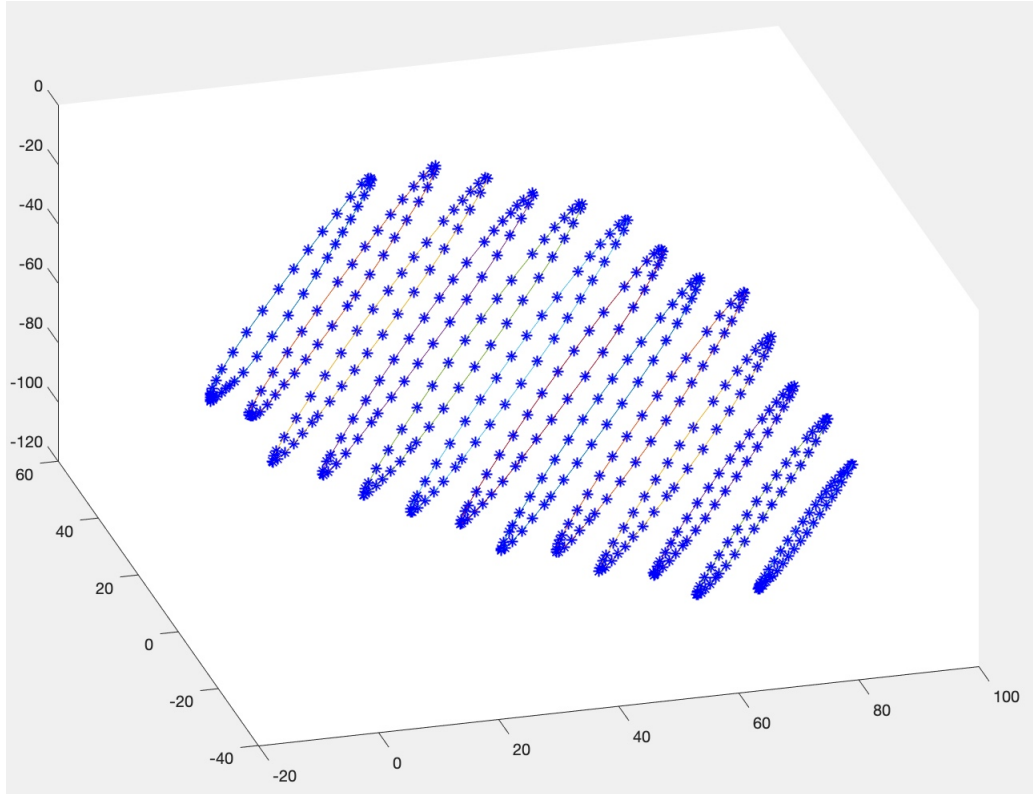
Figure 3.10: Contour data defining the inside surface of the LV depicted by the connected blue dots obtained from short-axis images.

the Delaunay-based triangulation method is the preferred mode for obtaining the surface geometry, holes may be found on the surface, as they were seen in Figure 3.12. Patching these holes requires a significant amount of time and attention to detail. Therefore, an alternative, faster method of obtaining the surface geometry was used. The reconstruction of the LV surface geometry for CFD simulation was carried out using a semi-automated method. Here, the set of short-axis contours were imported into SolidWorks. The *Loft* tool was used to generate the surface geometry. The *Loft* feature smoothly interpolates between the short-axis contour profiles to create the shape of the LV. It is able to do so by adding material between the contour profiles as seen in Figure 3.13.
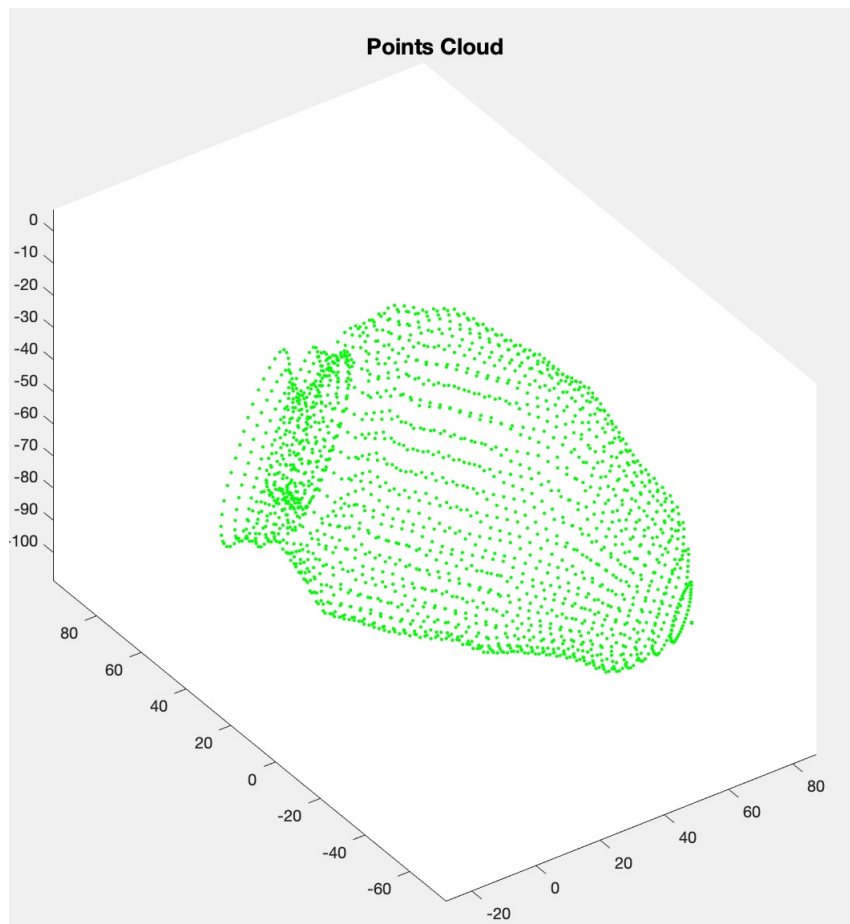
Figure 3.11: Interpolated schematic of the contour data to obtain a representative point cloud of the LV.
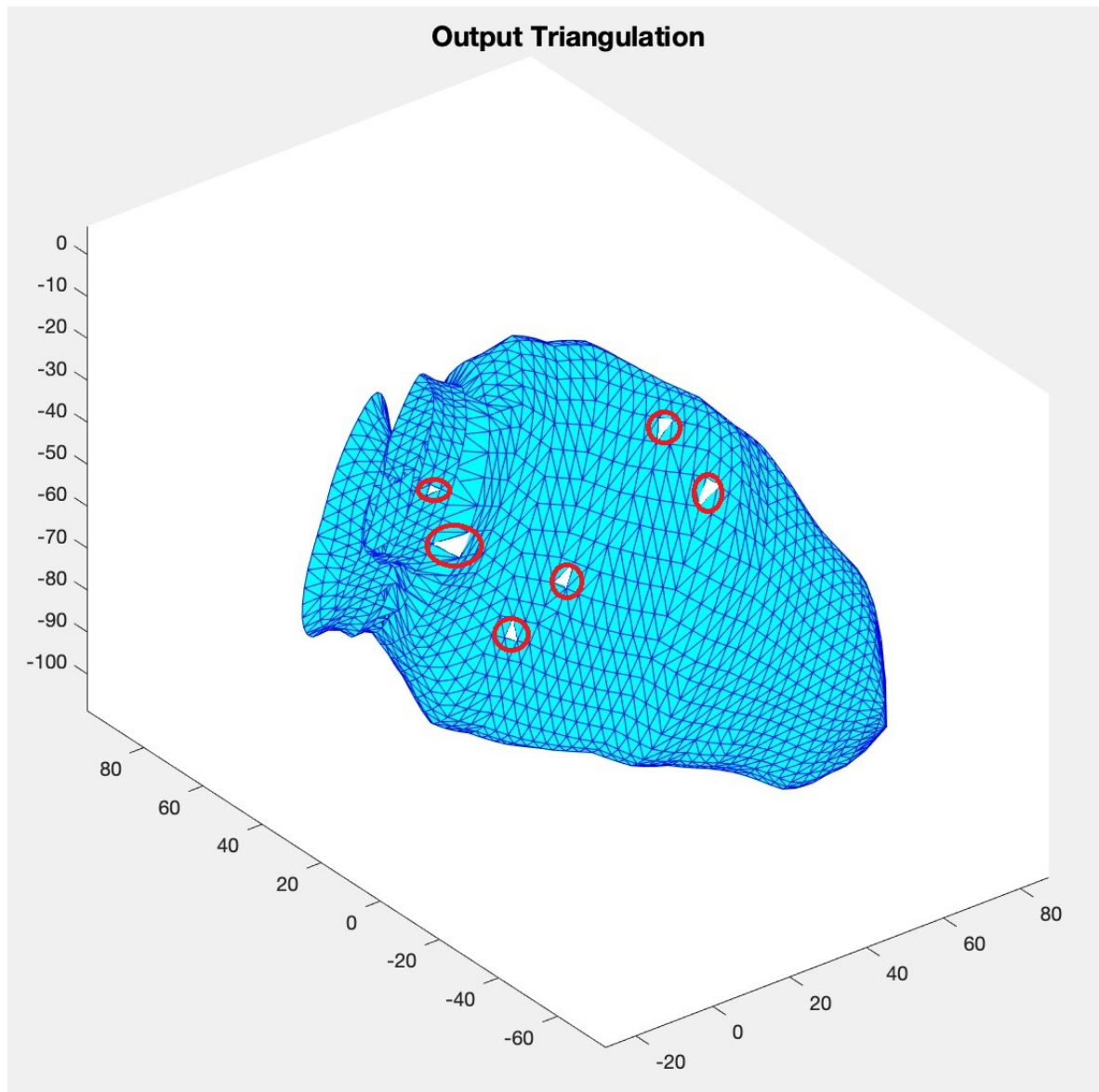
Figure 3.12: Surface mesh obtained from Delaunay triangulation of point cloud data. Red circles denote holes in the surface mesh.
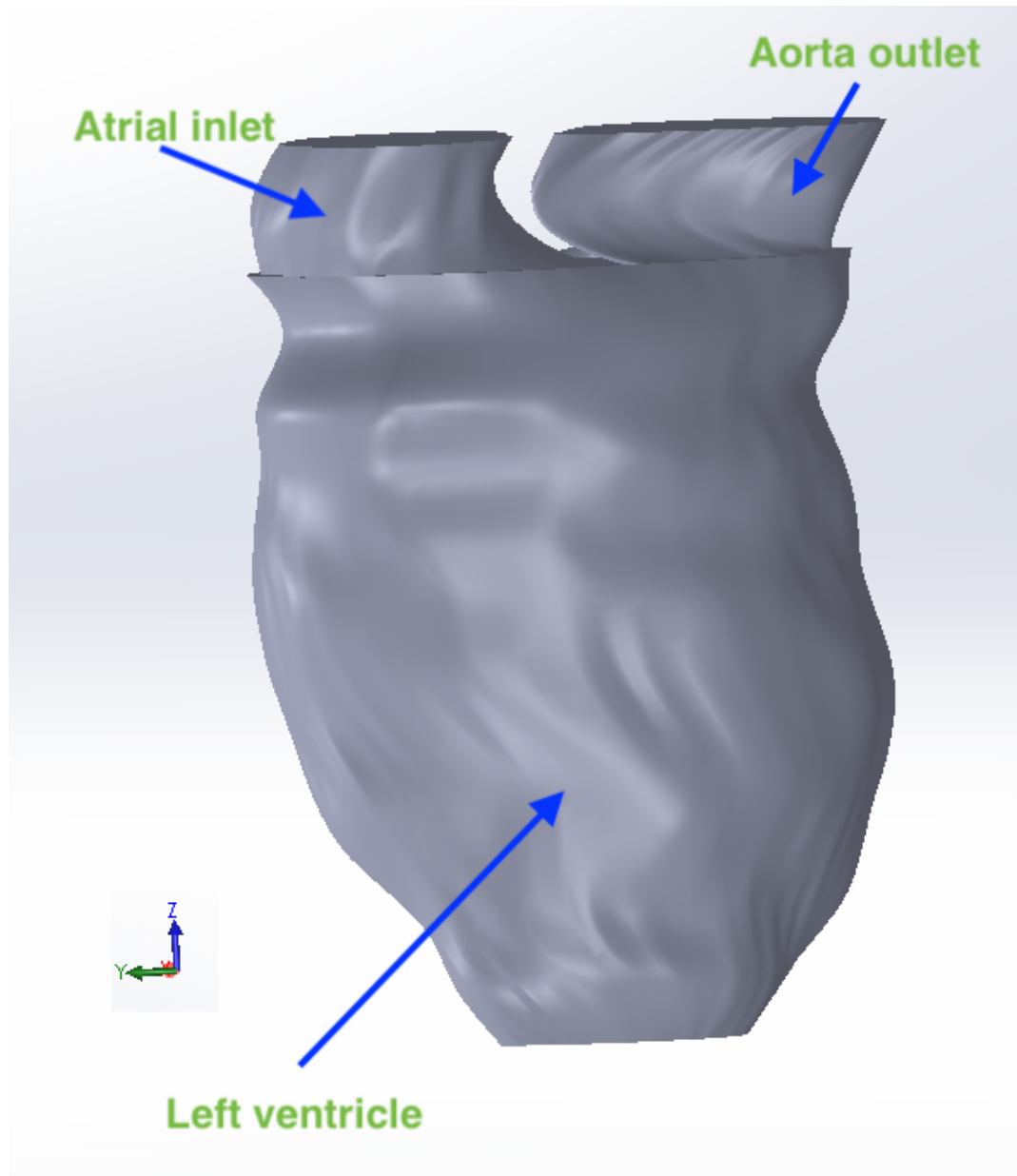
Figure 3.13: Patient-specific volume geometry of left ventricle with aorta outlet and atrial inlet reconstructed from 2D MRI images.

3.5   CFD simulation and boundary conditions

3.5.1   Geometry reconstruction and grid generation

For the reconstructed geometry, a set of unstructured meshes consisting of tetrahedral cells for 3D modelling were generated in ANSYS-Fluent. It should be noted that in the initial stages of the thesis program, both structured and unstructured grids were generated to model the LV and to test the correct operation of the dynamic mesh routine. However, for all subsequent cases, unstructured grids were used because most modern CFD solvers allow use of unstructured grids and accommodates the complex geometrical nature of the left ventricle with atrial inlet and aorta outlet. A grid-independence study was carried out to obtain spatial convergence of the CFD solution. The number of grid elements were increased by a factor of 1.5 (8000, 12000, 18000, 27000 and 40500). Calculated flow velocities did not change as the number of cells were increased from 27000 to 40500. In the range from 18000 to 27000, the changes in flow features were minor. For more accurate results, the final number of cells chosen for the 3D modelling was 27000.

The time-spacing of 25 phases per heart beat cycle (supplied by the MRI phase-averaging process) was not sufficient for the CFD simulation as the model experienced considerable distortion, involving both translation and compression/expansion, over the cardiac cycle. A reduced timestep was required to model the changing volume and to ensure that the Courant number remained less than unity (product of the local fluid velocity with the ratio of time-step to mesh spacing $\frac{u \Delta t}{\Delta x} < 1$) (Ferziger & Perić, 1999). This is required for computational stability. The time step and mesh spacing that were found to satisfy the Courant condition and used for the simulations was 0.04 ms and 0.08 mm respectively.

3.5.2   Governing equations

To predict the fluid flow in the computational domain using the finite-volume method, the arbitrary Lagrangian-Eulerian (ALE) form of the Navier-Stokes solution is used

(Hirt *et al.*, 1974). The three-dimensional integral form of the continuity equation for an arbitrary volume V and surface S moving with local surface velocity of v_b (Hirt *et al.*, 1974; Ferziger & Perić, 1999) is given by

$$\frac{\partial}{\partial t} \int_V \rho \, dV + \int_S \rho(v - v_b) \cdot \mathbf{n} \, dS = 0 \tag{3.5}$$

where ρ is the density of the fluid, $v = (u, v, w)$ is the velocity vector of the fluid in the fixed coordinate system, $v_b = (u_b, v_b, w_b)$ is the velocity vector of the moving boundary (boundary S of control volume V) and $\mathbf{n}$ is the outward directed normal vector to dS.

The three-dimensional integral form of the momentum equation (Hirt *et al.*, 1974; Ferziger & Perić, 1999) is given by:

$$\frac{\partial}{\partial t} \int_V \rho v \, dV + \int_S \rho v(v - v_b) \cdot \mathbf{n} \, dS = - \int_S p\mathbf{n} \, dS + \int_S \tau \cdot \mathbf{n} \, dS \tag{3.6}$$

where p is the pressure and τ is the viscous stress tensor. In Equation 3.6, the gravitational force is included in p for a homogeneous fluid in a closed system. Assuming blood to be an incompressible Newtonian fluid, τ is expressed as:

$$\tau_{ij} = \mu \left(\frac{\partial u_i}{\partial x_j} + \frac{\partial u_j}{\partial x_i} \right) \tag{3.7}$$

Here, μ is assumed to be constant because blood flow in large vessels can be treated approximtely as a homogeneous Newtonian fluid. The density and dynamic viscosity used in this study are 1050 kg m^{-3} and 0.00316 Pa sec respectively. For the finite-volume implementation, these equations are discretised for each cell of the computational domain.

3.5.3 CFD simulation and boundary conditions

For the present application, two orifices (surfaces) are positioned at the top of the LV to represent the inlet and the outlet valves. Initial boundary conditions applied are an outflow boundary condition to the outlet (aortic valve) with a closed inlet

(mitral valve) when the LV is contracting, and a closed outlet (aortic valve), with a reversed outflow boundary condition applied to the inlet (mitral valve). Of course, this does not model the dynamical fluid-structure interaction of the opening and closing valves, but still is expected to provide a reasonable first approximation to the flow away from the valves.

The Navier-Stokes equations for three-dimensional flow with a dynamic mesh was solved using the finite-volume based CFD commercial solver ANSYS-Fluent (Ansys Inc 2019). An ALE formulation together with optional re-meshing is used by selecting the dynamic mesh option in Fluent. Fluent permits users to prescribe boundary motion using user-defined functions (UDFs). The UDFs to describe the LV boundary motion were programmed in C. The geometry was constructed from 15 horizontal slices from the base to the apex. To describe the motion of the boundaries, each slice was segmented into a set of angular segments about the centre of the slice. Boundary points could move outwards or inwards along a line of fixed angular positions (Saber *et al.*, 2001). A schematic of a single angular position for one slice is shown in Figure 3.14.
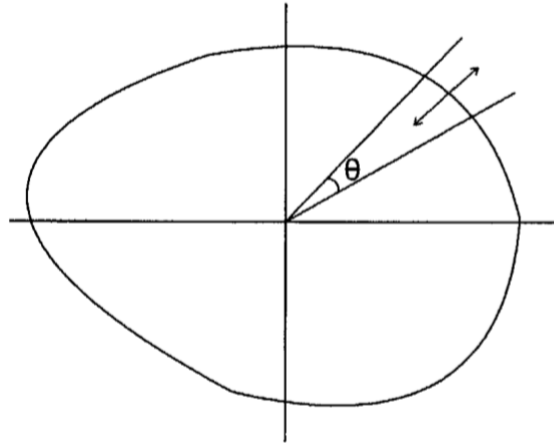
Figure 3.14: View of one angular position for one slice.

The motion of the boundary for all the slices over the heart beat cycle was defined for the solver by writing UDFs based on the raw MRI data, and the motion of points between slices was determined using linear interpolation. To obtain the surface velocity for the fitted grid, the difference between the former (t_{i-1}) and

current grids (t_i) were calculated. Mesh motion occurs due to the movement of the LV wall. To ensure the mesh could be used after the domain deformed, a mesh quality control measure was implemented. Here, the grid quality is assessed at each time step and the simulation halted if grid quality deteriorates to below a criterion. In the current work, the criterion for grid quality is that the maximum value of the face skewness must not exceed 0.9. Additionally, the spring-based smoothing method is used for the tetrahedral mesh. As the boundary displacement becomes much larger than the local cell size, a deterioration of cell quality can occur and the cells may degenerate. This will invalidate the mesh (i.e. result in negative cell volumes) and convergence problems will arise as the solution is updated to the following time step. To prevent this from happening, re-meshing is used in the regions where the mesh has degenerated and fallen below the acceptable grid quality criterion (ANSYS-Fluent 19 documentation, 2019). There are a number of different re-meshing methods that can be used depending on the problem. In the current work, a local re-meshing method is used. Using the local re-meshing method, Fluent marks cells based on cell skewness, minimum and maximum length scales as well as an optional sizing function. Each cell is evaluated by Fluent and marked for re-meshing if it satisfies the criterion. The re-meshing technique interpolates the previous time step results to the new mesh and continues the iteration. Further information about the different re-meshing methods is available in the ANSYS-Fluent documentation (2019). Figure 3.15 shows a diagram of CFD solution using a re-meshing loop. To achieve convergence and accuracy, a second-order upwind scheme was employed. The resulting algebraic equation system was solved using the implicit PISO (Pressure implicit with splitting of Operators) algorithm that is suitable for time-dependent flow problems (Issa, 1986).
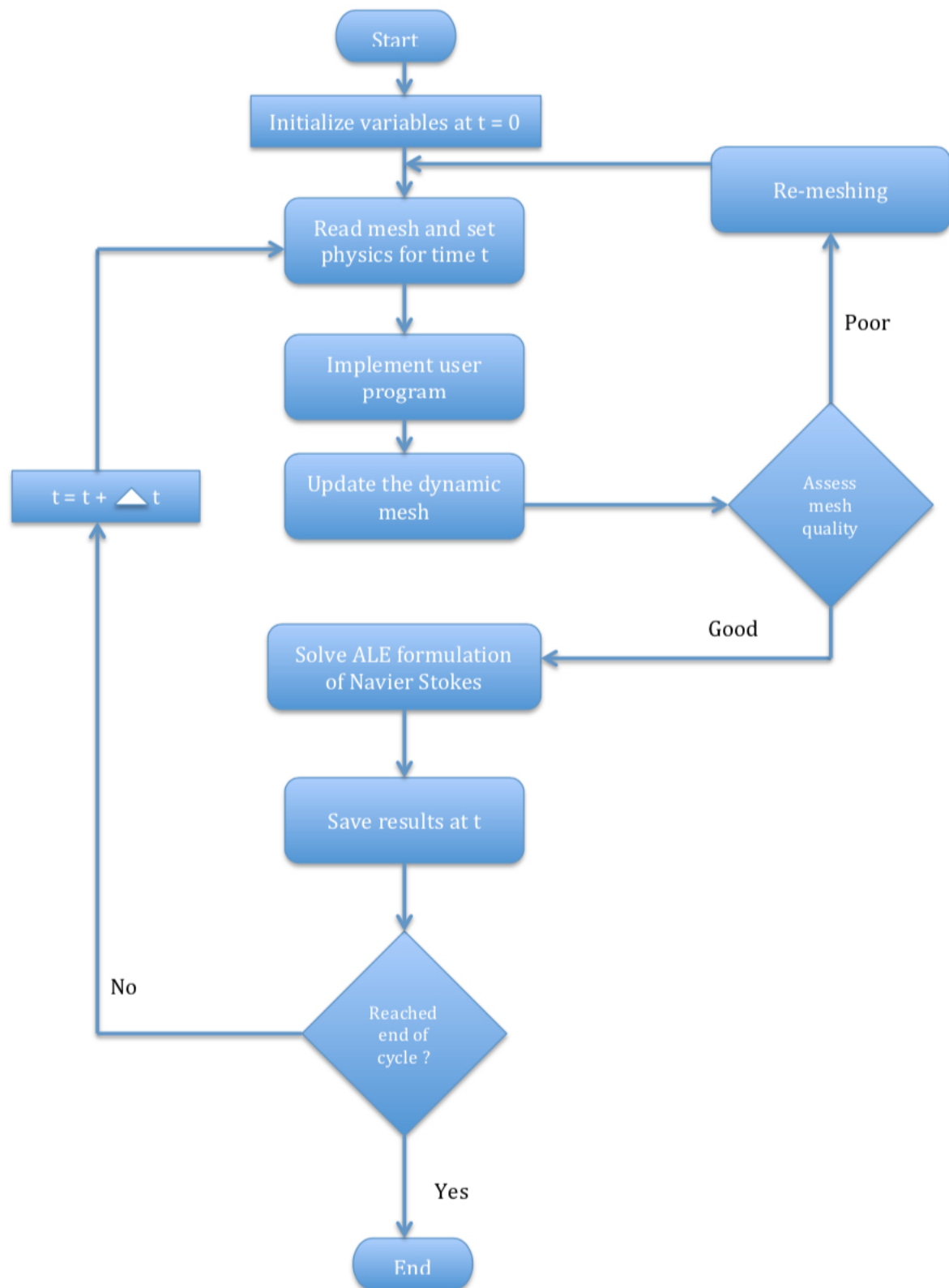
Figure 3.15: Simulation process with re-meshing.

3.6   Summary

In this chapter, MRI image acquisition and post-processing of the MRI data for the CFD model and RTD study have been described. MRI images were segmented and reconstructed for 25 frames in one (mean) cardiac cycle. The dynamic mesh capability of ANSYS-Fluent could be utilised using user-defined functions (UDFs) to describe the motion of the LV wall throughout the cardiac cycle. Smoothing and re-meshing methods allow a high level of grid quality to be maintained. RTD graphs generated from particle tracing data allow a time constant to be obtained by fitting an exponential decay function to the residence time distributions. The application of these methodologies will be examined in the following chapters. Chapter 4 will provide a description of applying RTDs to measure cardiac function in healthy patients and patients with dilated cardiomyopathy. Furthermore, the RTD constant will be compared to current diagnostic measures, particularly the ejection fraction, GLS and T1 values. An initial computational fluid dynamics model is developed and presented in Chapter 5. This model will highlight the intraventricular fluid dynamics, and present a detailed overview of the changing volume of the left ventricle over the cardiac cycle.

Chapter 4

Residence Time Distribution

4.1 Introduction

Phase-averaged blood flow dynamics within the heart can be captured reasonably accurately using cardiac magnetic resonance imaging. Patients with arrhythmia demonstrate a change in blood flow, and using 4D flow MRI (time-resolved blood flow) derived markers of cardiovascular function may aid clinicians in their diagnostic and prognostic endeavours. Patient-specific residence-time distributions of blood passing through a chamber can be obtained by post processing the measured flow data. RTDs can provide an understanding of mixing, stasis and overall blood flow, which have effects on cardiac function. In a way, the RTD differs from existing markers, such as the ejection fraction, as it investigates blood flow directly and contains extra information on blood "age", rather than the global volumetric mechanics of the cardiac cycle.

In this chapter, left and right ventricular 4D flow data from a healthy control group and patients with impaired left ventricular function is analyzed. RTDs of blood transiting the left and right ventricles were developed, and the relationship between RTD parameters and ejection fraction investigated. Furthermore, the relationship between the RTD and the global longitudinal strain (tissue function) and T1 value (tissue composition) is investigated to evaluate the ability of the RTD technique to distinguish normal and abnormal myocardial function.

4.2 Biodata for cases

The study involved sixteen normal subjects and sixteen patients with ventricular dysfunction. The healthy volunteers had normal blood pressures and did not report a history of diabetes, smoking or renal impairment. They were found to have normal CMR results (ejection fraction, ventricular size and mass index). Patients suffering from dilated cardiomyopathy were included in the study if they presented a history of symptomatic heart failure and a dilated left ventricle with an ejection fraction < 50%. A summary of the biodata is provided in Table 4.1. For the purposes of understanding the table, the following definitions are provided. The ejection fraction is calculated by taking the fraction of the volume of blood pumped out of the chamber against the total volume of blood in the chamber. The volume of blood pumped out per contraction is referred to as the stroke volume (SV). The total amount of blood collected in the chamber at the end of the filling phase is the end diastolic volume (EDV). In other words, the ejection fraction is the normalised stroke volume.

	Healthy Controls	Dysfunctional Cases
Number	16	16
Age(years)	43 ± 11	54 ± 14
Gender	7F/9M	6F/10M
LV End-Diastolic Volume (mL)	183 ± 46	225 ± 108
LV Stroke Volume (mL)	107 ± 27	75 ± 22
LV Ejection Fraction (%)	59 ± 5	35 ± 9
RV End-Diastolic Volume (mL)	174 ± 45	147 ± 42
RV Stroke Volume (mL)	96 ± 22	62 ± 21
RV Ejection Fraction (%)	63 ± 30	43 ± 12

Table 4.1: Demographics and clinical data for the RTD study.

4.3 Methods

The 4D flow image post processing duration (to draw and position the entry and exit planes) varied between 6 to 12 minutes per patient. The software provided by Siemens corrected for random noise and distortion in signal magnitude. A duration of approximately 10 minutes of computer processing was taken to obtain the RTD for each patient. The method used was explained in Section 3.3. The RTD time constants obtained from the RTD analysis are compared with the other accepted markers of cardiac performance to determine the extent (if any) of correlation between the measures. Statistical analysis of the data yields two values, R and p. R refers to the correlation coefficient which depicts the strength of the relationship between the relative movements of two variables. R ranges from 0 to 1, and a value of 0.9 implies that 90% of the observed variation can be explained by the input variables. Generally, a value greater than 0.6 is considered meaningful, although a high R value does not necessarily imply that the model chosen is appropriate. The p value is a measure of the probability that there is no relationship between the variables, given the results obtained. A general mark of $p < 0.05$ is used for statistical significance, i.e., less than a 5% chance of getting the result given no correlation between variables.

4.4 Results

4.4.1 Left ventricular residence time distributions

Smoothed RTD graphs accumulated over five heartbeats for a patient with a normal heart and a heart with a reduced LVEF are shown in Figure 4.1 & Figure 4.2 respectively. All healthy patients demonstrated a prominent peak at the first heartbeat. Patients with ventricular dysfunction had the highest peak at the second heartbeat and a greater spread across the heartbeats, although a small number (~ 3) of 16 sick patients had the highest peak at the third heartbeat.

Residence Time Distribution of particles in the left ventricle
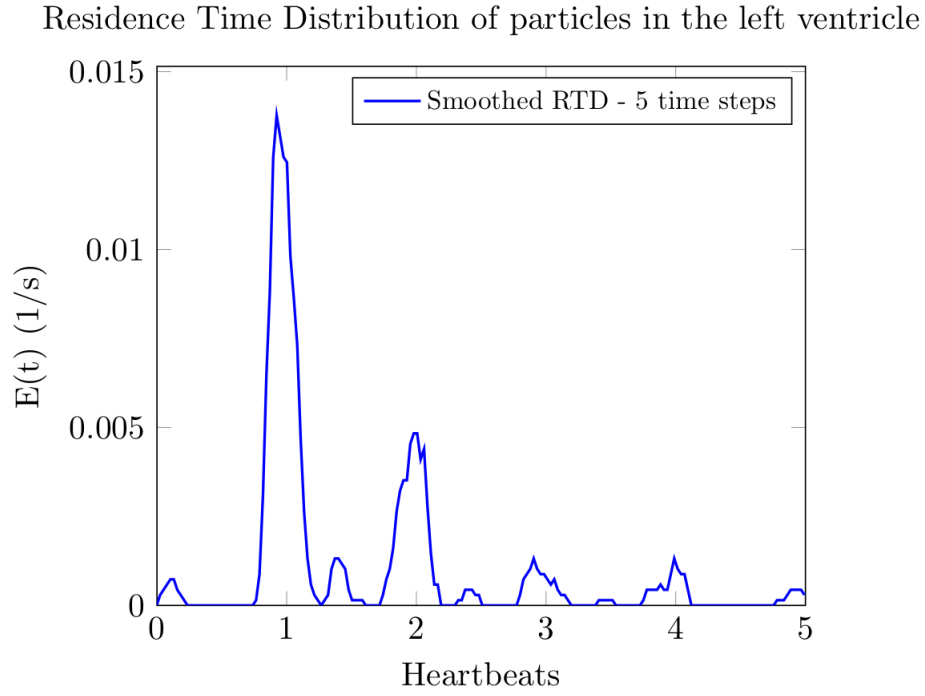
Figure 4.1: Example of smoothed left ventricular residence time distribution from a healthy patient with LVEF = 60%.

Residence Time Distribution of particles in the left ventricle
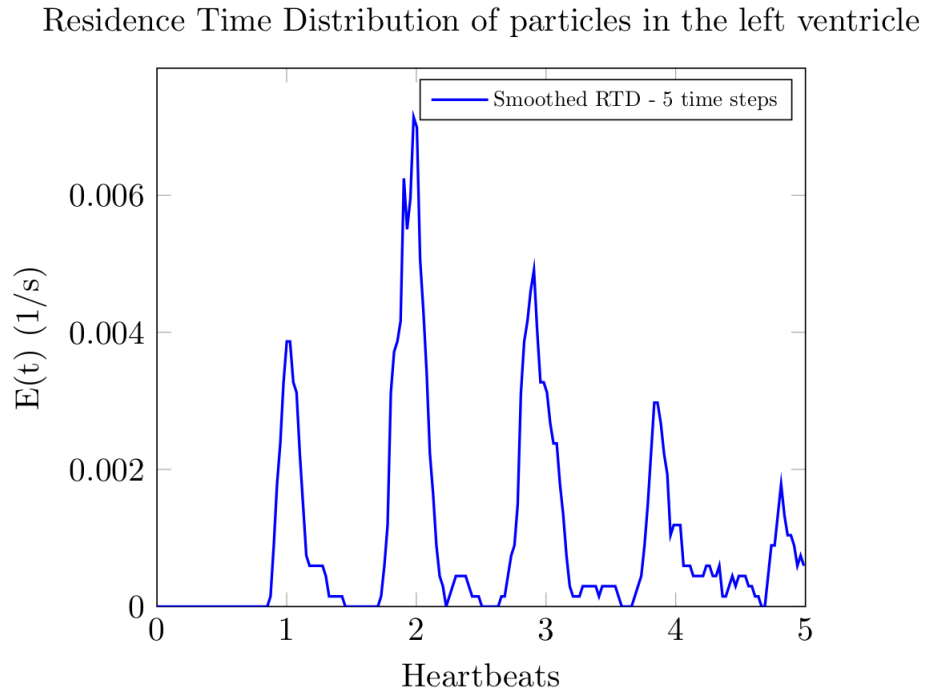
Figure 4.2: Example of smoothed left ventricular residence time distribution from a patient with dilated cardiomyopathy & LVEF=38%.

Exponential decay curves are shown in Figures 4.3 and 4.4. These decay curves are fit to the fraction of particles remaining in the left ventricle for each patient. Patients with regular LVEF demonstrate an approximate 50% drop in fraction of particles remaining after the first heartbeat, as seen in Figure 4.3, whereas patients with a lower LVEF have a more gradual drop in fraction of particles as seen in Figure 4.4. This demonstrates how hearts with low LVEF are incapable of expelling blood as efficiently. Comparing the results obtained here to the previous RTD study carried out on artificial left ventricles (Shettigar *et al.*, 1989), a broad agreement between the results was seen. Shettigar *et al.* (1989) reported 42% of blood particles being expelled at the end of the first ventricular contraction, 36% being expelled in the second heartbeat, 17% being expelled in the third heartbeat, and the remaining 5% in the following heartbeats. The values obtained in Figure 4.3 are marginally higher. This may be due to the realistic nature of the left ventricle pumping action being captured by the decay curves as this analysis was carried out on actual left ventricles, whereas Shettigar *et al.* (1989) was carried out on artificial left ventricles.

Plot of the exponential decay of number of particles v.s. heartbeats

$RTD : 1.276e^{-0.8205x}$
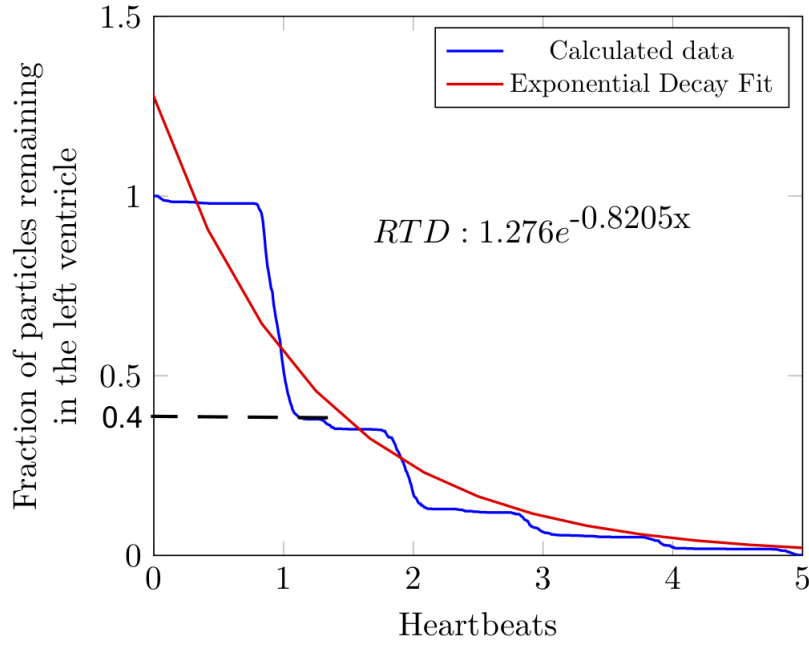
Figure 4.3: Example exponential decay curve from a healthy patient with LVEF = 60%. Curve is fitted to the complete calculated data set.

Plot of the exponential decay of number of particles v.s. heartbeats

$RTD : 1.249e^{-0.37857x}$
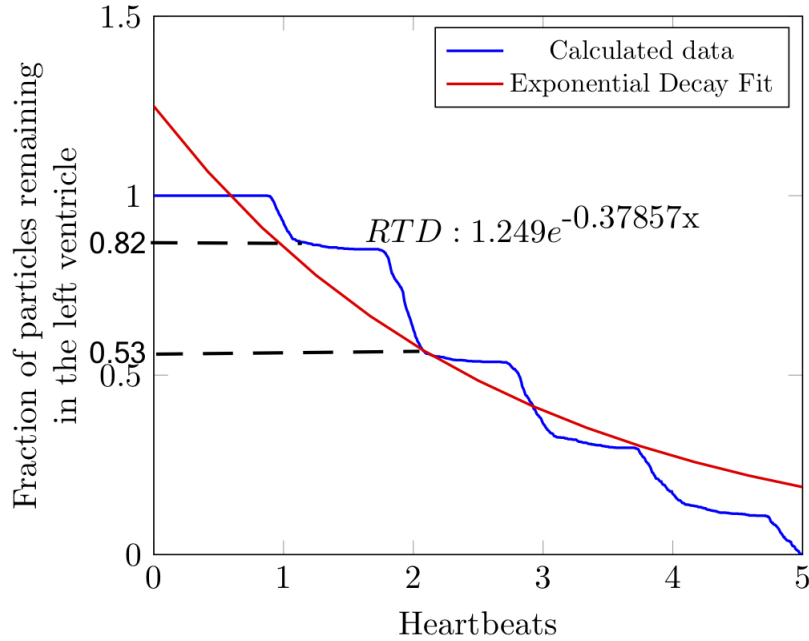
Figure 4.4: Example exponential decay curve from a patient with ventricular dysfunction & LVEF=38%. Curve is fitted to the complete calculated data set.

The ability of the RTD constant (LV RTD_c) to characterise heart health in the left ventricle was assessed by comparing it with the left ventricular ejection fraction. There was a significant difference in the LV RTD_c of healthy volunteers and those with dysfunctional hearts as determined by LVEF (LV RTD_c 1.2±0.13 vs 2.2±0.80, $p < 0.001$ for both groups) as seen in Figure 4.5. The box plot shows that the LV RTD_c for the reduced LVEF group has a wider range than that for the normal group. This may be an effect of the varying extent of illness and cardiac dysfunction faced by the patients within the reduced LVEF group. From a purely discriminatory viewpoint, our results show that the concept of the RTD can be used to distinguish between sick and healthy patients.
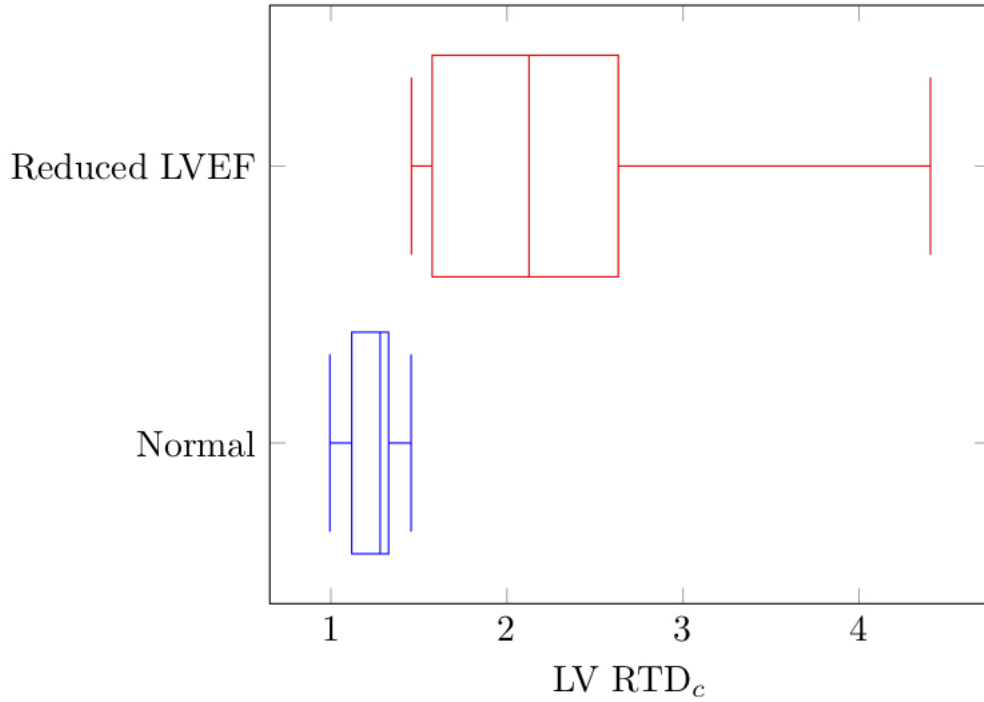
Figure 4.5: Box plot of left ventricular residence time distribution constant amongst group. The left and right bars indicate the minimum and maximum values respectively. The three bars in the middle signify the first quartile, the median and the third quartile, respectively.

There was a strong negative correlation between the LV RTD_c and LVEF ($R = -0.843, p < 0.001$) as seen in Figure 4.6. Values for the normal group were clustered closer together in a tight pattern, compared to those for unhealthy hearts which were broadly spread with little order. The strong correlation and low p value suggests that the LV RTD_c and LVEF are closely related, and that the elevated LV RTD_c may be a sensitive measure of cardiac dysfunction.
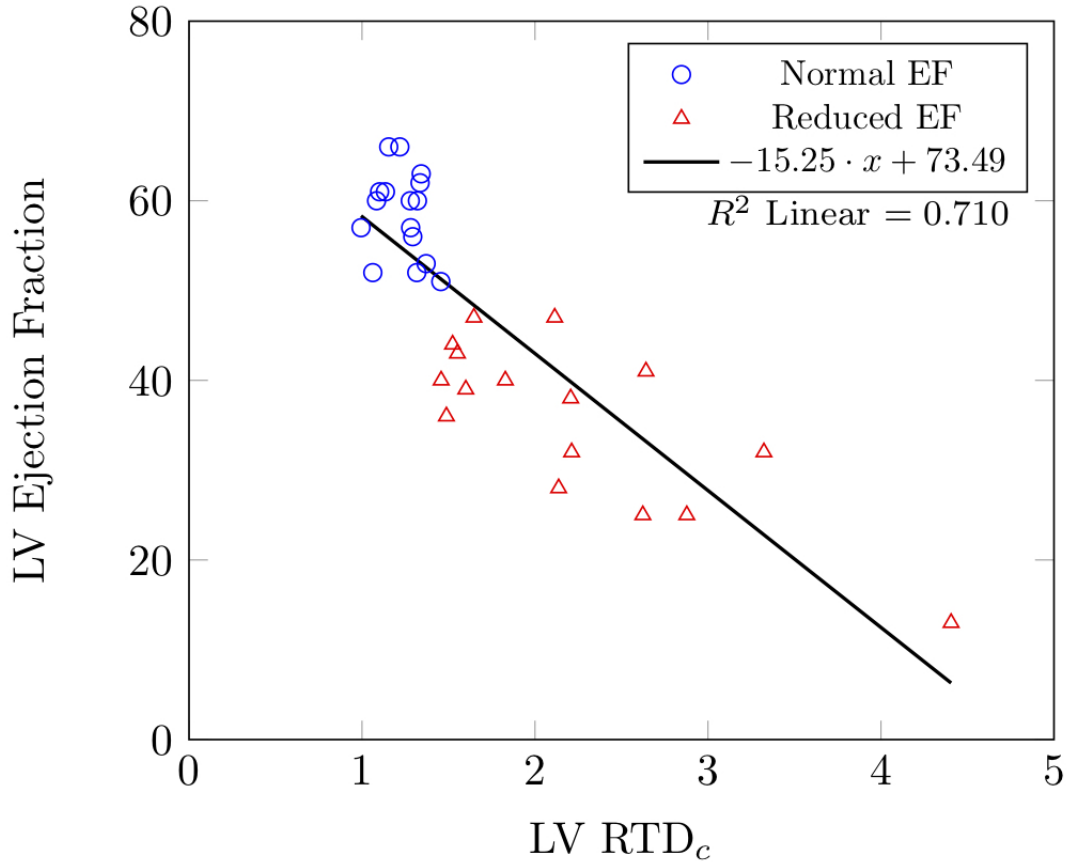
Figure 4.6: Correlation of LV ejection fraction (y-axis) with residence time distribution constant (LV RTD_c, x-axis). The healthy controls are displayed as blue circles, patients with dilated cardiomyopathy as red triangles.

Furthermore, when the RTD_c was compared to the GLS (measuring the elasticity of the heart muscle measured by a % change in length), a strong positive correlation was obtained ($R = 0.7805, p < 0.001$) as seen in Figure 4.7. Values for the normal group were seen to be grouped together with a smaller range of GLS and RTD_c, whereas the group with dysfunctional hearts were spread out with a wider range of RTD_c. Some patients with dilated cardiomyopathy recover a normal EF in the future, with or without medical intervention. Recovered patients with a normal EF however remain at a higher risk of future cardiovascular events, and 40% of them undergo a relapse of left ventricular dysfunction (Cheng *et al.*, 2014; Basuray *et al.*, 2014). This may explain why patients who appear "clinically stable" remain susceptible to haemodynamic stress and undergo subsequent heart failure events. The results obtained here suggest that there is a close relationship between the myocardial strain and cardiac flow.
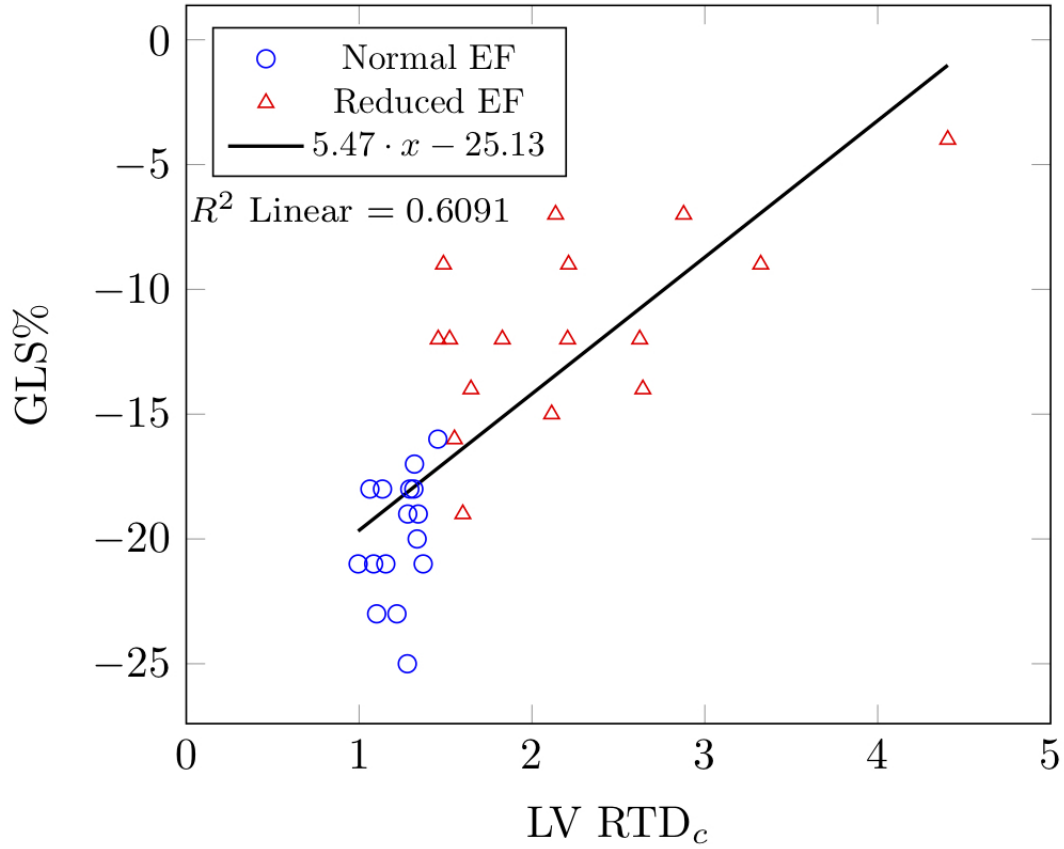
Figure 4.7: Correlation of global longitudinal strain (GLS) (y-axis) with residence time distribution constant (LV RTD$_c$, x-axis). The healthy controls are displayed as blue circles, patients with dilated cardiomyopathy as red triangles.

A study carried out by Adamo *et al.* (2017) showed that amongst a patient group with a currently normal LVEF, those with impaired GLS (i.e. $< -16\%$) have 3 times the risk of undergoing a drop in LVEF after a subsequent check-up (61.8% vs 21.4%). Furthermore, every percentage increase in GLS value increased the likelihood of maintaining a normal range LVEF during followup by 22%. This demonstrates the importance of using GLS as a diagnostic and prognostic tool, particularly in cases where the ejection fraction does not describe the full extent of cardiac dysfunction. Furthermore, it seems prudent to include some of the patients in the current study for a future study to investigate how the GLS and LVEF values change between check-ups, and how this relates to a change in LV RTD$_c$.

Another indication of cardiac dysfunction can be obtained from T1 values. Elevated T1 values (i.e. > 1200 ms) can be a sign of *odema* (increase of water in tissue because of inflammation) or increased *interstitial space* (from scarring or cardiomyopathy). Here, we found a weak positive correlation when the RTD_c was compared to the T1 native values ($R = 0.1517, p = 0.4073$). Recall, T1 native value is related to the thickening of the heart muscle tissue. Noticeably, the values for the normal group are more spread out and with less order than the EF and GLS comparisons. Interestingly, a number of subjects from the sick patient group had similar native T1 values as their healthy counterparts. This suggests the lack of a strong relationship between scarring and impairment of cardiac flow.
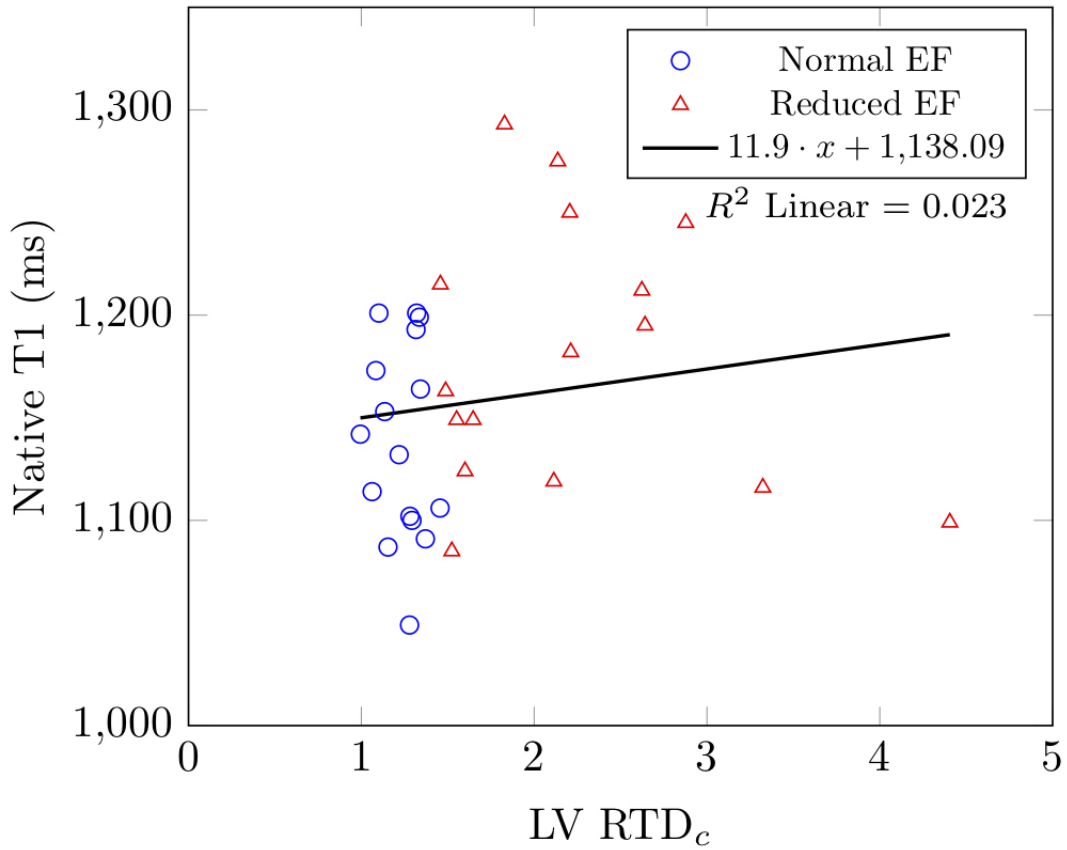
Figure 4.8: Correlation of T1 native values (y-axis) with residence time distribution constant (LV RTD_c, x-axis). The healthy controls are displayed as blue circles, patients with dilated cardiomyopathy as red triangles.

4.4.2 Further assessment of left ventricular residence time distributions

To understand the concept of the RTD further, three patient cases were selected, and their RTD graphs compared. These were Patient RC (with an left ventricular ejection fraction of 25%) presented in Figure 4.9, Patient SB (with a left ventricular ejection fraction of 25%) presented in Figure 4.10, and Patient PS (with a left ventricular ejection fraction of 13%) presented in Figure 4.11.
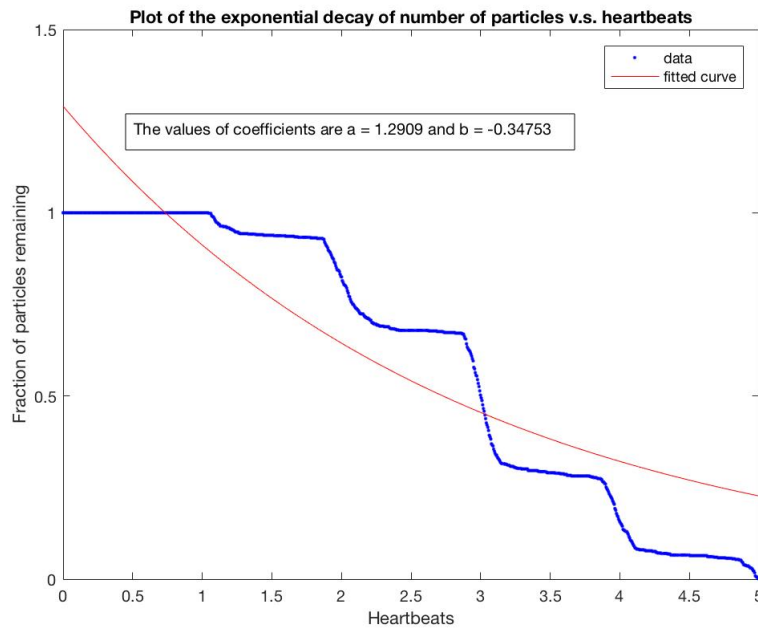
Figure 4.9: Example exponential decay curve of Patient RC with a left ventricular ejection fraction of 25%.

From the results obtained in Figures 4.9 and 4.10, it is clear that similar ejection fractions do not result in similar RTD graphs being obtained. Patient RC (RTD value: 2.98) demonstrates an expelling of a negligible fraction of particles in the first heartbeat followed by a 20% drop in the second heartbeat followed by a 40% drop in the third heartbeat. Conversely, Patient SB (RTD value: 2.67) demonstrates a gradual and consistent expelling of 20% of particles each heartbeat. When Patient PS (RTD value: 4.42) was considered, no expelling of particles occurred in the first two heartbeats, followed by a small loss of 10% in the third heartbeat, and a large 30% loss in the following two heartbeats. These results suggest that further analysis
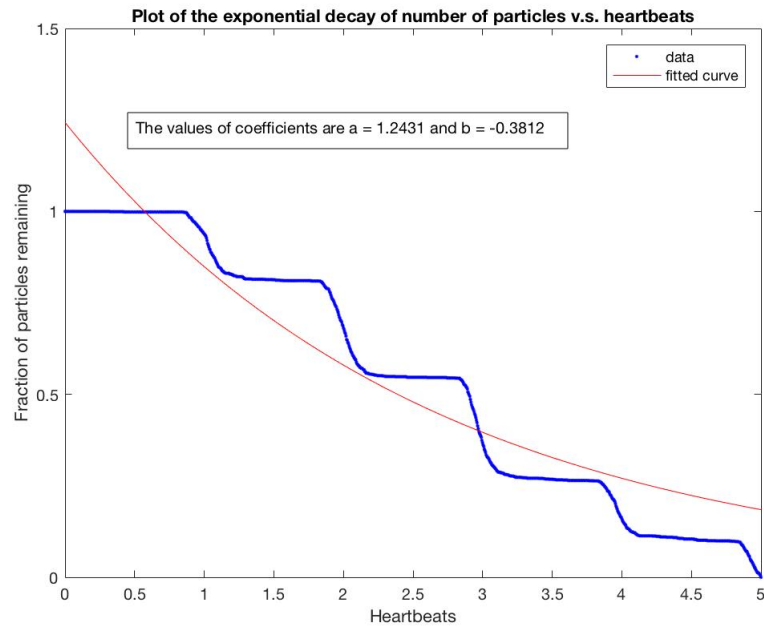
Figure 4.10: Example exponential decay curve of Patient SB with a left ventricular ejection fraction of 25%.
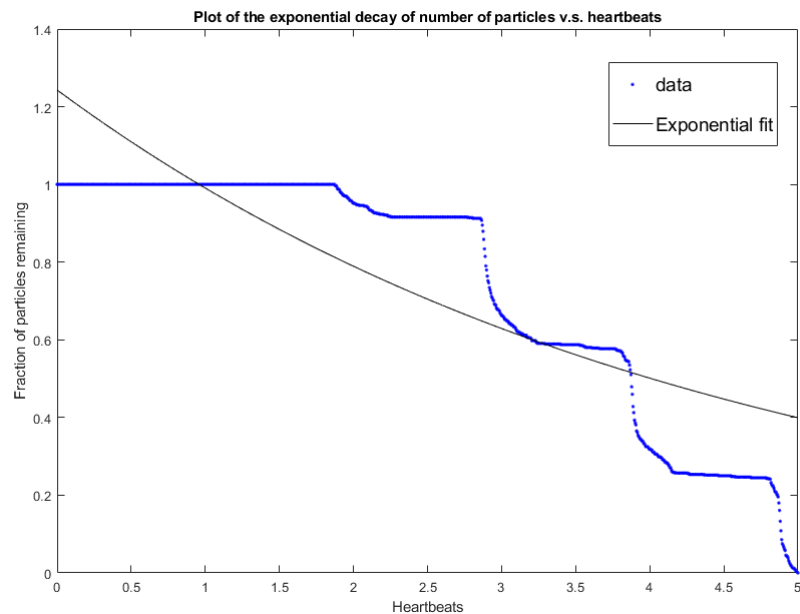
Figure 4.11: Example exponential decay curve of Patient PS with a left ventricular ejection fraction of 13%.

of these patients is required, and that their cardiac dysfunction differs amongst them even though they may display similar ejection fractions. Whilst the exact nature and extent of their dysfunction is not available, a closer analysis of Patient RC reveals that their end-diastolic volume was more than double that for Patient SB

(537 vs 218 mL). This indicates that Patient RC had a greater volume of blood in the left ventricle prior to the systole (contraction). This may be due to an enlarged chamber (i.e. dilation of the left ventricle) and may indicate that Patient RC suffers from dilated cardiomyopathy to a greater degree than Patient SB. The end-diastolic volume for Patient PS was elevated (374mL). End-diastolic volumes vary based on the health, age and gender of the patient. A normal value would lay in the range of 150–200 mL.

Upon closer examination of the RTD graphs, Patient PS and RC had 2533 particles seeded by the Siemens software and only 750 (30% of the seeded particles) actually transit the left ventricle, whereas Patient SB had double the particles transit (1500 for a total of 60% of the seeded particles transiting). This is a stark anomaly when the general case for the rest of the patients was 85-90% of seeded particles transiting the left ventricle. The small percentage of particles transiting is consistent with significant "hold-up" of fluid and is likely due to slow mixing regions. The number of particles actually transiting compared to the number seeded is an important marker as it can reveal information on the amount of blood that fails to transit, the condition of the patient, and may reflect the possibility of a larger risk of thrombus formation.

The entry and end points of the particles seeded for Patient PS are displayed in Figure 4.12. Charting the trajectory of the particles allows us to determine whether blood pools, and if so, where in the chamber. From Figure 4.12, it is clear that a number of particles collect and never escape in at least two distinct regions of the chamber. This explains why the number of particles transiting the chamber was low. It also represents the elevated risk of Patient PS suffering from thrombus formation (stroke). There are a number of particles that were "missing" the exit plane, but seen to exit the left ventricle. This was attributed to noise, as it was physically impossible for particles to exit the left ventricle but not cross the exit plane.
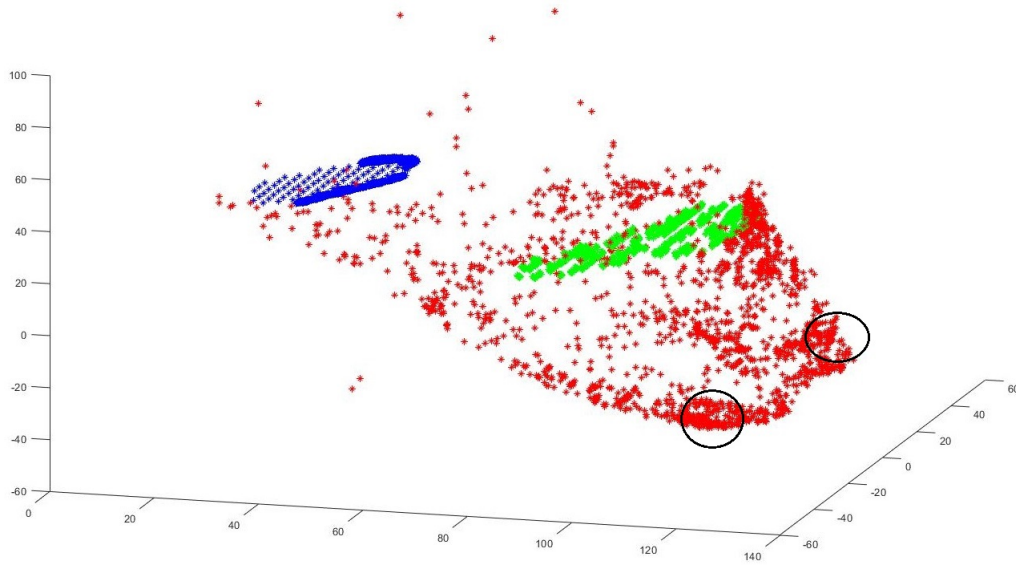
Figure 4.12: Entry Points (Green) and Exit/End Points (Red) of particles for Patient PS. Blue plane is the exit plane. Black circles denote area where blood collects

Residence time distributions were developed for a further eight patients from the reduced LVEF group, and shown in Figures 4.13 and 4.14. The results demonstrate how residence time distributions can vary significantly despite a small change in ejection fraction amongst patients with reduced function. A few observations were made from the results. Firstly, there were circumstances whereby a higher ejection fraction did not correspond to a larger fraction of particles being expelled within the first heartbeat (see Figure 4.14b and Figure 4.14c). Patient MB (LVEF = 41%) demonstrated a more gradual drop in fraction of particles compared to Patient RB (LVEF = 32%). Within the first two heartbeats, less than 50% of the seeded particles transited the left ventricle for Patient MB, whereas about 55% of particles were expelled within the same time period for Patient RB. The difference between the two patients becomes clearer when we consider the time period of the first heartbeat. This conveys the notion that although Patient MB may be considered "healthier" if ejection fraction was the sole indicator of health, blood flow through the LV was restricted in a greater manner than for Patient RB. This warrants other medical tests carried out to ascertain the full nature of the disease for Patient MB. Secondly, some patients did not exhibit sharp drops of particle fraction at the

time of ventricular contraction (particularly after the third heartbeat). This was seen most significantly in Patient AM (see Figure 4.13b), and to a lesser extent in Patient JL (see Figure 4.14a) and Patient RF (see Figure 4.14d). For Patient AM, there was a gradual drop in particles from 25% remaining at the second heartbeat for the remaining three heartbeats. This may signify the presence of some cardiac pathology that allows blood to leave the left ventricle throughout the cardiac cycle, or possibly a faulty aortic valve (that should be closed except during ventricular contraction). Regardless, this suggests that the RTD has the ability to provide more information than the ejection fraction by looking at a blood flow over a time period (5 heartbeats).
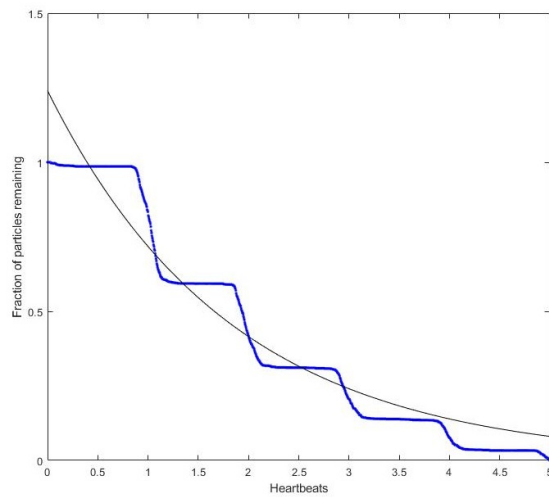
(a) Patient AF with LVEF = 40%.
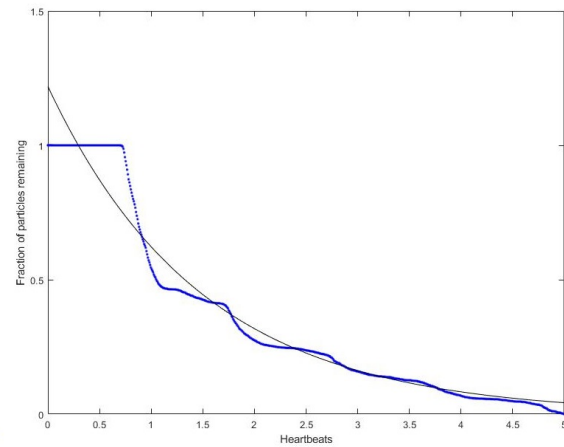
(b) Patient AM with LVEF = 36%.
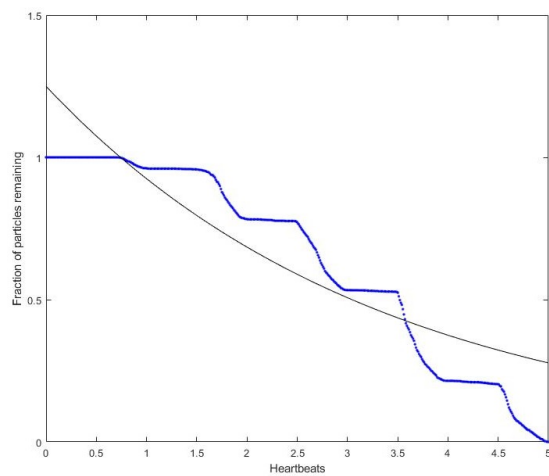
(c) Patient BR with LVEF = 32%.
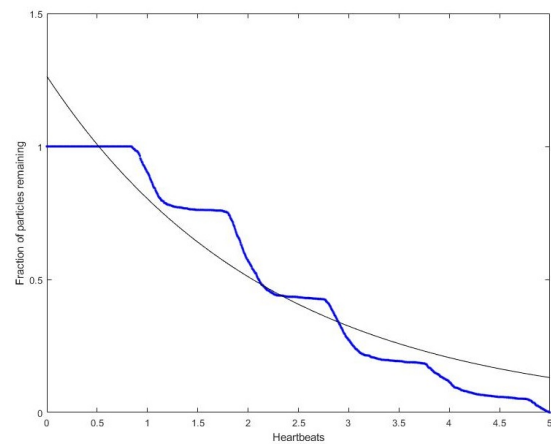
(d) Patient JC with LVEF = 38%.

Figure 4.13: Fraction of particles remaining in the left ventricle over time for four patients (LVEF $<$ 50%). Blue line denotes the particle fraction, black line denotes the exponential decay fit.
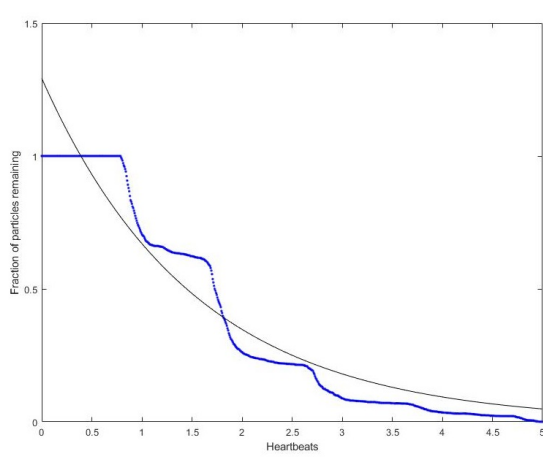
(a) Patient JL with LVEF = 44%.
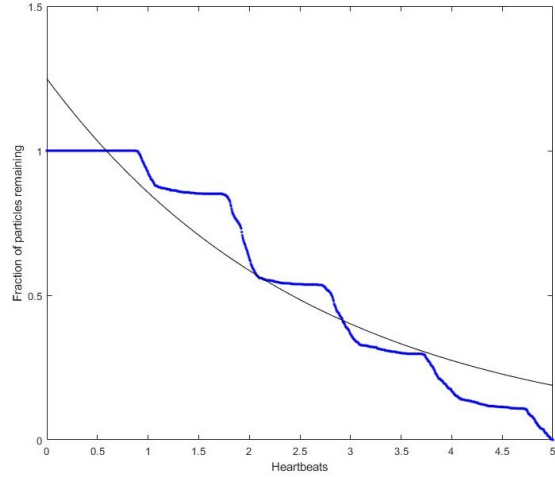
(b) Patient MB with LVEF = 41%.
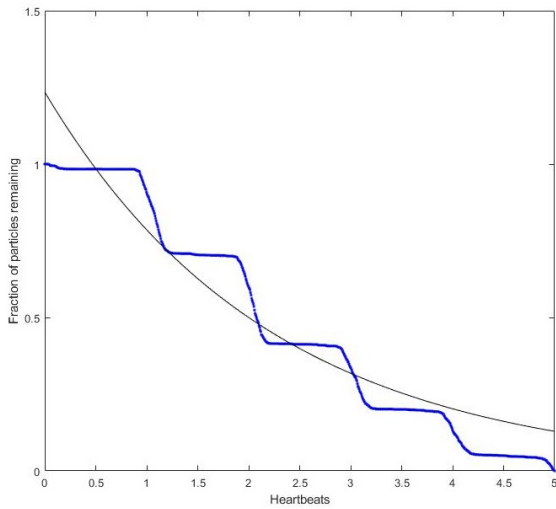
(c) Patient RB with LVEF = 32%.
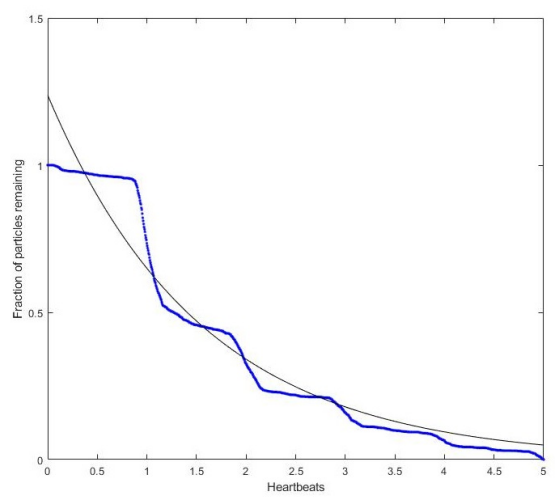
(d) Patient RF with LVEF = 43%.

Figure 4.14: Fraction of particles remaining in the left ventricle over time for four patients (LVEF < 50%). Blue line denotes the particle fraction, black line denotes the exponential decay fit.

4.4.3 Right ventricular residence time distributions

The RTD_c was seen to correlate well with dysfunction in the LV. It seems possible that the concept may carry over to other heart chambers. To explore this further, residence time distributions were produced from particle tracking in the right ventricle. The box plot showing the differences in RV RTD_c between the two groups is presented in Figure 4.15. The correlation of the RV RTD_c to the RV ejection fraction is shown in Figure 4.16.
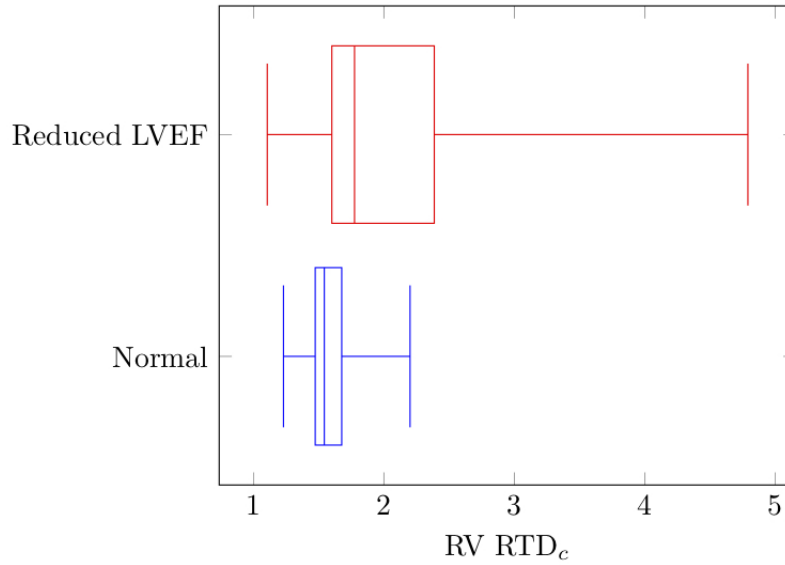
Figure 4.15: Box plot of right ventricular residence time distribution constant for the two groups.

For this study, the mean RTD_c was compared between the focus groups that were defined by the patient left ventricular ejection fraction. In the healthy focus group, the RV RTD_c was 1.5 ± 0.2 compared to 1.8 ± 0.57, $p = 0.01$ in the dysfunctional heart focus group (see Figure 4.15). When the box plots are compared (Figures 4.15 and 4.5), it is seen that there is more overlap between the patient groups for the RV. A greater number of patients in the reduced LVEF have a RV RTD_c which falls within the range of RV RTD_c for the healthy patients.

The RV RTD_c & RVEF are modestly negatively correlated ($R = -0.7113$, $p < 0.001$) as seen in Figure 4.16. Overlap between the normal and reduced LVEF group was seen again. The normal LVEF group are more spread out when compared
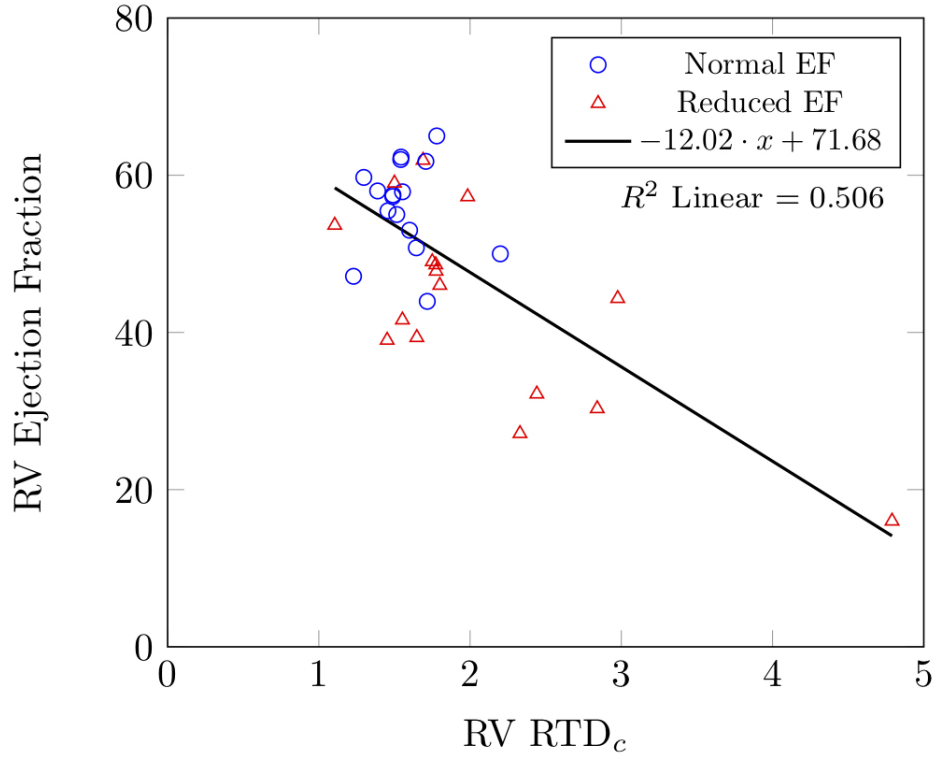
Figure 4.16: Correlation of RV ejection fraction (y-axis) with residence time distribution constant (RV RTD$_c$, x-axis). The healthy controls are displayed as blue circles, patients with dilated cardiomyopathy as red triangles.

to Figure 4.6 where the patients LV RTD$_c$ were close together. Moreover, some patients from the reduced LVEF group demonstrate RV RTD$_c$ values that could be mistaken for the normal EF group. The correlation in the right ventricle was not as strong as that in the left ventricle (see Figure 4.6). This may have been due to the challenge of accurately defining the tricuspid plane (seeding plane for the RV) as noted by the cardiologist. Particles not seeded at the position of the tricuspid valve may be seeded in the right atrium and thereby take longer to transit the chamber. It is possible that a different relationship exists between RTD$_c$ and the ejection fraction of the left and right ventricle. Dilated cardiomyopathy is not always biventricular, and the RTD$_c$ of the right ventricle may provide an insight into the extent of involvement of the right ventricle in the disease. In a case where the RV RTD$_c$ falls within the healthy range (0.5 to 1.7) and the LV RTD$_c$ is greater than 1.7, a greater prevalence of the disease in the left ventricle rather than the right

may be true. In the opposite case (i.e. where the LV RTD_c falls in the healthy range whereas the RV RTD_c is elevated), a greater prevalence of the disease afflicting the right ventricle compared to the left may be the likely cause.

4.4.4 Right atrial residence time distributions

Following on from the previous section, residence time distributions were produced from particle tracking in the right atrium. In the right atrium, the atrial RTD_c was compared between the groups defined by the left ventricular ejection fraction. A weak negative correlation was observed ($R = -0.4543$, $p = 0.009$) as shown in Figure 4.17. The healthy patient group had a number of distinct clusters of data points, and other data points more spread out. The group with reduced EF demonstrated a wider spread of atrial RTD_c (ranging from $1.2 - 4.1$), with approximately half of the patient group having an atrial RTD_c less than 2, and within a similar range to the normal EF group. The correlation in the right atrium is lower than that of the right ventricle or left ventricle. A contributor to the lack of correlation may be due to the noted difficulty of defining the tricuspid plane (exit plane for the RA). It may also be due to a lack of relationship between the ejection fraction of the left ventricle and blood flow through the right atrium, or that an alternative relationship exists.

4.5 Discussion

In this chapter, the residence time distribution has been described and determined for 2 sets of patients, one with normal cardiac function and the other with dilated cardiomyopathy. The RTD, produced from time-dependent MRI derived velocity fields, is demonstrated to be a novel method of assessing cardiac function and efficiency. The RTD_c was found to be lower in participants with a normal functioning LV (defined by LVEF) compared to the dysfunctional LVEF group. Healthy volunteers with presumed normal cardiac function displayed a RTD constant that fell within a narrow range (mean 1.24, range 1.0–1.45). Participants from the dysfunc-
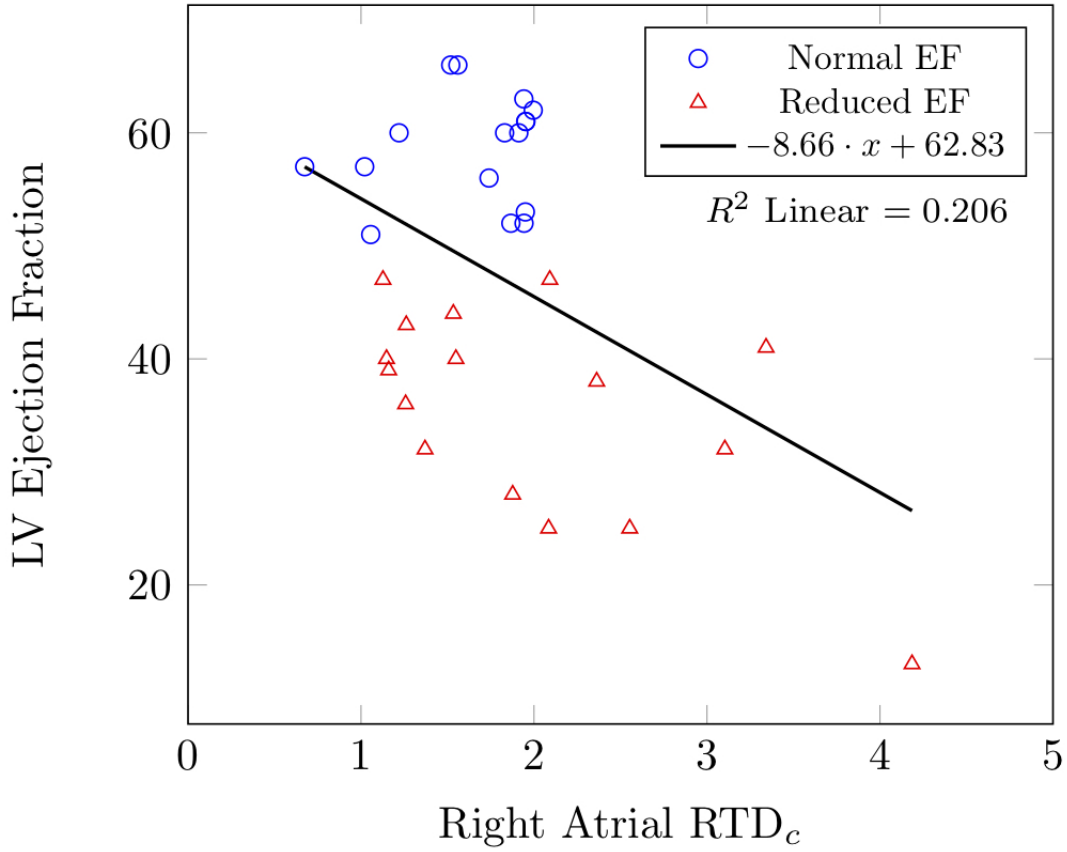
Figure 4.17: Correlation of LV ejection fraction (y-axis) with residence time distribution constant (right atrial RTD$_c$, x-axis). The healthy controls are displayed as blue circles, patients with dilated cardiomyopathy as red triangles.

tional LV group had an RTD$_c$ higher than this and with a broader range (from 1.45 to 4.48).

For healthy volunteers, the largest percentage of blood was expelled in the first cardiac cycle. Comparatively, the dysfunctional LV group demonstrated a greater volume exiting during the latter cycles, indicating a delay in transit of blood as seen in the difference of mean ejection fraction values from Table 4.1. This delay in transit is a marker of inefficiency, as it indicates that the chamber transports blood at a reduced flow rate. Furthermore, it indicates that there is a possibility that blood pools and collects, before it transits the chamber in following heartbeats as seen in Figure 4.12.

Whilst ejection fraction is an effective method of analysing the left ventricular performance, providing prognostic and functional information (Curtis *et al.*, 2003), low LVEF is often a late sign of dysfunction, and finding markers of dysfunction earlier in the pathophysiologic process could improve clinical outcomes. Given that we have demonstrated that the RTD_c does distinguish clearly between healthy and sick patients in the LV, usage of the RTD can be incorporated in the post-MRI scan phase of the diagnostic process. The patient's particle tracking data would be processed, RTD_c obtained and their risk for cardiac dysfunction defined before they return to their cardiologist for their post-MRI check-up. The RTD_c provides a theoretical advantage over ejection fraction in cardiomyopathy. This is because ejection fraction is influenced by functional mitral regurgitation (reversal of blood flow from the left ventricle to the left atrium). The reversal of blood flow causes the stroke volume to reduce thereby reducing the ejection fraction. This is a common occurrence amongst patients with more advanced cardiomyopathy, which may lead to the misestimation of cardiac function based solely on ejection fraction (Trichon *et al.*, 2003; Donal *et al.*, 2009). The RTD is able to identify particles that cross the entry plane multiple times (in the case of mitral regurgitation) and exclude them from the analysis.

Ventricular function has been characterised beyond ejection fraction by a number of studies investigating myocardial tissue. Analysis of myocardial deformation (GLS), tissue Doppler velocities and T1 mapping are alternative techniques looking at myocardial factors to determine pathology, and have had the ability to identify and classify cardiovascular disease (Iles *et al.*, 2008; Stanton *et al.*, 2009; Biering-Sorensen *et al.*, 2015). The strong correlation between the RTD_c and the GLS suggests that there is close relationship between the deformation of the myocardium, efficiency of blood flow through the heart and the ejection fraction.

Bolger *et al.* (2007) used time-resolved MRI derived velocity fields to develop a method of compartmentalising LV blood flow into four components based on compartmental origin and fate. Direct flow enters and leaves the LV in a single cardiac

cycle; delayed ejection flow refers to blood that originates in the LV and exits during the systolic phase; retained inflow enters the LV in the diastolic phase but does not leave in the next systole; and the residual volume remains in the LV for at least two complete cardiac cycles. This approach can theoretically be used to distinguish cardiomyopathy from normal LV function if a greater proportion of 'residual volume' is seen. However, it is computationally intensive and not routinely available with existing post-processing software. The RTD is a similar concept to the 4 component model as it largely reflects the direct flow component. It has the advantage of being a process that can be incorporated into CMR analysis in a time effective manner and applied to all cardiac chambers. According to our results, up to 60% of blood particles transited the LV in the first cycle in normal functioning hearts (analogous to direct flow). Residence time distribution analysis has been used to evaluate dead space in chemical reactors. In a similar fashion, the 'retained flow' component in the cardiac cycle and the ventricular residence time distribution can provide an insight into the conditions under which particles enter the chambers during the relaxation phase but do not exit during the first contraction.

From the results, it appears that maintaining an efficient flow of blood as it passes through the atrioventricular valve and into the aorta is a key indicator of cardiac performance. Further analysis of how this translates to avoiding stasis is warranted. Studying whether the RTD, when deployed in a clinical setting, can detect early stages of left and right ventricular cardiac pathologies is required to determine the value of the RTD_c as an independent measure of cardiac function.

From a diagnostic perspective, it appears that the RTD is useful in a discriminatory capacity. The narrow range of LV RTD_c in healthy patients may increase diagnostic sensitivity through an investigation into whether RTD_c values obtained outside of a narrow range correlate with cardiac dysfunction. Moreover, the hypothesis that the RTD can provide incremental value in diagnosis and in monitoring response to interventions over strain analysis and T1 mapping requires further investigation. This should be carried out in a clinical setting by charting treatment

options based primarily on the RTD_c.

A number of assumptions have been made in developing the RTD_c. Blood flow in the heart was assumed to achieve steady state. Blood flow and velocity was phase averaged over the duration of the scan. In the case where an isolated event occurs that affects blood flow within the heart over a short time frame (e.g. palpitations), the effects of this are averaged over the entire cardiac cycle and made less 'visible'. Furthermore, because the group with reduced EF contains both current and recovered cases, it is possible that pharmacologic treatment may have changed the flow dynamics of individual patients within the group and confound our results. The RTD uses particle tracing as a quantitative technique, and although the accuracy of the data could not be directly tested, the relevance of the association between LV ejection fraction and RTD_c appears strong.

4.6   Summary

4D flow cardiac magnetic resonance (CMR) imaging allows visualisation of blood flow and acquisition of blood velocity fields in the heart chambers and large vessels. Post processing of the flow data allows determination of the residence time distribution (RTD), a novel means of assessing ventricular function, potentially providing additional information beyond ejection fraction. Left and right ventricular (LV and RV) blood flow efficiency was evaluated using RTD measurements. 16 healthy patients and 16 patients with cardiac dysfunction (as defined by LVEF $< 50\%$) were studied using cardiac magnetic resonance imaging including 4D flow. The RTDs were developed computationally by seeding virtual 'particles' at the inlet plane in customised post-processing software, moving these particles with the measured blood velocity, recording and counting the number of particles that exited the chamber per unit of time. Ventricular flow efficiency was determined from the RTDs based on the time constant ($RTD_c = \frac{1}{b}$) of the exponential decay fit to the particle fraction. The RTD_c was compared to the ejection fraction. There was a significant difference between groups in LV RTD_c (healthy volunteers 1.2 ± 0.13 versus systolic dysfunc-

tion 2.2 ± 0.80, $p < 0.001$) and RV RTD_c (1.5 ± 0.15 versus 1.8 ± 0.57, $p = 0.013$). The LV RTD_c correlated significantly with LVEF ($R = -0.843$, $p < 0.001$) and the RV RTD_c had significant correlation with RVEF ($R = -0.7113$, $p < 0.001$). This reduced correlation might be explained by the difficulty in defining the particle seeding plane for the RV. Furthermore, there was strong correlation between the LV RTD_c and the GLS parameter ($R = 0.7805$) and a weak correlation to the T1 value ($R = 0.1517$). The ventricular residence time correlates with ejection fraction and can distinguish normal from dysfunctional ventricular function, and can serve as a biosensitive marker for myocardial dysfunction. Further assessment of this method of assessment of chamber function and its applicability in other chambers is warranted. The deployment of the RTD in a clinical setting as a tool for early diagnosis of cardiac dysfunction is justified. Clearly, it will be of interest to follow the future fate of patients within this study.

Chapter 5

Computational Fluid Dynamics

5.1   Introduction

The left ventricle (LV) and the mitral and aortic valves play a pivotal role in the pumping of blood through the body, and the overall health of an individual. Patients with abnormal cardiac function display altered flow dynamics. It is hypothesized that obtaining derived markers of cardiac function from cardiac magnetic resonance imaging data may provide clinicians an additional useful tool that could be used for diagnosis and prognosis. A patient-specific 3D model of the LV is developed by post-processing two-dimensional MRI images. At this stage of development of the approach, the connections of the left ventricle to the aorta and atrium through the aortic and mitral valves have been simplified. This modified approach was taken because of continuing computational difficulties in producing a consistent model involving the three moving subdomains (ventricle + aorta + atrium) within the FLUENT ALE framework. Indeed, this was not helped by limitations within FLUENT of interacting through UDFs and restrictions of mesh movement within the program itself. So at this stage, *tubes* have been added to the top of the LV to (weakly) represent the inlet (mitral valve) and outlet (aorta). A more realistic model is still under development at the time of writing this thesis.

Computational flow fields obtained from the simulation can provide an insight into the nature of mixing, stasis and the efficiency of blood flow, factors which

affect cardiovascular function. Computationally obtained flow fields also provide an advantage over time-resolved phase-averaged flow fields obtained from cardiac MRI as they have the ability to provide greater temporal and spatial resolution. This further signifies the prospect of computational fluid dynamics as an additional tool that clinicians may rely on to provide clinically relevant data.

In this chapter, an initial computational fluid dynamics model (CFD) of the left ventricle is developed and described. The effect of the pumping action of the left ventricular wall on blood flow is highlighted.

5.2 Methodology

To obtain the fluid domain, the 25 frames of the endocardial LV walls were obtained for one blood-pumping cycle from the MRI (refer to Section 3.4). The motion of the LV wall was derived from positional data obtained during the segmentation of the LV endocardial borders, as described in Sections 3.2 and 3.4.

A grid dependency study was carried out for 5 different grids, whereby the number of grid elements were increased by a factor of 1.5 (8000, 12000, 18000, 27000 and 40500). Calculated flow velocities did not change as the number of cells were increased from 27000 to 40500. In the range from 18000 to 27000, the changes in flow features were minor. For more accurate results, 27000 cell numbers were chosen for the 3D modelling. An unstructured grid using tetrahedral elements was generated as seen in Figure 5.1. Outflow boundary conditions were applied to the face of the outlet tract.

The geometry used for the CFD simulation is shown in Figure 5.1. The wall of the LV was assigned to expand and contract as prescribed by the UDF created. The diameters of the mitral valve inlet and aorta outlet were approximated to be ≈ 3 times smaller than the actual diameters to ensure the dynamic mesh routine ran. The mitral valve inlet and aorta outlet were prescribed to remain stationary i.e. not move or expand/contract. The top and bottom were assigned to deform based on the subsequent movement of the wall. The dynamic mesh methods used

in FLUENT included *Smoothing* and *Remeshing*. *Remeshing* occurs when the face skewness exceeded 0.9. A spring-based *smoothing* method was used with a spring constant factor of 0.05 and a convergence tolerance of 0.001. This method changes cell edge sizes from timestep to timestep as these lengths move away from their initial lengths during the mesh movement.
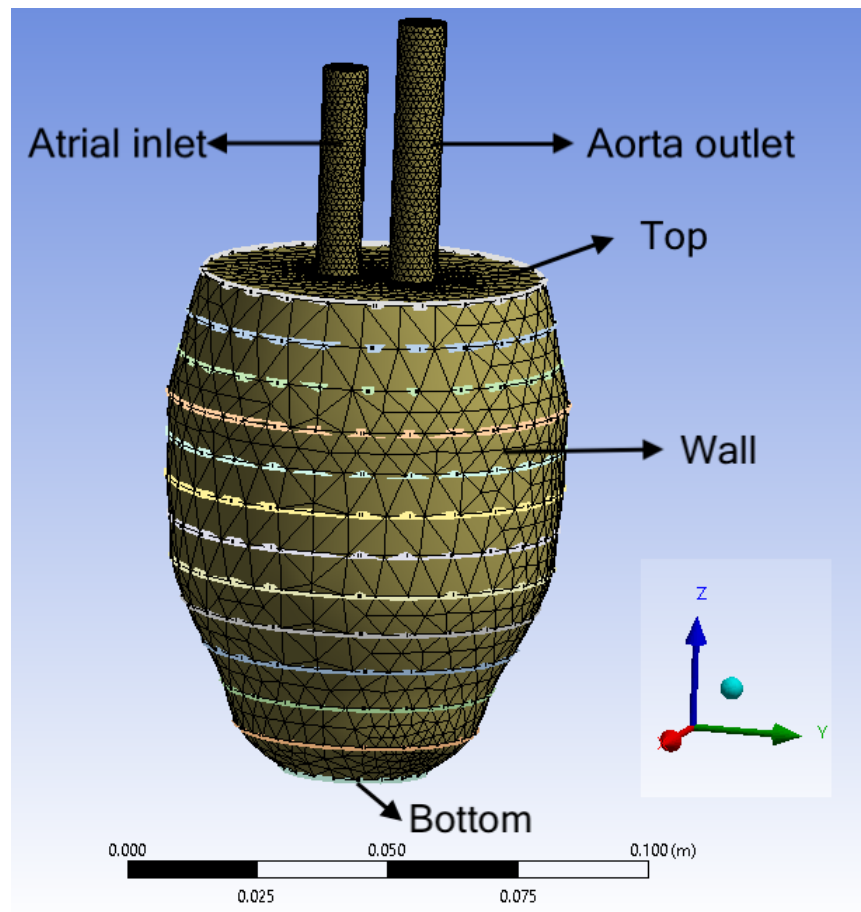
Figure 5.1: Patient-specific LV reconstructed with idealised atrial inlet and aorta outlet. Unstructured mesh generated on surface with 27000 internal elements.

5.3 Results and Discussion

The simulation was carried out over the cardiac cycle with a time-step of 0.04ms. This corresponds to 1000 timesteps per MRI phase interval. A non-dimensional time parameter, t^* was defined as:

$$t^* = \frac{t}{T_0} \tag{5.1}$$

where T_0 was the total time for one cardiac cycle. The varying geometry of the left ventricle is shown in Figure 5.2 and 5.3.
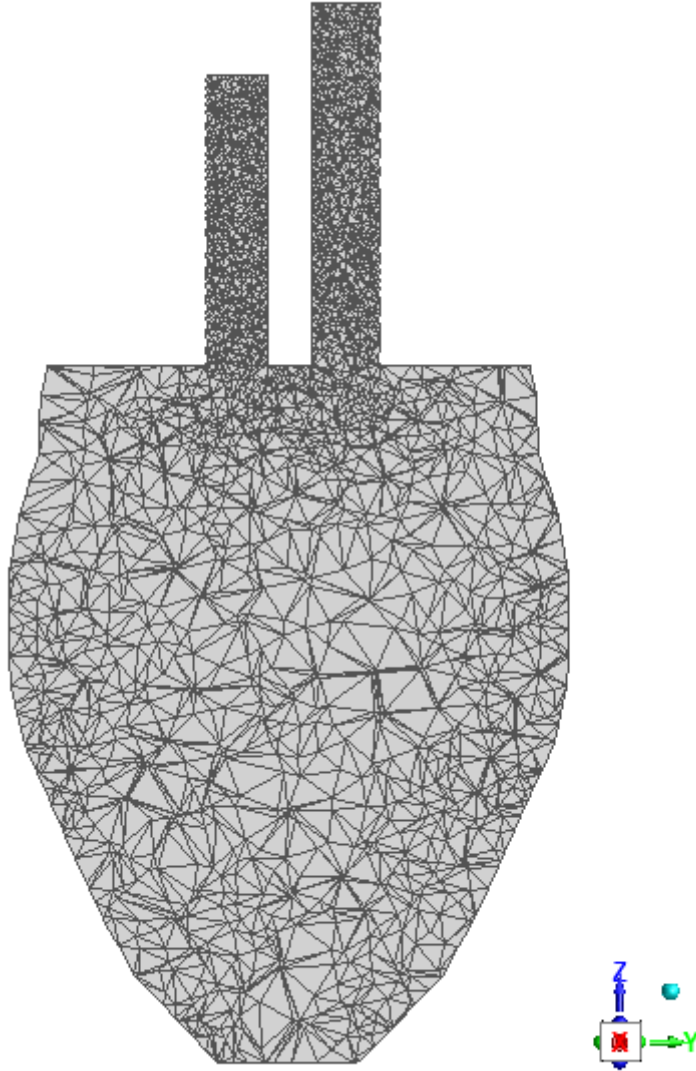
Figure 5.2: Model geometry at $t^* = 0$.
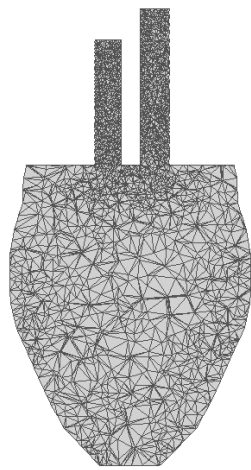
(a) Model geometry at $t^* = 0$.
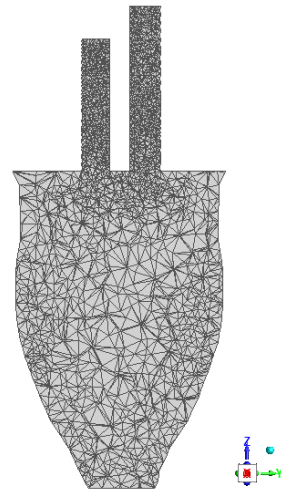
(b) Model geometry at $t^* = 0.2$.
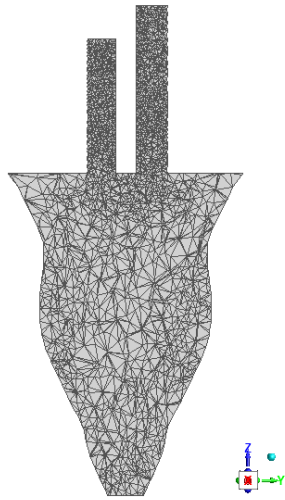
(c) Model geometry at $t^* = 0.4$.
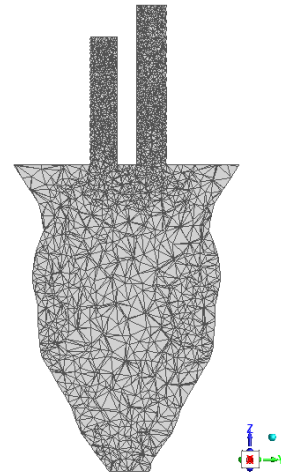
(d) Model geometry at $t^* = 0.6$.
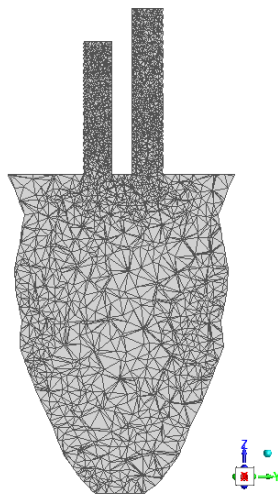
(e) Model geometry at $t^* = 0.8$.
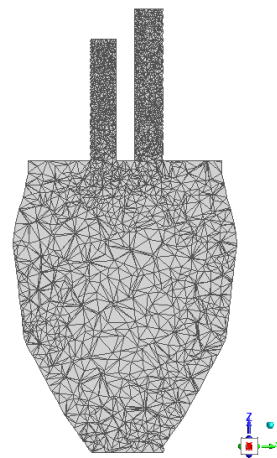
(f) Model geometry at $t^* = 1$.

Figure 5.3: Model geometries at various times through the cardiac cycle.

As can be seen in the above figures, the volume and shape of the left ventricle changed dramatically over time. This is quantified by Figures 5.4 & 5.5 which depict the change in volume, and the flow of blood into and out of the left ventricle over the cardiac cycle. Four distinct phases were seen. Phase 1 in Figure 5.4 (duration: 0.3s) corresponded to the ejection phase where the left ventricle contracts and expels blood. Phase 2 or the rapid inflow phase (duration: 0.28s) was the phase where the left ventricle expands, allowing blood to enter the chamber rapidly and fill it. This was followed by Phase 3 or the diastasis phase i.e. where the left ventricle volume did not change dramatically (duration: 0.32s). The cardiac cycle concluded with Phase 4 where the atrial contraction caused blood to flow into the left ventricle and the volume to increase (duration: 0.08s). The non-dimensional volume fraction, V^* was defined as:

$$V^* = \frac{V}{V_0} \qquad (5.2)$$

where V_0 was the maximum LV volume during the cardiac cycle.
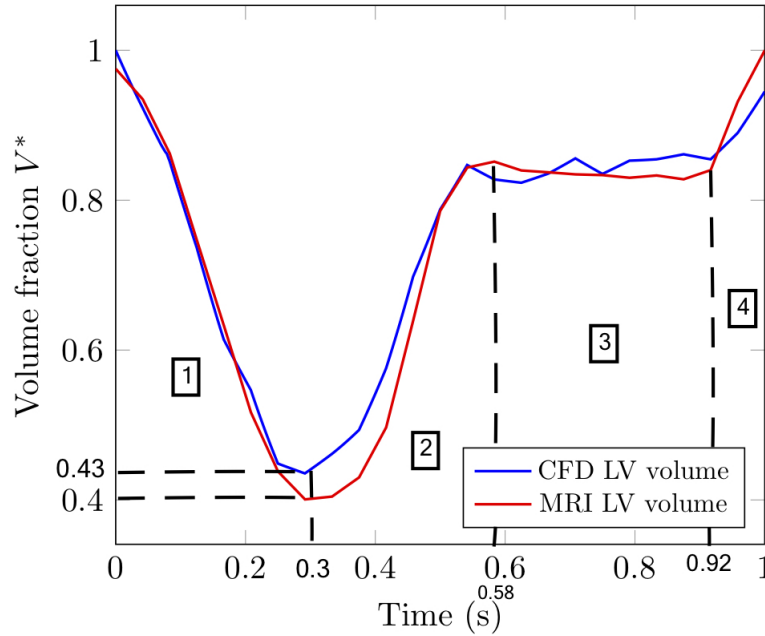
Figure 5.4: Volume of computational left ventricle varying over cardiac cycle. Four distinct phases are seen, (1) ventricular contraction, (2) rapid filling, (3) slow filling, (4) final filling during atrial contraction.

Broad agreement between the volumetric changes of the computational LV model and real LV were seen. When the ejection fraction was calculated from the computational model, a value of 57% was obtained which was in close agreement with the ejection fraction as obtained from cardiac MRI measurements of 60%. There were some discrepancies in the computational model obtained. The volume of the left ventricle reduced slightly and increased in Phase 3 as seen in Figure 5.4, whereas the volume should remain mostly constant with a slight increase. Furthermore, the duration of CFD ventricular rapid inflow was shorter than actual values. This discrepancy could be attributed to some inaccuracies during the segmentation process of the short-axis contours for the reconstruction of the ventricular geometry. Some inaccuracy may also result from the use of linear interpolation between the discrete MRI cardiac phases. Alternative interpolation schemes, such as a Bezier cubic interpolation may be more accurate, and warrant further investigation. The stair steps seen in Figure 5.5 may be due to the linear interpolation scheme used between consecutive time slices.
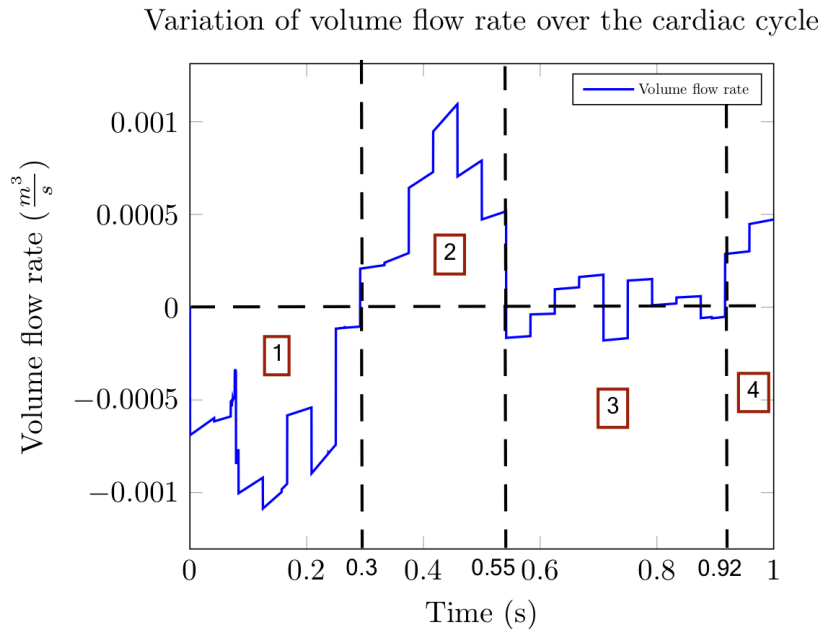
Figure 5.5: Volumetric flow rate of computational left ventricle varying over cardiac cycle. Four distinct phases are seen, (1) ventricular contraction, (2) rapid filling, (3) slow filling, (4) final filling during atrial contraction.

The internal flow dynamics near the end of the atrial contraction phase are shown in Figures 5.6–5.9. It was observed that the fluid had enough momentum to reach the base of the left ventricle. Furthermore, two recirculating regions were seen, one on either side of the main jet. Recirculating regions are most often seen close to the mitral and aortic valves when modeled comprehensively with a realistic inlet and outlet and valve leaflets. Given the lack of complexity of the current model, these vortices were not seen near the valves. Moreover, the inflow jet had a velocity of approximately 1.34 ms^{-1}. This was considerably higher than the normal range of $0.3 - 0.5$ ms^{-1} as measured by cardiac MRI or Doppler velocity measurements. This resulted from approximating the inlet diameter to be much smaller than the actual diameter of the mitral valve inlet so that the dynamic mesh sequence would not fail and the simulation would run.
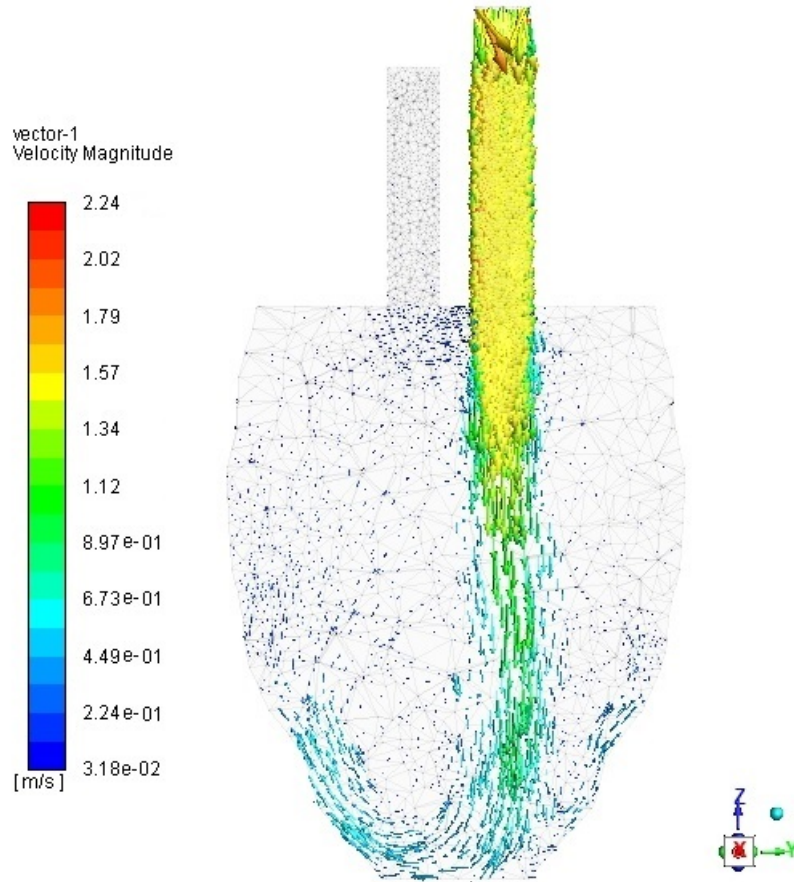
Figure 5.6: Velocity Vectors at $t^* = 1$.
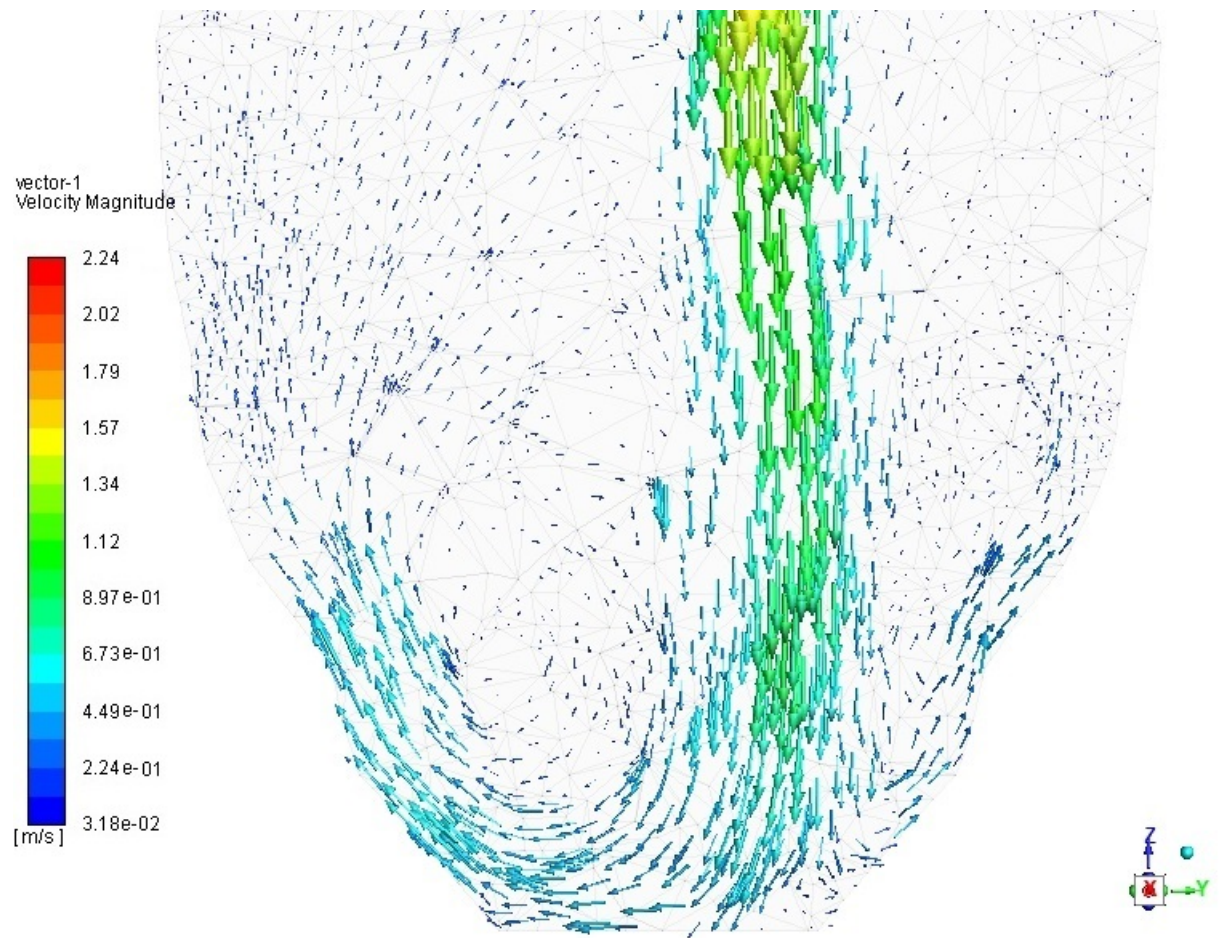
Figure 5.7: Velocity Vectors at $t^* = 1$. A close-up view is provided to show the fluid reaching the base and two recirculating regions, one on either side of the inlet jet.
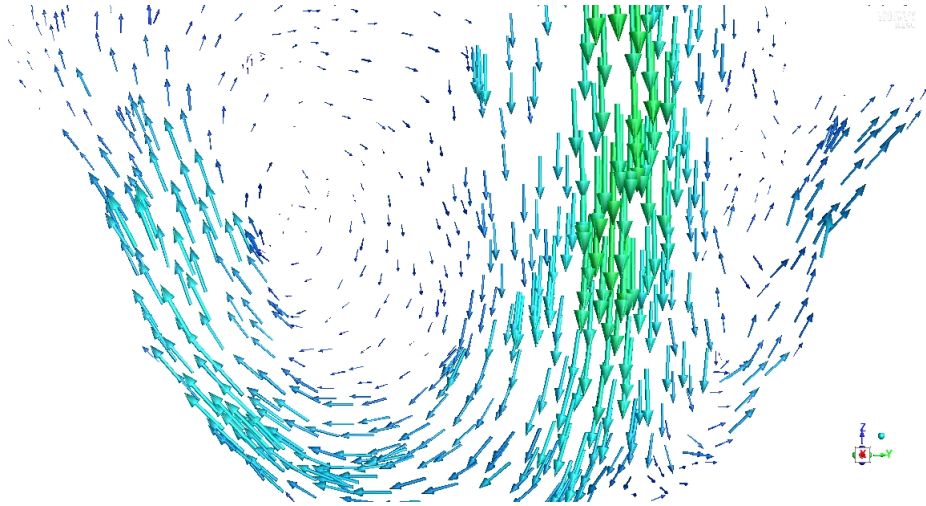
Figure 5.8: Velocity Vectors at $t^* = 1$. A close-up is provided of the large recirculating region.
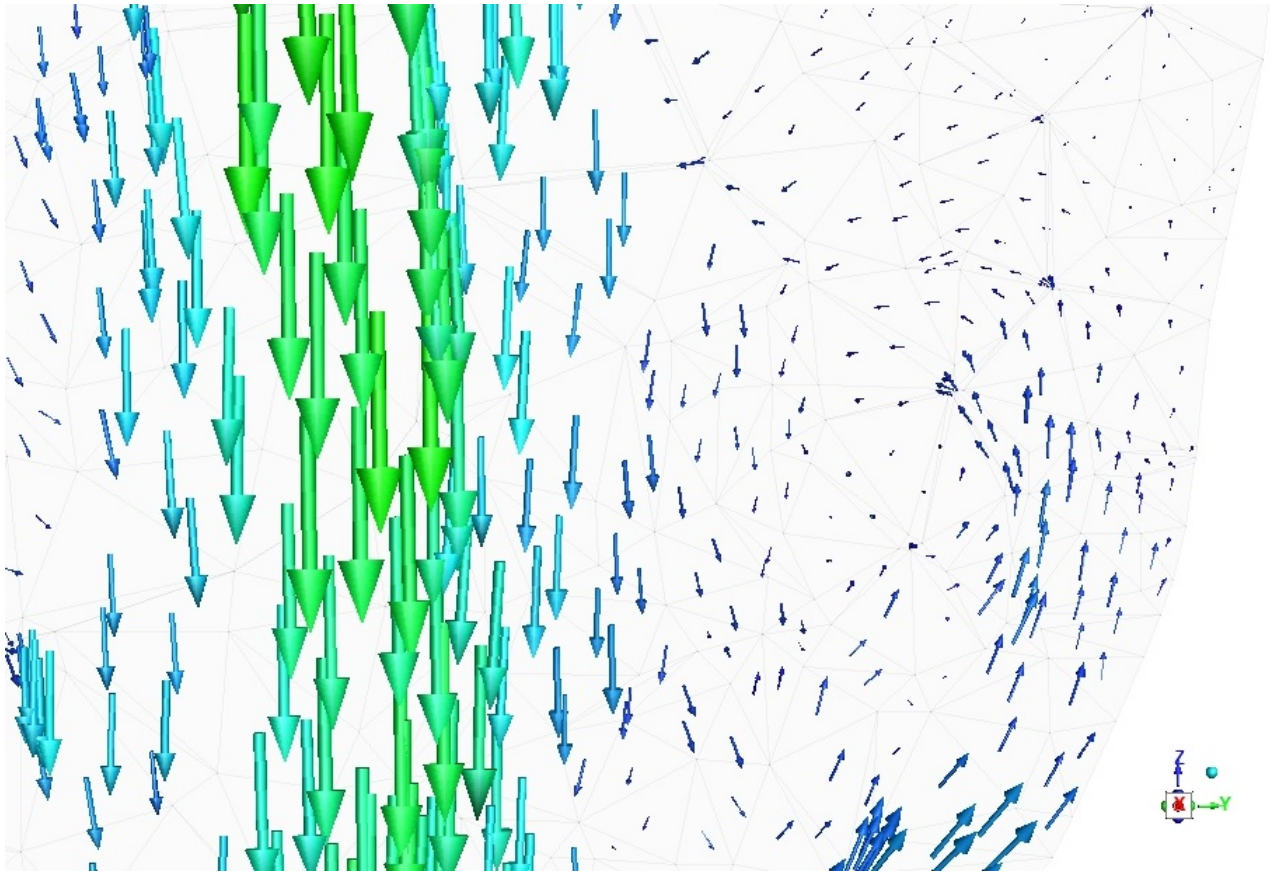
Figure 5.9: Velocity Vectors at $t^* = 1$. A close-up is provided of the small recirculating region.

The results obtained are promising as they demonstrate that the dynamic mesh routine works when applied to the left ventricle. However, further work must be undertaken to model the dynamic motion of the atrial inlet and the aorta outlet.

Alternatively, an immersed boundary method may be more appropriate to model the contraction and expansion of the endocardium. Such an approach may be more useful, as it can accommodate complex geometries, the motion of the ventricular wall, and fluid-tissue interaction. It is also more preferable as it allows for large grid deformation and is noted for its efficiency.

5.4 Summary

Post processing of short-axis images of the endocardium allows the geometric reconstruction of the left ventricle. We investigated the ventricular fluid dynamics by developing an initial computational fluid dynamics model (CFD) of the left ventricle. The effect of the pumping action of the left ventricular wall on blood flow was highlighted. It was seen that the variation of volume in the computational model agreed well with the realistic MRI variation of volume over the cardiac cycle. Furthermore, the derived ejection fraction of 57% agreed closely with the value obtained from cardiac MRI measurements of 60%. Intraventricular vortices were unable to be investigated in relation to the progression of cardiac disease as this required a comprehensive modelling of the mitral valve inlet, aorta outlet and valve leaflets. Nevertheless, a major and minor recirculating region was seen close to the base of the left ventricle on either side of the main inlet jet at the end of the atrial contraction phase. The framework provided here, if further developed, may be used to investigate vorticity and wall-shear stress as biosensitive markers for cardiac dysfunction. Investigating ventricular fluid dynamics over a large group of healthy patients and those with dsyfunctional hearts will provide further strength to the applicability of these markers.

Chapter 6

Conclusions and Recommended Future Work

6.1   Conclusions

In this thesis, cardiac magnetic resonance imaging data is analyzed and processed to generate residence time distributions and produce the time-varying computational domains for computational fluid dynamics studies. The aim is to develop alternative novel markers for cardiac dysfunction. Review of previous studies highlighted the novelty of using residence time distributions in a cardiovascular setting, and how computational markers such as vorticity and wall shear stress can act as robust noninvasive tools for investigating cardiac dysfunction. These are further explicated in the present thesis. The investigation comprises two broad studies, the conclusions of which are discussed below.

6.1.1   Residence time distributions

Residence time distributions were developed through the use of particle position and time data obtained from cardiac magnetic resonance data. By tracking individual particles and calculating plane crossing times, a quantitative constant related to the RTDs was developed. In the left ventricle, the RTD constant was compared to the

83

left ventricular (LV) ejection fraction, global longitudinal strain (GLS) and T1 native values, as these three measures are often used as markers of cardiac dysfunction.

A significant difference was seen in the LV RTD_c between healthy subjects and patients reporting cardiac dysfunction(1.2 ± 0.13 vs 2.2 ± 0.80, $p < 0.001$). There was also a strong negative correlation between the LV RTD_c and the LVEF ($R = -0.843$, $p < 0.001$). Patients reporting cardiac dysfunction were found to have a wider range of RTD constants than healthy patients. When the RTD constant was compared to the GLS, a strong correlation coefficient of $R = 0.7805$ was seen, and the LVEF and GLS reported a strong negative correlation ($R = -0.926$). A weak correlation was seen between the RTD constant and native T1 time ($R = 0.1517$). Overall, it can be concluded that the left ventricular residence time constant has the capability of distinguishing normal from dysfunctional cardiac function. Moreover, it provides potentially useful extra information by tracking the fate of a small marked volume of blood entering through the atrium as a function of time. The clinical value of this may become more pronounced by tracking the outcomes of patients over time.

In the right ventricle, the RV RTD_c was 1.5 ± 0.2 for the healthy patients compared to 1.8 ± 0.57 for the group with cardiac dysfunction. There was a modest negative correlation between the RVEF and the RV RTD_c ($R = -0.7113$, $p < 0.001$) and a wider range of RTD_c values were seen in the focus group with cardiac dysfunction when compared to the LV RTD_c for the same group. This suggests that relationship between the ejection fraction of the right ventricle and the RV RTD_c may differ from that of the left ventricle and the LV RTD_c.

The right atrial RTD_c differed moderately between healthy volunteers and the sick patients (1.6 ± 0.4 compared to 1.9 ± 0.7). A weak negative correlation was seen between the atrial RTD_c and the LVEF ($R = -0.4543$). This may suggest that the atrial RTD_c may not be an appropriate marker of cardiac dysfunction, or that dilated cardiomyopathy and its symptoms do not present themselves extensively in the right atrium. Overall, the use of the residence time distribution constant may

help clinicians in distinguishing normal from abnormal cardiovascular behaviour, and serve as a early, novel marker during diagnostic evaluation that will improve patient outcomes through early intervention.

6.1.2 Computational Fluid Dynamics

Intraventricular fluid dynamics were visualised by developing a computational model of the left ventricle that expands and contracts over the course of the cardiac cycle. The movement of the endocardial walls were prescribed by the use of user-defined functions (UDFs) in ANSYS-FLUENT. We demonstrate that the change in volume of the computational model was similar to the actual change in volume of the left ventricle when specific phases were considered. Computationally obtained ejection fractions agreed well with the measured ejection fraction (57% versus 60%). When ventricular fluid mechanics were closely investigated, two recirculating regions were seen close to the main inlet jet. However, the ability to visualise vortices that are representative of cardiac dysfunction was impaired by the lack of complexity of the geometric model and the numerous simplifications made. Although the inlet jet had a higher velocity than what was generally expected ($1.4 \text{ m}s^{-1}$ versus $0.3 \text{ m}s^{-1}$), this was mainly due to an approximation of the inlet diameter to be smaller than the actual inlet diameter to ensure the dynamic mesh routine was able to continue and the simulation successfully completed.

Overall, the model explicated here has shown its utility in describing the motion of the left ventricular walls over the cardiac cycle. Further development, if carried out, will allow novel markers such as the vorticity and wall shear stress to be investigated in greater detail.

6.2 Recommendations for future work

Although the present study tries to make developments in this domain, some areas remain under-explored.

- The current study attempted to fit the fraction of particles remaining in the chamber to a negative exponential distribution. Further analysis into the relationship to other distributions, and the similarities of the cardiac model to other reactor models such as the plug flow and laminar flow reactor models will potentially characterise other chambers more accurately. Additionally, it is beneficial to validate the RTD results obtained computationally with RTD results obtained from artificial heart models. Alternative metrics can also be further investigated, such as the ratio of number of particles exiting the chamber to the number of particles seeded. Age matching the normal subjects and patients with cardiac dysfunction would remove a limitation on the results obtained.

- Improving the current technique so that the particle tracking planes can be generated more stringently will increase the accuracy of the particle tracking data output. Furthermore, investigating the link between residence time and the formation of clots can provide useful insight into a patient's risk factor for stroke.

- Currently, manual segmentation of the LV on multiple images is the standard clinical practice. It is a time-consuming task, and prone to inter and intra-observer variability. To ameliorate this, an automated method should be developed (possibly based on artificial intelligence approaches). This would also allow the accurate and rapid description of left ventricle cardiac function from short-axis MR images without any user interaction.

- The regions where the left ventricle meets the atrium and mitral valve inlet are complex to model, and consequently their motion during the cardiac cycle is difficult to describe. The difficulty in modelling these regions appropriately resulted in the degeneration of the mesh to have negative cell volumes in the current study. Towards the very end of candidature, initial success was obtained using a hybrid approach, detailed in Sections A.2 and A.2.1.

Views of the mesh for the fluid domain are shown in Figure 6.1, with a lighted surface model showing the ventricle/aorta/atrium flow domain during the expansion phase in Figure 6.2.
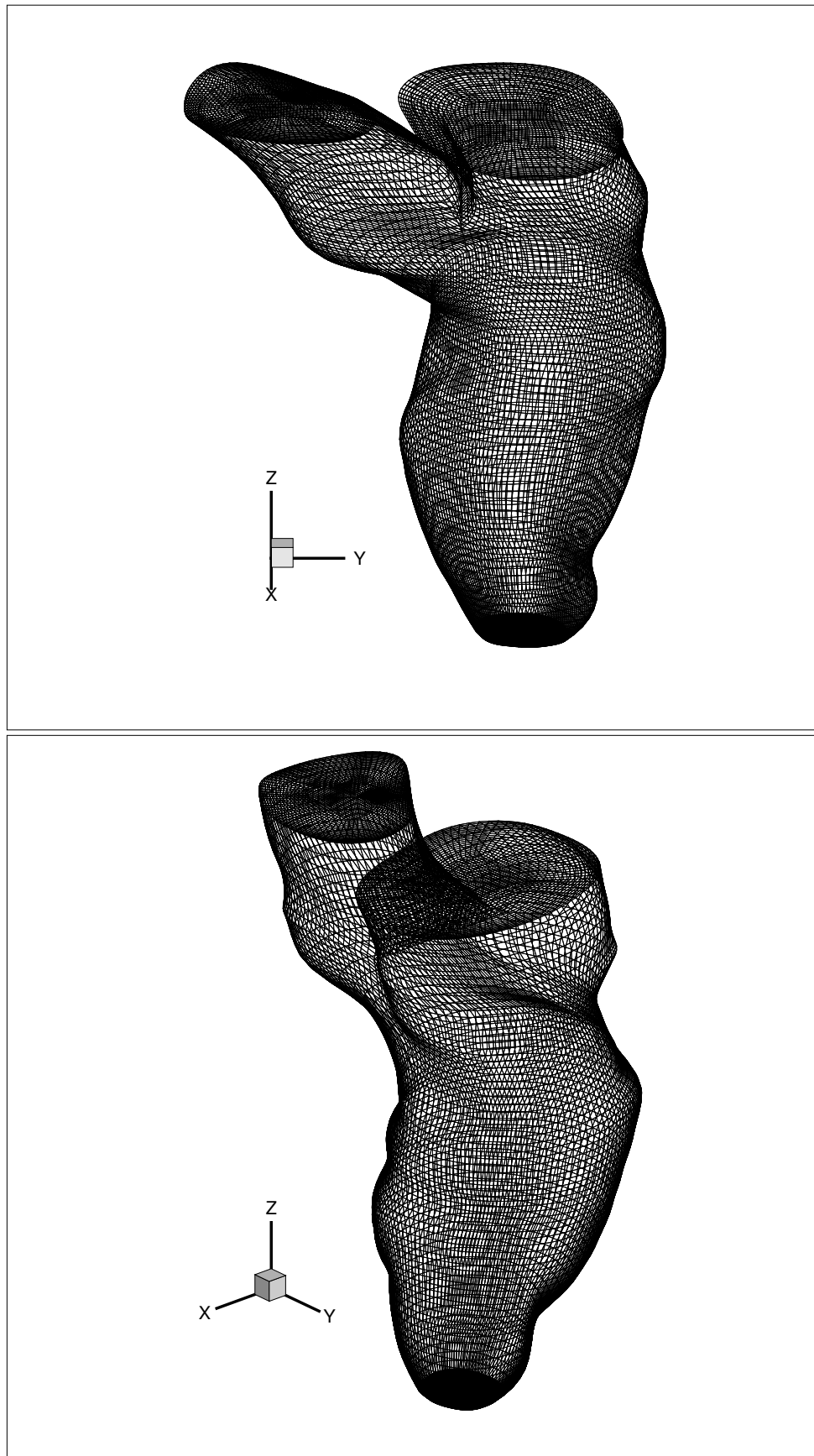
Figure 6.1: Surface mesh of fluid domain for a typical time-slice.
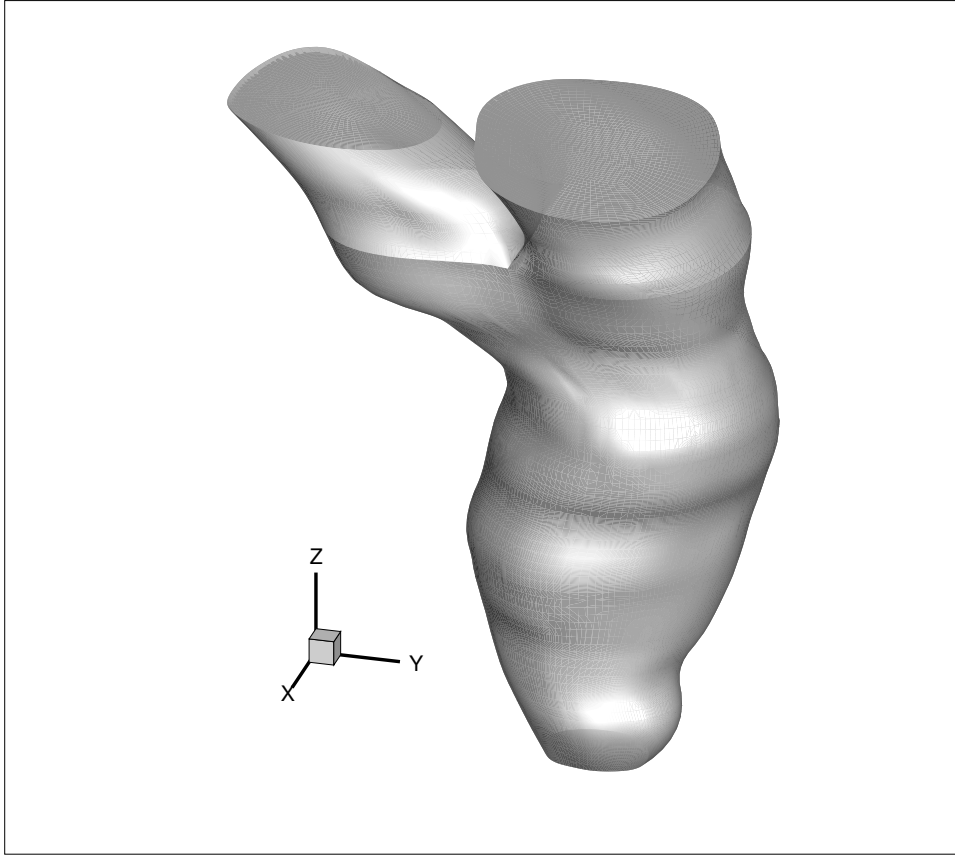
Figure 6.2: Lighted surface model of the ventricle/aorta/ventricle during the ventricle expansion phase.

Images of the blood flow in the computational domain is shown in Figure 6.3. The images correspond to the velocity field on a plane cutting through the centres of the aortic and left atrium inlet/outlets. The colours indicate vertical (z) velocity. The legend is shown on the images in Figure 6.3. They show the velocity fields at maximum inflow and outflow. Evidently blood enters through the mitral valve at approximately 400 mm/sec and exits through the aorta at a speed of more than 500 mm/sec. Full results of the model developed for a single patient are shown in Section A.3.
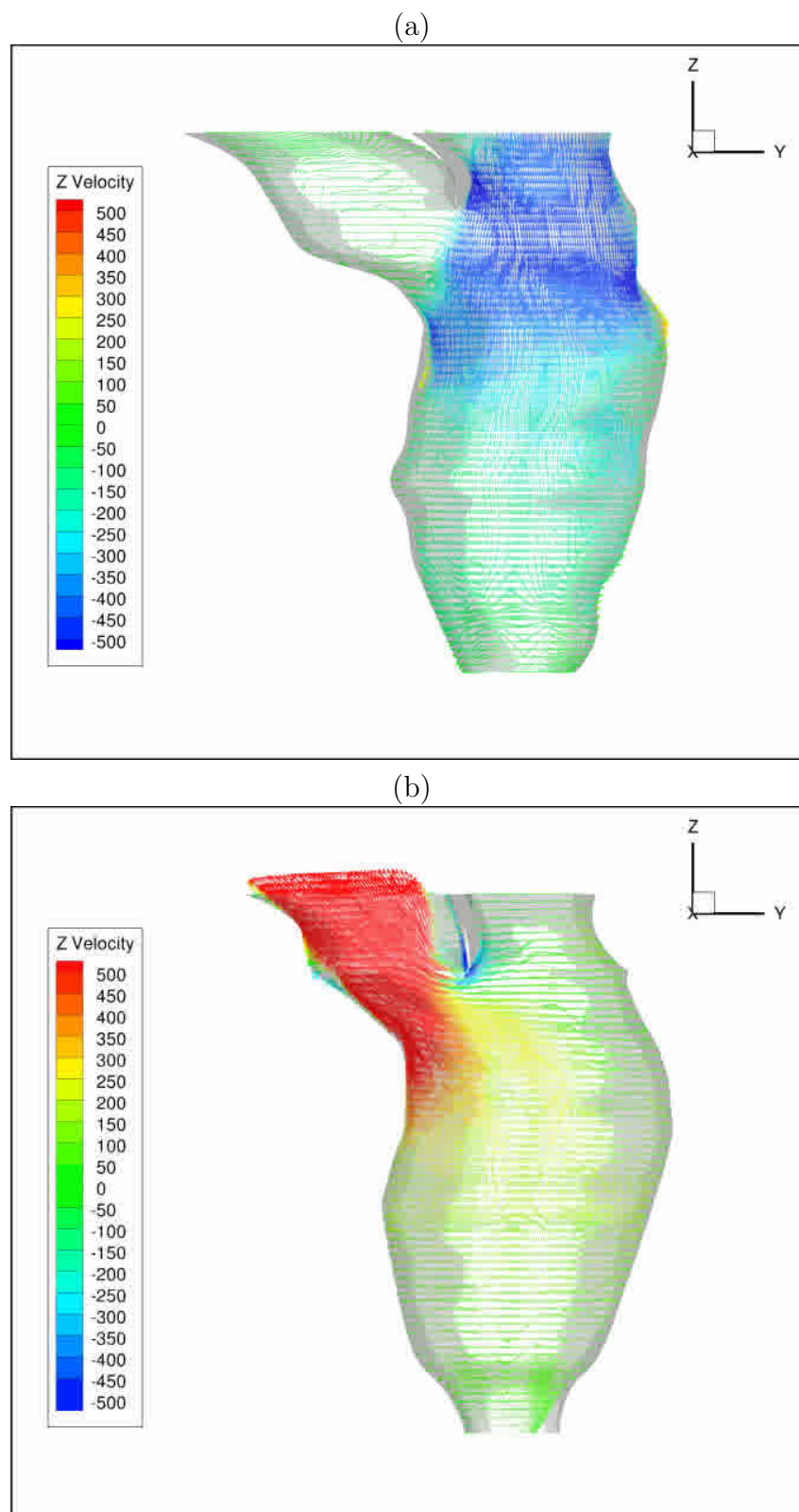
Figure 6.3: Zoomed out images of the velocity fields corresponding to time-slice 12 (maximum inflow) and (b) time-slice 4 (maximum outflow).

Further development of this model to include the motion of the valve leaflets is warranted. Moreover, comparing results for different patients and to investigate the potentially different blood filling and emptying patterns between different patient groups to assess the potential clinical implications of this approach would be useful. Residence time distributions can also be developed from these results. In the future, this would allow potential markers to be identified and compared between healthy and sick patients.

Appendix A

CFD modelling of the blood flow through the left ventricle

A.1 Introduction

As discussed in the methodology chapter, a variety of different approaches were tried to implement a dynamically changing mesh suitable for the CFD flow calculation within the framework provided by ANSYS-FLUENT. Unfortunately, this proved to be more difficult than originally hoped. In particular, the dynamic mesh routines available within FLUENT did not cope well with the considerable distortions involving both translation and compression/expansion. Typically, this resulted in the breakdown of the moving mesh within a small number of timesteps (typically $\sim O(100)$). This generally manifested as the development of negative cell volumes that led to the flow calculation diverging. FLUENT allows two main approaches for mesh movement – a spring based method, which changes cell edge sizes from timestep to timestep as these lengths move away from their initial lengths, and a diffusion based approach, which uses a diffusion analogy to move mesh points during timestepping. The latter approach appeared more successful, but typically still became unstable after a reasonably short integration time. FLUENT also implements remeshing as part of the dynamic mesh process, but this also seemed not

to work well for this case. Other significant complicating factors were: the need to treat the inflow and outflow through separate vessels (aorta and atrium) that needed to be effectively treated separately but maintaining consistency with the ventricle movement; the need to maintain a reasonable mesh point distribution, especially to resolve the flow near the vessel walls; and approximating the effect of the flow of the heart valves (aortic and mitral valves). Preliminary success was achieved with the following hybrid approach.

A.2 Mesh generation

To have greater control in maintaining mesh point distribution for resolving the thin boundary layers, an alternative approach was pursued. This was different from the approaches described previously i.e. Delaunay triangulation of the surface mesh, or using SolidWorks for surface generation with ANSYS-FLUENT meshing. These previously described approaches may be useful in the future.

Centroids of each short-axis contour of the ventricle were found. Raw contour points were interpolated onto equi-spaced points at incremental angles (typically 1 degree) relative to the centroid of the contour. This was carried out for the complete stack of short-axis contours (15 contours). Points with similar angle relative to the centroid were used in a cubic spline interpolation scheme to add points that defined intermediate contours. This increased the resolution in the z (long-axis) direction. Centroid points were also interpolated.

Next, a surface mesh was constructed for each contour. To maintain an appropriate resolution where the ventricular model branches into the left atrium and the aorta, a cross-sectional mesh was used and is shown in Figure A.1. The schematic shows the stages in constructing this cross-sectional mesh by mapping circular meshes. This permits excellent mesh point concentration towards the walls, which is controlled by a compression parameter, and a natural split as the ventricular domain cross-sectional topology changes from the ventricle cross-sections to the aorta/atrium cross-sections. A closer view of the cross-sectional mesh is provided

in Figure A.2 that shows an the increased mesh point concentration towards the boundaries.
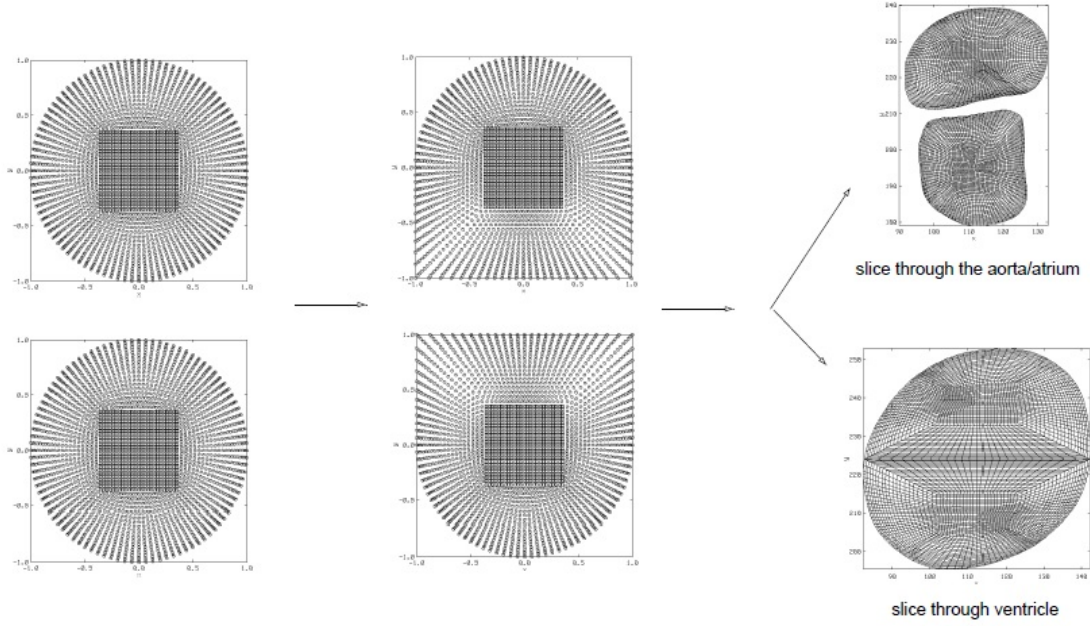
Figure A.1: Stages in generating intermediate short-axis cross-sectional meshes used to build the 3D mesh.

After this stage, the resulting cross-sectional meshes were stacked and used to form a three-dimensional mesh built of hexahedral elements. This mesh was converted into FLUENT file format *msh* so that it could be read into FLUENT. This process was carried out for all time slices across the cardiac cycle.

Views of the mesh for the fluid domain are shown in Figure A.3, with a lighted surface model showing the ventricle/aorta/atrium flow domain during the expansion phase in Figure A.4.
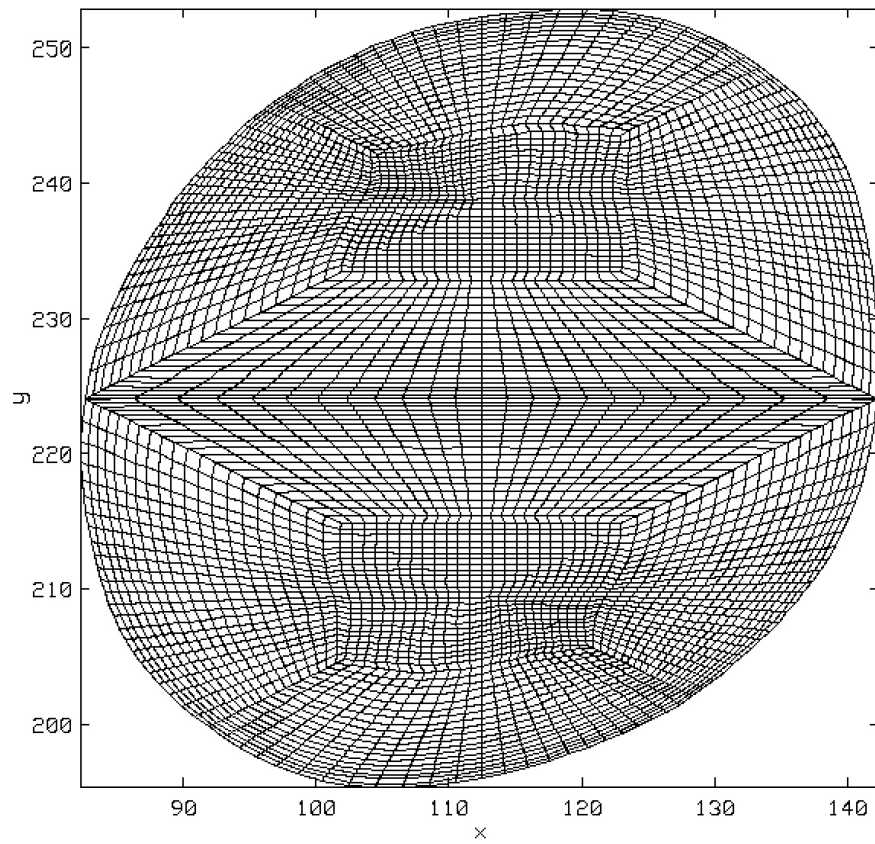
Figure A.2: Zoomed in view of cross-sectional mesh through the ventricle showing increased concentration towards the walls.
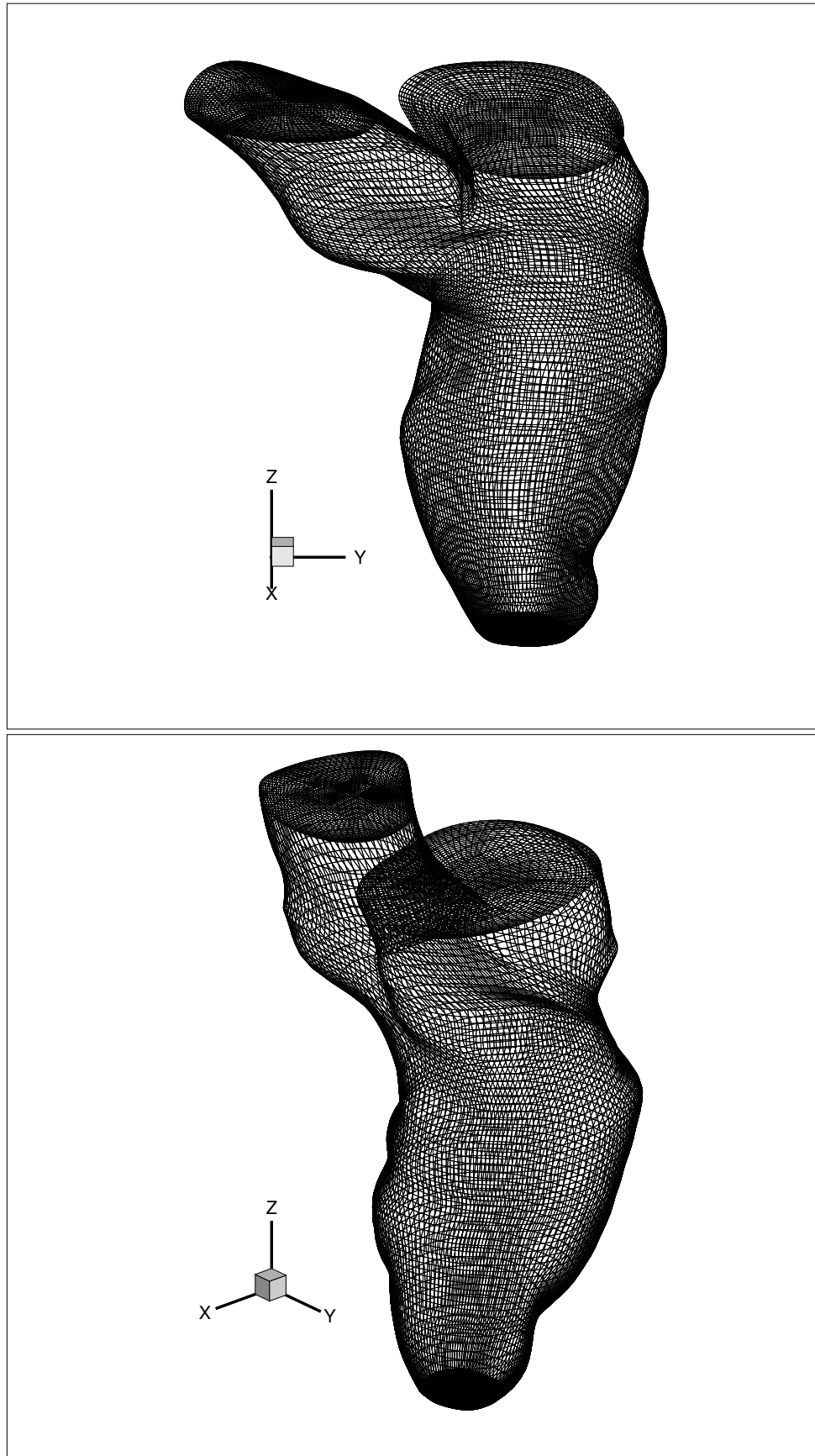
Figure A.3: Surface mesh of fluid domain for a typical time-slice.
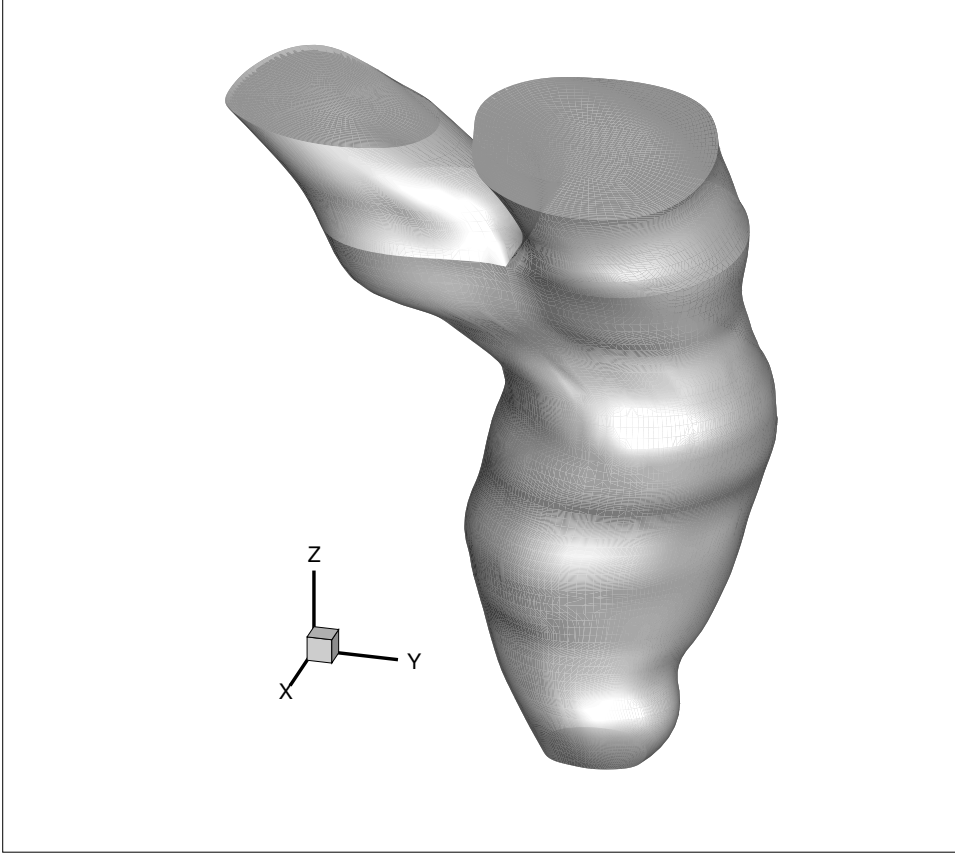
Figure A.4: Lighted surface model of the ventricle/aorta/atrium during the ventricle expansion phase.

To model the connection of the aorta and the left atrium to the top of the ventricle, the top contour (where splitting happens) was directly divided in half. The upper half splits into the left atrium, whereas the lower half splits into the aorta. This was done by firstly rotating the short axis contours so that the transition into the aorta/atrium occurred approximately along the split. The process used is outlined in Figure A.5.

For this model, the mesh consists of 4992 quadrilateral cells on each cross-sectional slice. These were connected to form the 3D hexahedral mesh of the ventricle/atrium/aorta by 70 slices in the z (long-axis) direction. Therefore, the 3D computational mesh contained approximately 350K cells, as a first attempt to resolve the blood flow. Whilst this may likely be insufficient to fully resolve the internal blood flow, it should provide a reasonable first approximation.

Using a process that moves the mesh points as a substep of each timestep through

initial timeslice – ventricle/aorta/atrium contours
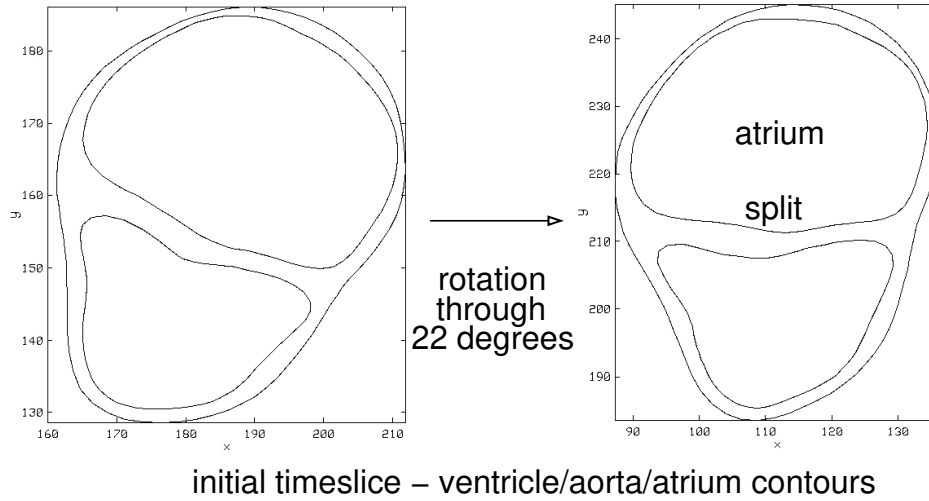
Figure A.5: Treatment of the bifurcation between the ventricle, and atrium and aorta. Initially, contours are rotated so that there is an approximately horizontal line between the aorta and the atrium. The top section forms the exit of the atrium into the left ventricle, and the bottom section defines the entry into the aorta. The details of the valve geometries are not included in this version of the model.

FLUENT's dynamic mesh routine is computationally expensive. Unoptimised initial simulations over the full cardiac cycle took approximately 8 hours on a 12 core processor. However, the mesh generation is parameterised; thereby making it easier to generate a more refined mesh and undertaking a full resolution study. This will occur as part of the project continuing in the future.

A.2.1 Dynamic mesh considerations

Movement of the mesh during the simulation was not completely stable, and it was prone to fail after integrating through a few of the 25 time frames. Occasionally, it could be worse than that and not even survive the 50 timestep integration between one time slice and the next. To avoid this problem, a new, undistorted mesh generated for the particular time using the process described above was routinely read in. The velocity field from the current mesh was interpolated to the new mesh. Fortunately, FLUENT has built in interpolation procedures that allow this process to be semi-automated. Once a new mesh had been read in and the velocity field initialised, the integration proceeded for another half a time-slice period – typically 1/50th of a cardiac cycle – before repeating the process again. This procedure was a

little messy in practice, because the boundaries were renamed when their boundary type was changed, so initial testing was required to turn the process into a working procedure. At present, a timestep of 0.0008 cardiac periods is chosen for the computational timestep – giving 12500 timesteps per cycle. This is likely to be sufficient to resolve the flow in time.

To move the surface points of the left ventricle, aorta and left atrium, the dynamic mesh model requires user-supplied functions. These three routines were constructed by matching each point supplied by FLUENT during its dynamic re-meshing as part of each timestep with where that point should be given the required mesh movement. This required interpolation from the surface points for each timeslice, in time, long-axis position and angular position from the centroid. Given that the time slices were at fixed time intervals, as were the points in z, interpolation in these two directions was easy and relatively computationally cheap. To find the matching point in the azimuthal direction was more complicated. After some testing, the method used was a half interval search – a match was assumed if the supplied and tested points matched to within a pre-supplied tolerance. Whilst locating how the supplied surface mesh point moved to a new position during the timestep was slightly computationally expensive, the dynamic mesh movement process that FLUENT used to move internal points was much more time intensive. Note that quadratic interpolation was used in time using the three closest timeslices. Cubic spline interpolation was used to compute the positions of the surface mesh points in the long-axis direction. This was supplied to the user-supplied mesh point movement functions.

To summarise, during a timestep over which the flow solution was updated, each surface point on the left venticle, aorta and left atrium was moved to a new position through three user-supplied functions. Once this was done, then FLUENT moved the internal points of the mesh based on its diffusion dynamic meshing approach, as part of the update during a timestep. The flow solution was calculated based on the iterative unsteady *SIMPLE* algorithm, which iterates from the start to the end

of the timestep until the solution converges at the next timestep. Convergence was tested by determining how well each of the discretised governing (3 momentum + 1 continuity) equations were satisfied by the current solutions in a relative L2 norm sense (refer to the FLUENT reference manual for details). For the current model, relative convergence criteria of 0.0001 was chosen for each equation. Although this was an order of magnitude below the default, it was generally sufficient for reasonable time-integration convergence. This should be tested/verified in future model development. Typically 10-20 (SIMPLE) iterations were required for each timestep to satisfy the convergence criteria, although it occassionally required more iterations after the fluid velocity was interpolated from one mesh to the next.

A.2.2   Modelling the effect of the Aortic and Mitral valves

The current implementation did not really make an attempt to model the complex flow associated with the dynamic geometry of the left ventricle heart valves. The model was simplified considerably by approximating the process through inlet/outlet pressure boundary conditions at the top of the aortic and atrial domain sections of the mesh. Ideally, these sections would be longer; in particular, the aortic entry was quite short and did not include any part of the aortic arch. This was because, the sections of the aorta and left atrium were generated based on only two short-axis contours beyond the ventricle/aorta/atrium branching cross-section. Future developments would treat this by, at least, adding on sections to the top of the domain to make both the inlet and outlet longer.

A.3   Flow calculation

The approximate variation of left ventricular volume including the short sections of the aorta and left atrium is shown in Figure A.6(a). The volume was measured by adding the approximate volumes of each computational cell in the fluid domain. The volume that included solely the left ventricle is shown in Figure A.6(b). The

minimum and maximum LV volume achieved over the cycle was approximately 160,000 and 320,000 mm^3, giving an ejection fraction of $\sim 50\%$.
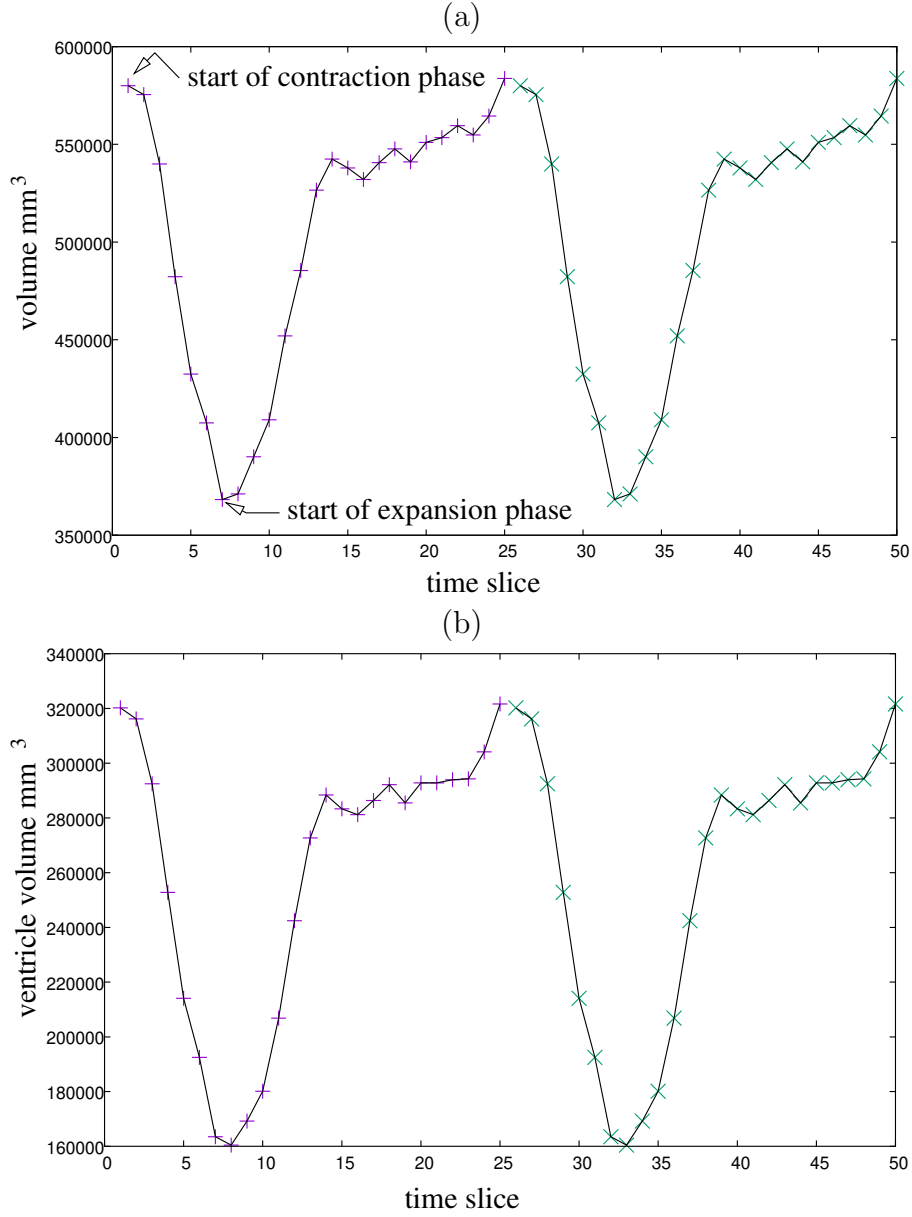
Figure A.6: Volume variation of the left ventricle over a cardiac cycle. (a) includes the sections of the aorta and left atrium; (b) left ventricle only. The first stage is a contraction stage that results in blood ejection into the aorta. This is followed by an expansion phase when the left ventricle fills, after which the expansion slows down prior to the next contraction.

The simulation began from the mesh corresponding to time slice 7, which was at the minimum overall volume. This was approximately the beginning of the expansion phase i.e. where blood enters from the left atrium into the left ventricle as the heart muscle relaxes. During this stage, the aortic valve should be closed.

Hence for this part of the simulation, a no-slip boundary condition was applied at the top of the aortic section while the inlet through the atrium was set to an inlet pressure boundary condition. This allowed flow into the domain driven by the expansion of the left ventricle. The aorta, left atrium and left ventricle surface were defined through user-supplied functions, enabling these surfaces to move from one timestep to the next. At the top and bottom boundaries, *deforming* wall boundary conditions were used. These required the specification of the plane defining each of these boundaries. The movement of points on these surfaces was controlled by FLUENT's diffusion dynamic mesh model. Motion was restricted to the specified planes. At this stage of the model development, it was assumed that there was no expansion along the long-axis, which was false, and should be included as the model is developed further.

The governing equations were integrated forward in time for half a time-slice period (1/50th of a cardiac cycle). At this stage, the velocity and pressure fields were saved and a new mesh replaced the mesh that had been distorted as part of the dynamic meshing procedure. The velocity and pressure fields were then interpolated onto the new mesh, boundary conditions were checked and the calculation continued. This process continued until the contraction phase of the cycle began at time-slice 25. At this point in the cycle, the pressure inlet boundary condition at the top of the left atrium subdomain was changed to a no-slip condition (sealing the mitral valve) and the no-slip boundary at the top of the aorta subdomain was switched to a pressure outlet condition. This allowed blood to exit through the aorta as the heart muscle underwent a rapid contraction phase. After the inlet/outlet boundary conditions were reset, the calculation proceeded as before. After again reaching time-slice 7 of the cycle, the boundary conditions were once again reset back to the original conditions, and the process repeated.

Images of the blood flow over a cycle are shown in figure A.7. As indicated, the initial time corresponded to time-slice 7. The velocity fields shown are between time-slices, so that the first image is at time-slice 7.5. The images correspond to the

velocity field on a plane cutting through the centres of the aortic and left atrium inlet/outlets. The colours indicate vertical (z) velocity. The legend is shown on the images in Figure A.8. They show the velocity fields at maximum inflow and outflow. It appears that blood enters through the mitral valve at approximately 400 mm/sec and exits through the aorta at a speed of more than 500 mm/sec. These values are close to agreeing with representative velocities obtained from cardiac MRI and Doppler measurements (0.3 – 0.5 m/s). At the phase shown in Figure A.8(b), the outflow through the exit plane was reasonably uniform; however, this was not so at later times (see images 24 and 25 of figure A.7). This may be an effect of the reduced outlet length and warrants further investigation.

Overall, after entering the left ventricle, the blood appeared to undergo a reasonable amount of mixing before exiting. This was indicated by reasonable flow motion over most of the left ventricle in the long phase prior to ejection. This can be seen through zoomed in views of the velocity vectors. In particular, there does not appear to be any *dead zones*, where the blood recirculates or pools, as might possibly be the case for a dysfunctional heart, with a low ejection fraction. Clearly, comparing the results obtained here with a heart from the group of patients with cardiac dysfunction would be useful but has not yet been done due to lack of time.
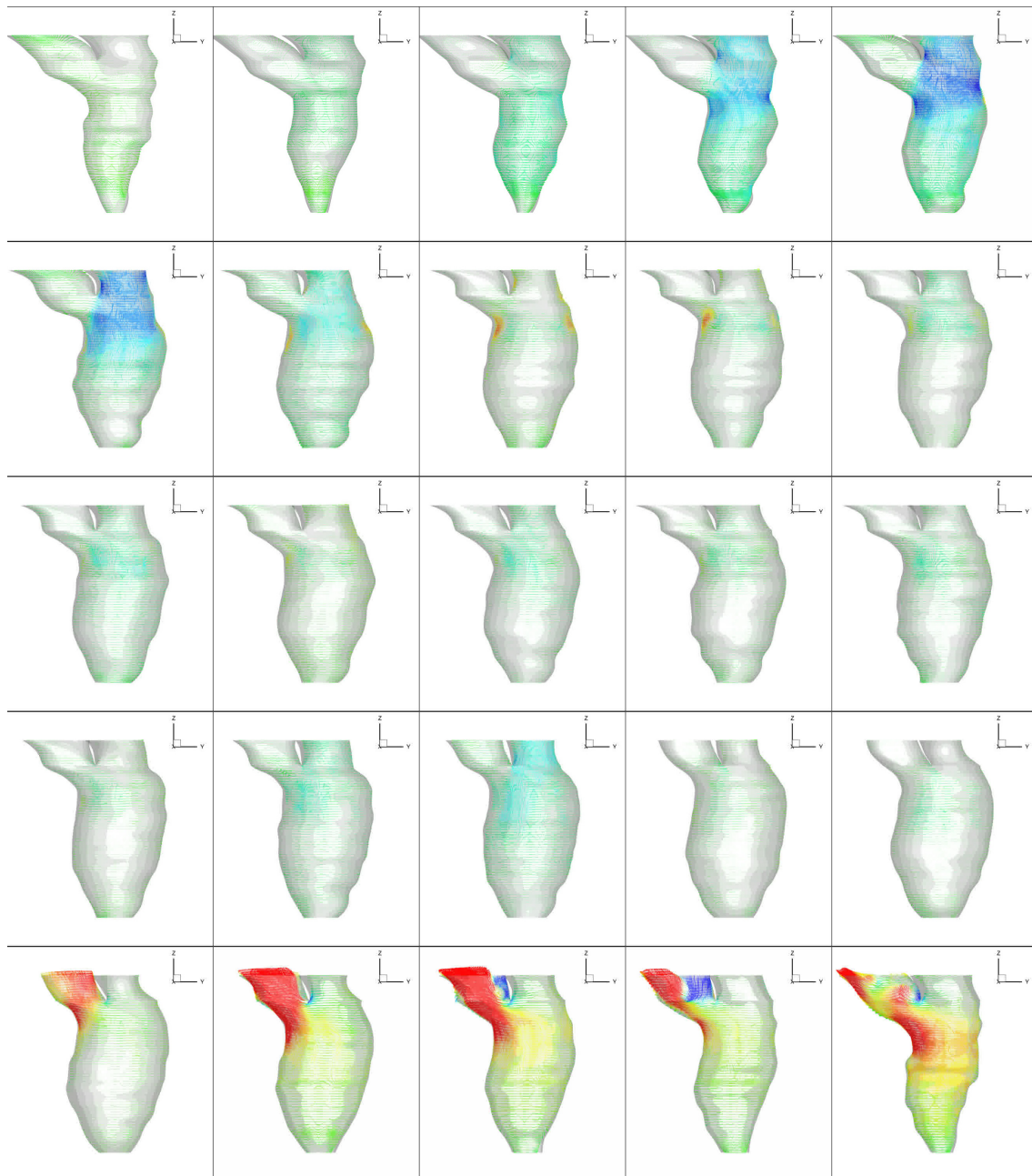
Figure A.7: Variation of blood flow through the left ventricle during a cardiac cycle. The velocity vectors are shown in the centre plane passing through the aorta/left atrium as described in the text. The lighted translucent surfaces show the surface of the fluid domain. Images correspond to time-slices 7.5, 8.5, 9.5, etc, left to right and then top to bottom.

(a)

(b)
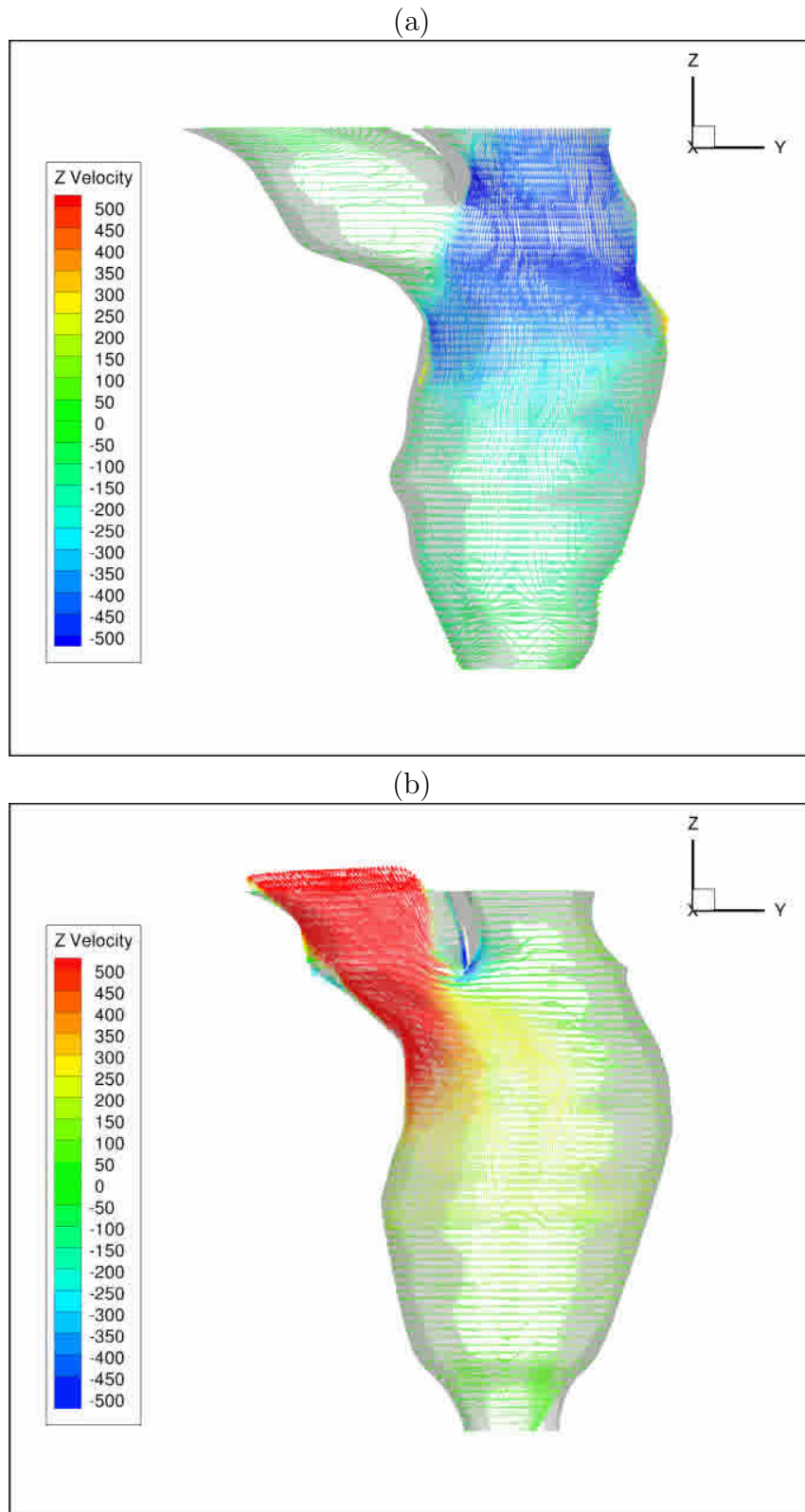
Figure A.8: Zoomed out images of the velocity fields corresponding to time-slice 12 (maximum inflow) and (b) time-slice 4 (maximum outflow).

Bibliography

ADAMO, L., PERRY, A., NOVAK, E., MAKAN, M., LINDMAN, B. R. & MANN, D. L. 2017 Abnormal global longitudinal strain predicts future deterioration of left ventricular function in heart failure patients with a recovered left ventricular ejection fraction. *Circ Heart Fail* **10** (6).

ADRIAANS, B. P., WESTENBERG, J. J., VAN CAUTEREN, Y. J., GERRETSEN, S., ELBAZ, M. S., BEKKERS, S. C., VEENSTRA, L. F., CRIJNS, H. J., WILDBERGER, J. E. & SCHALLA, S. 2020 Clinical assessment of aortic valve stenosis: Comparison between 4d flow mri and transthoracic echocardiography. *Journal of Magnetic Resonance Imaging* **51** (2), 472–480.

ASHISH, K., FAISALUDDIN, M., BANDYOPADHYAY, D., HAJRA, A. & HERZOG, E. 2019 Prognostic value of global longitudinal strain in heart failure subjects: A recent prototype. *Int J Cardiol Heart Vasc* **22**, 48–49.

BACCANI, B., DOMENICHINI, F. & PEDRIZZETTI, G. 2002*a* Vortex dynamics in a model left ventricle during filling. *European Journal of Mechanics - B/Fluids* **21** (5), 527 – 543.

BACCANI, B., DOMENICHINI, F. & PEDRIZZETTI, G. 2003 Model and influence of mitral valve opening during the left ventricular filling. *J Biomech* **36** (3), 355–61.

BACCANI, B., DOMENICHINI, F., PEDRIZZETTI, G. & TONTI, G. 2002*b* Fluid dynamics of the left ventricular filling in dilated cardiomyopathy. *Journal of Biomechanics* **35** (5), 665 – 671.

BASURAY, A., FRENCH, B., KY, B., VOROVICH, E., OLT, C., SWEITZER, N. K., CAPPOLA, T. P. & FANG, J. C. 2014 Heart failure with recovered ejection fraction. *Circulation* **129** (23), 2380–2387.

BESL, P. J. & MCKAY, N. D. 1992 A method for registration of 3-d shapes. *IEEE Transactions on Pattern Analysis and Machine Intelligence* **14** (2), 239–256.

BIERING-SORENSEN, T., MOGELVANG, R. & JENSEN, J. S. 2015 Prognostic value of cardiac time intervals measured by tissue doppler imaging m-mode in the general population. *Heart* **101** (12), 954–60.

BIGA, L. M., DAWSON, S., HARWELL, A., HOPKINS, R., KAUFMANN, J., LEMASTER, M., MATERN, P., MORRISON-GRAHAM, K., QUICK, D. & RUNYEON, J. 2016 *Anatomy & Physiology*. OpenStax & Oregon State University.

BOLGER, A. F., HEIBERG, E., KARLSSON, M., WIGSTROM, L., ENGVALL, J., SIGFRIDSSON, A., EBBERS, T., KVITTING, J. P., CARLHALL, C. J. & WRANNE, B. 2007 Transit of blood flow through the human left ventricle mapped by cardiovascular magnetic resonance. *J Cardiovasc Magn Reson* **9** (5), 741–7.

BOLZON, G., ZOVATTO, L. & PEDRIZZETTI, G. 2003 Birth of three-dimensionality in a pulsed jet through a circular orifice. *Journal of Fluid Mechanics* **493**, 209–218.

CHAN, B. T., LIM, E., CHEE, K. H. & ABU OSMAN, N. A. 2013 Review on CFD Simulation in Heart with Dilated Cardiomyopathy and Myocardial Infarction. *Comput. Biol. Med.* **43** (4), 377–385.

CHENG, R. K., COX, M., NEELY, M. L., HEIDENREICH, P. A., BHATT, D. L., EAPEN, Z. J., HERNANDEZ, A. F., BUTLER, J., YANCY, C. W. & FONAROW, G. C. 2014 Outcomes in patients with heart failure with preserved, borderline, and reduced ejection fraction in the medicare population. *Am Heart J* **168** (5), 721–30.

CHENG, Y., OERTEL, H. & SCHENKEL, T. 2005 Fluid-structure coupled cfd simulation of the left ventricular flow during filling phase. *Ann Biomed Eng* **33** (5), 567–76.

COSTELLO, B., QADRI, M., PRICE, B., PAPAPOSTOLOU, S., THOMPSON, M., HARE, J., LA GERCHE, A., RUDMAN, M. & TAYLOR, A. 2018 The ventricular residence time distribution derived from 4d flow particle tracing: a novel marker of myocardial dysfunction. *International Journal of Cardiovascular Imaging* **34** (12), 1927–1935.

CURTIS, J. P., SOKOL, S. I., WANG, Y., RATHORE, S. S., KO, D. T., JADBABAIE, F., PORTNAY, E. L., MARSHALKO, S. J., RADFORD, M. J. & KRUMHOLZ, H. M. 2003 The association of left ventricular ejection fraction, mortality, and cause of death in stable outpatients with heart failure. *J Am Coll Cardiol* **42** (4), 736–42.

DANCKWERTS, P. 1953 Continuous flow systems: Distribution of residence times. *Chemical Engineering Science* **2** (1), 1 – 13.

DOMENICHINI, F. & PEDRIZZETTI, G. 2011 Intraventricular vortex flow changes in the infarcted left ventricle: numerical results in an idealised 3d shape. *Comput Methods Biomech Biomed Engin* **14** (1), 95–101.

DOMENICHINI, F., PEDRIZZETTI, G. & BACCANI, B. 2005 Three-dimensional filling flow into a model left ventricle. *Journal of Fluid Mechanics* **539**, 179–198.

DOMENICHINI, F., QUERZOLI, G., CENEDESE, A. & PEDRIZZETTI, G. 2007 Combined experimental and numerical analysis of the flow structure into the left ventricle. *J Biomech* **40** (9), 1988–94.

DONAL, E., DE PLACE, C., KERVIO, G., BAUER, F., GERVAIS, R., LECLERCQ, C., MABO, P. & DAUBERT, J. C. 2009 Mitral regurgitation in dilated cardiomyopathy: value of both regional left ventricular contractility and dyssynchrony. *Eur J Echocardiogr* **10** (1), 133–8.

DONATI, F., FIGUEROA, C. A., SMITH, N. P., LAMATA, P. & NORDSLETTEN, D. A. 2015 Non-invasive pressure difference estimation from pc-mri using the work-energy equation. *Medical Image Analysis* **26** (1), 159–172.

EBBERS, T., WIGSTROM, L., BOLGER, A. F., WRANNE, B. & KARLSSON, M. 2002 Noninvasive measurement of time-varying three-dimensional relative pressure fields within the human heart. *Journal of Biomechanical Engineering* **124** (3), 288–293.

ENGISCH, W. & MUZZIO, F. 2016 Using residence time distributions (rtds) to address the traceability of raw materials in continuous pharmaceutical manufacturing. *J Pharm Innov* **11**, 64–81.

ERIKSSON, J., CARLHÄLL, C. J., DYVERFELDT, P., ENGVALL, J., BOLGER, A. F. & EBBERS, T. 2010 Semi-automatic quantification of 4d left ventricular blood flow. *Journal of Cardiovascular Magnetic Resonance* **12** (1), 9.

FENSTER, B. E., BROWNING, J., SCHROEDER, J. D., SCHAFER, M., PODGORSKI, C. A., SMYSER, J., SILVEIRA, L. J., BUCKNER, J. K. & HERTZBERG, J. R. 2015 Vorticity is a marker of right ventricular diastolic dysfunction. *American Journal of Physiology-Heart and Circulatory Physiology* **309** (6), H1087–H1093.

FERZIGER, J. H. & PERIĆ, M. 1999 *Computational Methods for Fluid Dynamics*, 2nd edn. Berlin: Springer.

FOGLER, H. S. 1999 *Elements of chemical reaction engineering*. Third edition. Upper Saddle River, N.J. : Prentice Hall PTR, [1999] ©1999.

FRANÇOIS, C. J., SRINIVASAN, S., SCHIEBLER, M. L., REEDER, S. B., NIESPODZANY, E., LANDGRAF, B. R., WIEBEN, O. & FRYDRYCHOWICZ, A. 2012 4d cardiovascular magnetic resonance velocity mapping of alterations of right heart flow patterns and main pulmonary artery hemodynamics in tetralogy of fallot. *Journal of Cardiovascular Magnetic Resonance* **14** (1), 16.

Geiger, J., Markl, M., Jung, B., Grohmann, J., Stiller, B., Langer, M. & Arnold, R. 2011 4d-mr flow analysis in patients after repair for tetralogy of fallot. *European Radiology* **21** (8), 1651–1657.

Gharib, M., Rambod, E., Kheradvar, A., Sahn, D. J. & Dabiri, J. O. 2006 Optimal vortex formation as an index of cardiac health. *Proc Natl Acad Sci U S A* **103** (16), 6305–8.

de González, A. B. & Darby, S. 2004 Risk of cancer from diagnostic x-rays: estimates for the uk and 14 other countries. *The Lancet* **363** (9406), 345 – 351.

Harloff, A., Nussbaumer, A., Bauer, S., Stalder, A. F., Frydrychowicz, A., Weiller, C., Hennig, J. & Markl, M. 2010 In vivo assessment of wall shear stress in the atherosclerotic aorta using flow-sensitive 4d mri. *Magnetic Resonance in Medicine* **63** (6), 1529–1536.

Hirt, C., Amsden, A. & Cook, J. 1974 An arbitrary lagrangian-eulerian computing method for all flow speeds. *Journal of Computational Physics* **14** (3), 227 – 253.

Hunter, P. J., Pullan, A. J. & Smaill, B. H. 2003 Modeling total heart function. *Annu Rev Biomed Eng* **5**, 147–77.

Iles, L., Pfluger, H., Phrommintikul, A., Cherayath, J., Aksit, P., Gupta, S. N., Kaye, D. M. & Taylor, A. J. 2008 Evaluation of diffuse myocardial fibrosis in heart failure with cardiac magnetic resonance contrast-enhanced t1 mapping. *J Am Coll Cardiol* **52** (19), 1574–80.

Issa, R. 1986 Solution of the implicitly discretised fluid flow equations by operator-splitting. *Journal of Computational Physics* **62** (1), 40 – 65.

Itatani, K., Miyaji, K., Tomoyasu, T., Nakahata, Y., Ohara, K., Takamoto, S. & Ishii, M. 2009 Optimal conduit size of the extracardiac fontan operation based on energy loss and flow stagnation. *Ann Thorac Surg* **88** (2), 565–72; discussion 572–3.

KALAM, K., OTAHAL, P. & MARWICK, T. H. 2014 Prognostic implications of global lv dysfunction: a systematic review and meta-analysis of global longitudinal strain and ejection fraction. *Heart* **100** (21), 1673–80.

KARLSEN, S., DAHLSLETT, T., GRENNE, B., SJØLI, B., SMISETH, O., EDVARD-SEN, T. & BRUNVAND, H. 2019 Global longitudinal strain is a more reproducible measure of left ventricular function than ejection fraction regardless of echocardiographic training. *Cardiovascular Ultrasound* **17** (1), 18.

KELLMAN, P. & HANSEN, M. S. 2014 T1-mapping in the heart: accuracy and precision. *J Cardiovasc Magn Reson* **16**, 2.

KHALAFVAND, S. S., NG, E. Y.-K., ZHONG, L. & HUNG, T.-K. 2017 Three-dimensional diastolic blood flow in the left ventricle. *Journal of Biomechanics* **50**, 71 – 76, biofluid mechanics of multitude pathways: From cellular to organ.

KHALAFVAND, S. S., VOORNEVELD, J. D., MURALIDHARAN, A., GIJSEN, F. J. H., BOSCH, J. G., VAN WALSUM, T., HAAK, A., DE JONG, N. & KEN-JERES, S. 2018 Assessment of human left ventricle flow using statistical shape modelling and computational fluid dynamics. *J Biomech* **74**, 116–125.

KILNER, P. J., YANG, G. Z., WILKES, A. J., MOHIADDIN, R. H., FIRMIN, D. N. & YACOUB, M. H. 2000 Asymmetric redirection of flow through the heart. *Nature* **404** (6779), 759–61.

KIM, W. Y., WALKER, P. G., PEDERSEN, E. M., POULSEN, J. K., OYRE, S., HOULIND, K. & YOGANATHAN, A. P. 1995 Left ventricular blood flow patterns in normal subjects: a quantitative analysis by three-dimensional magnetic resonance velocity mapping. *J Am Coll Cardiol* **26** (1), 224–38.

KLABUNDE, R. E. 2007 *Cardiovascular Physiology Concepts*. First edition. Lippincott Williams Wilkins, [2007] ©2007.

KLABUNDE, R. E. 2012 *Cardiovascular Physiology Concepts*. Second edition. Lippincott Williams Wilkins, [2012] ©2012.

KOSKIAHO, J. 2003 Flow velocity retardation and sediment retention in two constructed wetlandâponds. *Ecological Engineering* **19** (5), 325 – 337.

KOYAMA, S., KITAMURA, T., ITATANI, K., YAMAMOTO, T., MIYAZAKI, S., OKA, N., NAKASHIMA, K., HORAI, T., ONO, M. & MIYAJI, K. 2016 Impact of top end anastomosis design on patency and flow stability in coronary artery bypass grafting. *Heart Vessels* **31** (5), 643–8.

KRITTIAN, S., JANOSKE, U., OERTEL, H. & BOHLKE, T. 2010 Partitioned fluid-solid coupling for cardiovascular blood flow: left-ventricular fluid mechanics. *Ann Biomed Eng* **38** (4), 1426–41.

LONG, Q., MERRIFIELD, R., XU, X. Y., KILNER, P., FIRMIN, D. N. & G-Z, Y. 2008 Subject-specific computational simulation of left ventricular flow based on magnetic resonance imaging. *Proc Inst Mech Eng H* **222** (4), 475–85.

LONG, Q., MERRIFIELD, R., YANG, G. Z., KILNER, P. J., FIRMIN, D. N. & XU, X. Y. 2003 The influence of inflow boundary conditions on intra left ventricle flow predictions. *J Biomech Eng* **125** (6), 922–7.

MCQUEEN, D. & PESKIN, C. 1997 Shared-memory parallel vector implementation of the immersed boundary method for the computation of blood flow in the beating mammalian heart. *The Journal of Supercomputing* **11** (3), 213–236.

MCQUEEN, D. M. & PESKIN, C. S. 1985 Computer-assisted design of butterfly bileaflet valves for the mitral position. *Scand J Thorac Cardiovasc Surg* **19** (2), 139–48.

MCQUEEN, D. M. & PESKIN, C. S. 1989 A three-dimensional computational method for blood flow in the heart. ii. contractile fibers. *Journal of Computational Physics* **82** (2), 289 – 297.

MCQUEEN, D. M. & PESKIN, C. S. 2000 A three-dimensional computer model of the human heart for studying cardiac fluid dynamics. *SIGGRAPH Comput. Graph.* **34** (1), 56–60.

McQueen, D. M. & Peskin, C. S. 2002 Heart simulation by an immersed boundary method with formal second-order accuracy and reduced numerical viscosity. In *Mechanics for a New Mellennium* (ed. H. Aref & J. W. Phillips), pp. 429–444. Dordrecht: Springer Netherlands.

Morris, D. A., Ma, X. X., Belyavskiy, E., Aravind Kumar, R., Kropf, M., Kraft, R., Frydas, A., Osmanoglou, E., Marquez, E., Donal, E., Edelmann, F., Tschope, C., Pieske, B. & Pieske-Kraigher, E. 2017 Left ventricular longitudinal systolic function analysed by 2d speckle-tracking echocardiography in heart failure with preserved ejection fraction: a meta-analysis. *Open Heart* **4** (2), e000630.

Nakamura, M., Wada, S. & Yamaguchi, T. 2006 Influence of the opening mode of the mitral valve orifice on intraventricular hemodynamics. *Ann Biomed Eng* **34** (6), 927–35.

Nguyen, V. T., Wibowo, S. N., Leow, Y. A., Nguyen, H. H., Liang, Z. & Leo, H. L. 2015 A patient-specific computational fluid dynamic model for hemodynamic analysis of left ventricle diastolic dysfunctions. *Cardiovasc Eng Technol* **6** (4), 412–29.

O'Dell, W. G. 2019 Accuracy of left ventricular cavity volume and ejection fraction for conventional estimation methods and 3d surface fitting. *Journal of the American Heart Association* **8** (6), e009124.

Park, J. J., Park, J. B., Park, J. H. & Cho, G. Y. 2018 Global longitudinal strain to predict mortality in patients with acute heart failure. *J Am Coll Cardiol* **71** (18), 1947–1957.

Pedrizzetti, G. & Domenichini, F. 2005 Nature optimizes the swirling flow in the human left ventricle. *Phys Rev Lett* **95** (10), 108101.

Peskin, C. S. 1972 Flow patterns around heart valves: A numerical method. *Journal of Computational Physics* **10** (2), 252 – 271.

QIAN, Y., LIU, J. L., ITATANI, K., MIYAJI, K. & UMEZU, M. 2010 Computational hemodynamic analysis in congenital heart disease: simulation of the norwood procedure. *Ann Biomed Eng* **38** (7), 2302–13.

SABER, N. R., GOSMAN, A. D., WOOD, N. B., KILNER, P. J., CHARRIER, C. L. & FIRMIN, D. N. 2001 Computational flow modeling of the left ventricle based on in vivo mri data: Initial experience. *Annals of Biomedical Engineering* **29** (4), 275–283.

SABER, N. R., WOOD, N. B., GOSMAN, A. D., MERRIFIELD, R. D., YANG, G. Z., CHARRIER, C. L., GATEHOUSE, P. D. & FIRMIN, D. N. 2003 Progress towards patient-specific computational flow modeling of the left heart via combination of magnetic resonance imaging with computational fluid dynamics. *Ann Biomed Eng* **31** (1), 42–52.

SCHENCK, J. F. 2000 Safety of strong, static magnetic fields. *J Magn Reson Imaging* **12** (1), 2–19.

SCHENKEL, T., MALVE, M., REIK, M., MARKL, M., JUNG, B. & OERTEL, H. 2009 Mri-based cfd analysis of flow in a human left ventricle: methodology and application to a healthy heart. *Ann Biomed Eng* **37** (3), 503–15.

SHETTIGAR, U. R., DROPMANN, M., CHRISTIAN, P. E. & KOLFF, W. J. 1989 Residence time distributions in artificial ventricles. *ASAIO Trans* **35** (3), 708–12.

SIEMENS 2015 *System Owner Manual*. Siemens Healthcare GmbH.

STALDER, A. F., RUSSE, M. F., FRYDRYCHOWICZ, A., BOCK, J., HENNIG, J. & MARKL, M. 2008 Quantitative 2d and 3d phase contrast mri: Optimized analysis of blood flow and vessel wall parameters. *Magnetic Resonance in Medicine* **60** (5), 1218–1231.

STANTON, T., LEANO, R. & MARWICK, T. H. 2009 Prediction of all-cause mortality from global longitudinal speckle strain: comparison with ejection fraction and wall motion scoring. *Circ Cardiovasc Imaging* **2** (5), 356–64.

STERN, D. A., KHANBILVARDI, R., ALAIR, J. C. & RICHARDSON, W. 2001 Description of flow through a natural wetland using dye tracer tests. *Ecological Engineering* **18** (2), 173 – 184.

SU, B., ZHANG, J., TANG, H. C., WAN, M., LIM, C. C. W., SU, Y., ZHAO, X., TAN, R. S. & ZHONG, L. 2014 Patient-specific blood flows and vortex formations in patients with hypertrophic cardiomyopathy using computational fluid dynamics. In *2014 IEEE Conference on Biomedical Engineering and Sciences (IECBES)*, pp. 276–280.

SUGHIMOTO, K., SHIMAMURA, Y., TEZUKA, C., TSUBOTA, K., LIU, H., OKU-MURA, K., MASUDA, Y. & HANEISHI, H. 2016 Effects of arterial blood flow on walls of the abdominal aorta: distributions of wall shear stress and oscillatory shear index determined by phase-contrast magnetic resonance imaging. *Heart Vessels* **31** (7), 1168–75.

SUGHIMOTO, K., TAKAHARA, Y., MOGI, K., YAMAZAKI, K., TSUBOTA, K., LIANG, F. & LIU, H. 2014 Blood flow dynamic improvement with aneurysm repair detected by a patient-specific model of multiple aortic aneurysms. *Heart Vessels* **29** (3), 404–12.

TA, C. & BRIGNAL, W. 1998 Application of computational fluid dynamics technique to storage reservoir studies. *Water Science and Technology* **37** (2), 219 – 226, reservoir Management and Water Supply â An Integrated System.

TAYLOR, C. A. & DRANEY, M. T. 2004 Experimental and computational methods in cardiovascular fluid mechanics. *Annual Review of Fluid Mechanics* **36** (1), 197–231.

TRICHON, B. H., FELKER, G., SHAW, L. K., CABELL, C. H. & O'CONNOR, C. M. 2003 Relation of frequency and severity of mitral regurgitation to survival among patients with left ventricular systolic dysfunction and heart failure. *The American Journal of Cardiology* **91** (5), 538 – 543.

Valverde, I., Nordmeyer, S., Uribe, S., Greil, G., Berger, F., Kuehne, T. & Beerbaum, P. 2012 Systemic-to-pulmonary collateral flow in patients with palliated univentricular heart physiology: measurement using cardiovascular magnetic resonance 4d velocity acquisition. *Journal of Cardiovascular Magnetic Resonance* **14** (1), 25.

Vierendeels, J. A., Riemslagh, K., Dick, E. & Verdonck, P. R. 2000 Computer simulation of intraventricular flow and pressure gradients during diastole. *Journal of Biomechanical Engineering* **122** (6), 667–674.

Watanabe, H., Sugiura, S., Kafuku, H. & Hisada, T. 2004 Multiphysics simulation of left ventricular filling dynamics using fluid-structure interaction finite element method. *Biophys J* **87** (3), 2074–85.

Wei, F. & Zhu, J.-X. 1996 Effect of flow direction on axial solid dispersion in gasâsolids cocurrent upflow and downflow systems. *The Chemical Engineering Journal and the Biochemical Engineering Journal* **64** (3), 345 – 352.

Weiss, A., Ibanez, J. A. R., Agarwal, C., Smoller, R., Contreras, J., Narula, J., Fuster, V., Badimon, J., Salvo, A. S., Santos-Gallego, C. & Sinai, M. 2017 T1 mapping in patients with heart failure with preserved ejection fraction detects increased interstitial myocardial fibrosis and assesses the severity of heart failure. *Journal of the American College of Cardiology* **69** (11 Supplement), 1478.

WHO 2017 *World Health Statistics 2017: Monitoring health for the SDGs*. World Health Organization.